ADVANCEMENTS IN STIMULATED RAMAN SCATTERING MICROSCOPY

Benjamin Figueroa, Jr

A dissertation submitted in partial fulfillment of the requirements for the degree of

Doctor of Philosophy

University of Washington
2020

Reading Committee:
Dan Fu, Chair
Robert E. Synovec
Cody W. Schlenker

Program Authorized to Offer Degree:
Chemistry

University of Washington

Abstract

ADVANCEMENTS IN STIMULATED RAMAN SCATTERING MICROSCOPY

Benjamin Figueroa, Jr

Chair of the Supervisory Committee:
Professor Dan Fu
Chemistry

Stimulated Raman scattering (SRS) microscopy has transformed our ability to image chemical and biological systems because of its sub-micrometer resolution and molecular specificity. However, limitations in small spectral coverage, poor spectral resolution, and low sensitivity hamper the ability of SRS to investigate complex systems. Furthermore, the usage of SRS microscopy beyond biological systems is still very limited.

Here I present my work which specifically addresses these issues. In chapters 2 and 3 I demonstrate the benefits of using SRS microscopy outside of its current biological niche, by investigating materials such as latent fingerprints and pharmaceutical tablets. In chapter 4 I address the limitations of poor spectral resolution and small spectral coverage by developing a parabolic fiber amplifier to provide a better SRS microscope. In chapter 5 I demonstrate an application of the developed fiber amplifier system for monitoring and quantifying temperature at the microscale level. Lastly, in chapter 6 I introduce the development of a new optical parametric oscillator (OPO) source to address the final limitation by increasing the sensitivity of SRS imaging, which ties into the future outlook on advancements needed in SRS microscopy.

Table of Contents

List of Figures

List of Tables

Acknowledgments

My efforts and determination alone would have been insufficient to complete the work presented in this dissertation. This compilation of my five-year Ph.D. journey is truly a testament to the people who have pushed me to realize my dreams and goals. I would like to take a moment to express my gratitude to those who molded me into the person I am today; I cannot begin to express how grateful I am to all of you.

First and foremost, this would not have been possible without the support of my mentor Dan Fu who is an extremely intelligent and determined scholar. Researching in your lab has given me the skills and confidence to know that I can certainly achieve anything I set my mind to. I am indebted to you for the opportunities you have given me to develop into the scientist that I am today. I could not have done it without your trust, your guidance, and your determination to see me excel.

I would have not known what it was to be a scientist if it weren't for my high school physics teacher, Tom Allen. During class, he would address us as scientists and treat us as such in helping us understand different ways to approach a problem. It's amazing to realize how much a teacher can influence a student by treating them with respect and placing confidence in them to be the next generation of researchers. His influence on my life has been substantial and has molded me to be exactly what he addressed me as 10+ years ago: a scientist.

To begin the path in becoming a research scientist, I credit the many wonderful undergraduate physics, chemistry, and biology professors who granted me the opportunities to research under their guidance. Dr. Horace Crogman, Dr. Elvis Geneston, Dr. Shareen Sabet, and Dr. Christopher Perry, I owe you each more thanks than one can give. From each of you, I was imparted with not only the skills that would help me on my journey but also with the sense that science can also benefit from having culturally diverse researchers answering new questions.

I'd also like to extend my gratitude to the current and former members of our research group: The Fu Tang Clan. I thank Yikai for always being willing to drop everything he was doing to help a laser "newbie" set up nonlinear optical experiments. Andrew, Tai, Andy, Kseniya, Bryce, Elena, and Fiona, you guys created the best lab environment I could have hoped for and I am going to miss you all. I especially thank Andrew and Tai for providing me with friendship and fond memories through the ups and downs of graduate school. I am also very grateful for Andy's willingness to entertain my far-reaching thought experiments and schemes. These past five years would not have been as great as a journey without all of you.

Spending a large portion of my 5 years researching in the lab inevitably constrained my time to enjoy companionship with those outside my research group, but I am glad I was able to forge key friendships with Sam, Meagan, and Victor. Each one of you is a blessing in my life and your friendships have helped me become a better scientist and better friend. Our Fifa adventures, board game nights, parties, lunch dates, and conversations are among my most enjoyable and memorable.

Of course, I would never be where I am today if it were not for my family. Growing up in a disadvantaged socioeconomic community, I was aware of the educational barriers facing my ethnicity. My parents, however, did not want me or my brother to accept this future for ourselves; they worked tirelessly to provide a better future. This included 1-hour+ commutes to private schools, working multiple jobs, busy schedules that resulted in late-night homework sessions, and much more. Without this unrelenting support, encouragement, and love from my parents, my path would've been much different. To my brother Eddie, I am thankful for having you as a brother. You have always given me the right words to be a better person. All I have ever wanted to do is make you and my parents proud. I love you guys.

Finally, last but definitely not the least, to the person who singlehandedly made sure I kept pressing on, my better half, Natalie. There was never a day where I felt truly alone; when the research was not going as expected, you were always there. Always finding ways to cheer me up. And when I achieved my goals, you were the first one to celebrate with me. Through the highest highs and the lowest lows, I could always count on you to walk by my side. I love you my Colombian coffee bean.

To God, who has blessed me with this life and the people in it, to Natalie, my parents, and my brother, this work is dedicated to you.

Chapter 1: Prologue

1.1 INTRODUCTION

Seeing is believing. This is easier said than done; especially when the spatial and spectroscopic traits of the object of interest limit what we can perceive with our eyes. How then, do we study that which we cannot see? With the advent of the microscope in 1609 by Galileo, we have been able to step out of the world controlled by things unseen and into a world where the agents that cause disease are made visible. Not too long after this, Newton in 1666 showed that the white light from the sun could be dispersed into a continuous series of colors. His analysis of light was the beginning of the science of spectroscopy, allowing us to study the interaction between matter and radiated energy. Combining these two scientific advancements have greatly impacted our understanding of life: from the atomic scale up to the macroscale, from a single cell to the cosmos. This thesis is about improving a spectroscopy technique, stimulated Raman scattering, to enrich our understanding of biological processes at the microscopic level.

1.2 BACKGROUND

The cell theory, states that all organisms are composed of similar units of organization, called cells. The cells are then further organized by subcellular organelles, such as the nucleus, mitochondria, and the endoplasmic reticulum, that provide a specific function in the lifespan of these building blocks. Although much is known about cells, they are still quite complex and mysterious. Understanding them has been one of our greatest scientific quests; to understand the human body and disease to prevent pain and suffering.

While the microscope had proven invaluable by allowing us to peer into the microscopic world, the common optical microscope alone could not obtain important biochemical information of cells

and their complex processes. It was not until the early 1900s, where the first use of fluorescent molecules in biological investigations were performed to stain tissues, bacteria, and other pathogens.[1,2] Through the labeling of molecules of interest using fluorescent proteins and organic dyes, we can obtain the spatial and temporal dynamics of complex biological processes. Recently in 2008, the discovery of green fluorescent proteins further facilitated the imaging of protein dynamics in living cells and animals. For many years, fluorescence microscopies have dominated the field of cellular imaging, largely because of their high spatial resolution and the wide array of available fluorescent dyes and fluorescent proteins. Fluorescence microscopies, however, are not without shortcomings. Most biomolecules of interest are not intrinsically fluorescent, therefore necessitating the development of new fluorescent tags. This heavy reliance on fluorescent labels has its limitations, including altering the physiology of the samples they are labeling, difficulty in labeling small molecules, non-uniform staining, and photobleaching.[3,4]

To obtain chemical information, we now turn our attention to spectroscopy. Vibrational spectroscopy can bypass the need for exogenous labeling as it is a direct measurement of the molecular properties. When radiation is incident upon a sample, this light will interact with the sample in some fashion. It may be reflected, absorbed, or scattered in some manner. Typically, each molecule has its own vibrational signature or spectrum, which can be used to identify it and differentiate it from other molecules. By extending this capability to a microscope, vibrational microscopy opens numerous opportunities for applications in biological research.

From the many different spectroscopy techniques, Raman spectroscopy is specifically suited for biological analysis as it is an inherently label-free, nondestructive, noninvasive vibrational technique that provides information on the chemical content of a sample.[5,6] Raman spectroscopy is a phenomenon discovered in 1928 in which photons incident on a sample are inelastically

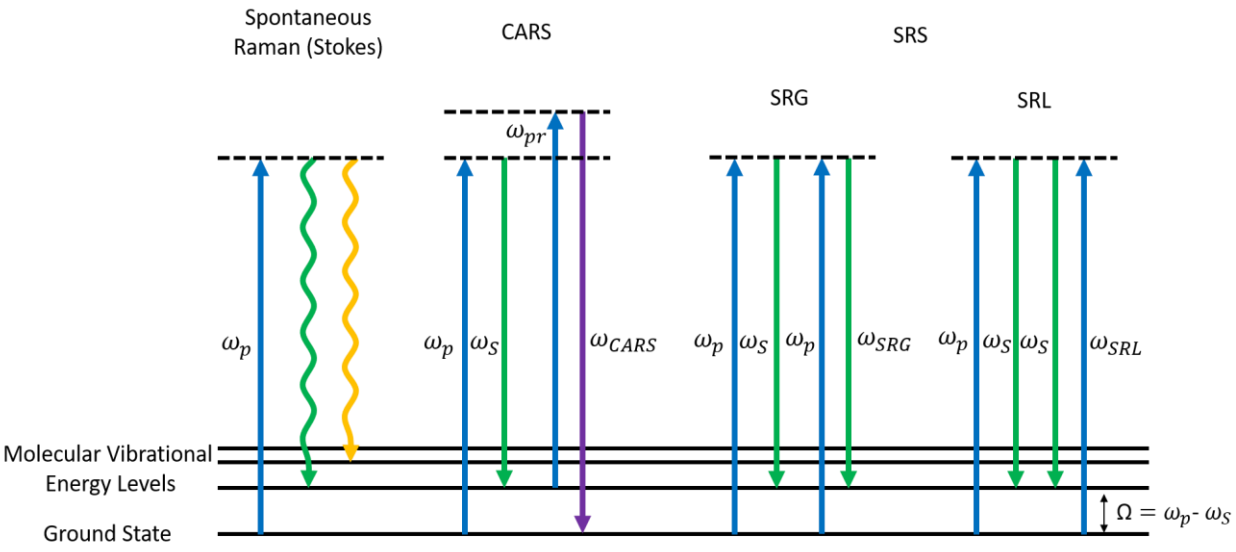

Figure 1.1 Energy diagram of spontaneous Raman scattering and coherent Raman scattering

scattered after interacting with vibrating molecules within the sample (Fig 1.1).[7] It is the change in wavelength of the scattered photon which provides the chemical and structural information. Unlike infrared spectroscopy, Raman spectroscopy is well suited for measurements in aqueous environments such as tissues and cells, because excitation wavelengths are below 1300 nm, where water does not present significant signals or absorption, obfuscating chemical analysis. Raman spectroscopy, however, is not without its limitations. Raman spectroscopy is a low signal technique compared to many other vibrational spectroscopies. Typical Raman cross-sections (the probability of the Raman phenomenon to occur) of molecules are on the order ~10^{-30} cm^{-2}, while fluorescence and infrared cross-sections are several orders of magnitude larger.[8] This low sensitivity results in long acquisition times and limits the chemical specificity due to the presence of background signals from Raman scattering of other molecules, especially within the complex domains of biological material. To address this limitation, coherent Raman scattering techniques

were developed, which offers orders-of-magnitude higher sensitivity and high-speed chemical-specific microscopy.

1.3 COHERENT RAMAN SCATTERING

Before we introduce the theory behind coherent Raman scattering (CRS) techniques, I would like to take a moment to delve deeper into the non-coherent Raman scattering version, typically referred to as spontaneous Raman scattering. When electromagnetic radiation (usually denoted as the pump, ω_p) is incident on a molecule, absorption of a photon excites the molecule to a virtual state and re-emission leads to Rayleigh (elastic) and Raman (inelastic) scattering (Fig 1.1). In the case of Raman scattering, if the scattered photon is at a shorter wavelength than the pump, then it is called a Stokes photon (ω_S). If the scattered photon is at a longer wavelength, it is denoted as an anti-Stokes photon (ω_{AS}). However, this process is not often studied, as the process begins in the less populated excited vibrational state. In both cases, these shifts in energies are referred to as wavenumbers. Detection of these inelastically scattered photons is obtained by spectrally separating the scattered photons with a monochromator(s) and filtering out the pump light source. One early factor limiting the implementation of Raman spectroscopy was the weak scattering signal. This requirement became much easier to realize following the invention of the laser in 1960.

With the development of the laser, it became possible to generate light at much higher irradiances than previously achievable. At these high irradiance intensities, new optical effects in materials were observed which involve multiple photon absorption/transitions. As laser pulses were formed with shorter and shorter pulse durations (pulse durations ranging from femtoseconds to picoseconds), the probability of a multiple photon transition pathway increases now that there are sufficient numbers of photons incident upon a molecule within a sufficiently short duration of time.

This is the premise of the field of nonlinear optics, which considers effects such as second (and higher) order harmonic generation, sum and difference-frequency generation, multi-photon absorption, and coherent Raman processes, among many others.

Both linear and nonlinear optical effects can be understood as resulting from the interaction of the electric field component of electromagnetic radiation with the charged particles of the material or molecule. Generally, an applied electric field moves positively charged particles in the direction of the field and negative charges in the opposite direction. Although the frequencies used for Raman spectroscopy are too high for the nuclei of the molecule to follow this oscillatory pattern, electrons are light enough to follow the rapid oscillations of the driving field, which induces an electric dipole moment: $\mu(t) = -e \cdot r(t)$ where e is the charge of the electron whose magnitude of the dipole depends on the extent of the displacement $r(t)$. The displacement, in turn, is dependent on how strong the electron is bound to the nuclei.

If we add up all the *N* electric dipoles per unit volume, we can model the macroscopic polarization as $P(t) = N \cdot \mu(t)$. In the linear regime (or weak applied electric fields, compared to the field that binds the electrons to the nuclei), the displacement is directly proportional to the electric field as $P(t) = \epsilon_0 \chi E(t)$. Here, ϵ_0 is the electric permittivity in a vacuum, χ is the susceptibility of the material and $E(t)$ is the time-dependent electromagnetic driving field. Such linear dependence is the origin of all linear optical phenomena.

For stronger electric fields, the electron is displaced farther from its equilibrium position. Consequently, the polarization response is not necessarily linear, and the macroscopic polarization may be expanded more generally as

$$P = \epsilon_0 \chi^{(1)} E^1(t) + \epsilon_0 \chi^{(2)} E^2(t) + \epsilon_0 \chi^{(3)} E^3 + \cdots = P^{(1)}(t) + P^{(2)}(t) + P^{(3)}(t) + \cdots$$

where the superscript denotes the order of the nonlinear effect. For simplicity, I have assumed all fields are linearly polarized and have thus reduced the vector components of the macroscopic polarization to its scalar form. The CRS processes can all be understood as resulting from the third-order contribution to the polarization $P^{(3)}$ with their magnitude mediated by $\chi^{(3)}$. The three electric field terms associated with $\chi^{(3)}$ originate from two incident laser beams, labeled as the pump and Stokes, such that the total third-order polarization is $P^{(3)} = \chi^{(3)} E_p E_S E_p$.

CRS microscopy is a growing family of the Raman scattering-based imaging techniques, with coherent anti-Stokes Raman scattering (CARS)[9–11] and stimulated Raman scattering (SRS)[12–14] modalities being the two most widely used. In both CARS and SRS, two synchronized ultrashort laser pulses (E_p and E_S) are used to coherently excite a Raman vibration that has an energy corresponding to the energy difference between the pump and Stokes ($\Omega = \omega_p - \omega_S$). This coherent excitation improves signal intensity by several orders of magnitude and eliminates interference from background fluorescence.[15] CARS was applied to microscopy first by Duncan *et al.* in 1982,[16] and later popularized in 1999 when Xie *et al.* employed a high numerical aperture (NA) objective which allowed for collinear excitation and improved phase matching conditions.[10] For nonlinear optical processes, a phase matching condition is needed for efficient signal generation. SRS soon followed suit in 2008 and has become an indispensable tool in biomedical microscopy. Since then, technical advances have pushed the boundary of CRS microscopy, which have offered new opportunities for researchers in biology, pharmacy, chemistry, and other fields. Although CARS was the first CRS technique to be used for vibrational imaging, CARS microscopy does suffer from certain limitations. The signal of CARS microscopy has a quadratic dependence on molecular concentration. Furthermore, the CARS signal includes a well-known resonant background problem which originates from a four-wave mixing process that distorts

vibrational spectra and causes image artifacts.[11,17] Developments in CARS microscopy have mitigated the non-resonant background problem by optimizing experiment procedures and post-image data processing.[18–20] The emerging SRS microscopy overcomes these limitations as the SRS signal has a strictly linear relationship with molecular concentration and is inherently free from the non-resonant background that plagues CARS. Therefore, while CARS and SRS microscopy provide the same vibrational information, SRS microscopy has been shown to provide better image quality, higher sensitivity, and superior quantification capability than CARS microscopy.

Unlike CARS, the pump and Stokes lasers interact with the sample to produce SRS signals at the frequency of pump and Stokes lasers. Because the SRS process does not generate any photon at frequencies different from ω_p and ω_S, the phase-matching condition is automatically satisfied. By energy conservation, each vibrational excitation event is accompanied by one photon loss in the pump beam, this attenuation of power is called stimulated Raman loss (SRL), and one photon gain in the Stokes beam is called stimulated Raman gain (SRG). Because the SRS signal overlaps with the excitation fields in both spectral and time domain, it is commonly extracted through high-frequency modulation and lock-in detection for high sensitivity. Detection at high-frequency (megahertz) modulation removes the noise from the slow laser intensity fluctuation and achieves near shot-noise-limited sensitivity. By raster scanning the laser focus across a sample, 3D SRS images can be constructed to provide microscopic analysis.

1.4 CHALLENGES IN SRS MICROSCOPY

In the past decade, SRS microscopy has become the favored technique of many experimentalists by allowing for the study of a wide variety of previously undetectable molecules. Owing to its high speed, chemical specificity, and diffraction-limited spatial resolution, applications have been demonstrated in lipid quantification,[21] intraoperative diagnoses,[22] drug uptake and distribution,[23]

and solid-state analysis.[24] Several multi-color SRS techniques are also developed to expand the spectroscopic capability of SRS.[25–27] Despite these successful cases, there are still unmet challenges in SRS microscopy. In this dissertation, I present to you the technical difficulties that I addressed to improve the ability of SRS to enrich our understanding of complex biological processes. The specific questions I address are: Can we increase the spectral resolution of femtosecond SRS microscopy, and if so, what technologies would be involved? Can we expand the amount of spectral information we can obtain if limited by laser bandwidth source? Can we improve the sensitivity, so that we can detect target molecules that were previously hindered by background signals usually present in the cellular environment? Furthermore, what could this tool offer to the research fields outside of biomedical imaging?

While SRS imaging is very useful in identifying chemical bonds, the ability to differentiate between similar molecules proves difficult. Many chemicals share similar bonds, so it is hard to use SRS alone to confirm chemical identification, especially when SRS only targets one or a few Raman peaks. Prior knowledge or control experiments are needed to confirm chemical identification. Isotopologues offer a convenient route to shift the vibrational transition of interest to new locations so that the chemicals can be more specifically imaged.[28] But this requires labeling and may not be easy for *in vivo* imaging and may be subject to some of the same limitations as fluorescence labeling. Despite these difficulties, there are still many cases where one Raman peak combined with prior chemical and morphological information is enough to identify certain chemicals using narrowband, picosecond light sources. But as more studies focus on the so-called "fingerprint region" –region rich with sharp Raman vibrational modes that provide particularly valuable information for molecular identification – increasing chemical specificity is a must.

An alternative approach to SRS excitation with narrowband, picosecond lasers is SRS imaging with femtosecond lasers and the "spectral-focusing" approach. The spectral focusing approach offers much higher spectral resolution than direct femtosecond laser excitation by sending the pulses through a dispersive medium. This introduces linear chirp through the temporal spreading of the frequency components of the two femtosecond excitation sources, leading to narrower instantaneous bandwidths. Tuning different vibrational frequencies within the range of the broad laser bandwidth is done by simply varying the temporal delay between the two chirped pulses. However, the current SRS spectral range of spectral focusing approaches is limited by the total bandwidth of the excitation laser sources to ~300 cm^{-1} and a low resolution of ~25 cm^{-1} (typical Raman line widths are < 10 cm^{-1}).[13,14] While these capabilities are often sufficient for imaging in the high wavenumber region (2800-3050 cm^{-1}), they are insufficient for imaging in the fingerprint region (700-1800 cm^{-1}). Therefore, increasing both the SRS spectral resolution and spectral coverage will allow for better identification and quantification of species with overlapping Raman spectra, especially in the fingerprint region.

In terms of chemical sensitivity, Raman scattering varies between molecular compounds. For common chemicals, the sensitivity is usually in the tens of millimolar levels. For molecules like β-carotene, the sensitivity can be much higher and reach hundreds of nanomolar level. Recent advances in electronic pre-resonance SRS (epr-SRS) imaging have shown to increase sensitivity up to the 250 nM range for select dyes.[29] However, such molecules also tend to suffer more from photodamage. Current sensitivity is enough for lipid imaging and protein imaging in the C-H region, where the signal is strong due to the abundance of C-H bonds, but most molecules in a cell do not reach this high concentration level. To boost sensitivity, the excitation intensity and acquisition times can be increased but photothermal damage considerations must be considered.

1.5 DISSERTATION OUTLINE

This dissertation is organized as follows: chapters 2 and 3 contain demonstrations of research fields that can benefit from the label-free, high-speed, and non-destructive nature of SRS microscopy. Specifically, in chapter 2 I demonstrate the first usage of SRS microscopy to visualize the morphology of latent fingerprints deposited on various substrates (glass slides, stainless steel, and tape). I demonstrate that detecting trace amounts of potentially illegal substances can also be achieved with SRS microscopy. As intense research is focused on making miniaturized and field-deployable SRS setups, this will soon benefit forensic analysts as they will now have a non-destructive and non-invasive tool to visualize and investigate fingerprints deposited at crimes scenes. In chapter 3, I move from the field of forensics and into the pharmaceutical sciences by demonstrating the first usage of SRS microscopy in combination with chemometric techniques to quantify the amount of unfavorable chemical reaction byproducts embedded in a compressed tablet. Formulation scientists are hard at work at optimizing the efficacy and bioavailability of many of their trade-marked drugs, which are used by millions of people worldwide. Therefore, understanding the chemical and physical properties of their active pharmaceutical ingredients (API) is a top priority, albeit one with technical challenges involved. I show that SRS microscopy can detect down to 1% API in a multicomponent drug tablet and monitor the water-mediated chemical reaction that leads to its non-active form. Both of these demonstrations were published in the Journal of Analytical Chemistry.

Chapters 4 seeks to address the issues of spectral resolution and spectral range of common SRS systems. The works in chapters 2 and 3 were feasible due to the rather simplicity of the systems being studied, but what happens when the complexity of the system increases due to overlapping spectra of similar molecules? Or when spectral information is lost due to the narrow spectral

bandwidth of the excitation laser sources? Chapter 4 describes the development of a fiber amplifier laser source which increased the spectral resolution and spectral bandwidth of our SRS microscope by 2x and 3x, respectively. This add-on module can be implemented on any SRS microscope with a 1.4-1.7 μm laser source, which will enable parabolic amplification via an Yb—doped optical fiber that allows for nonlinear interaction. Chapter 5 takes advantage of our broadband capability and embarks on a novel use of SRS microscopy by monitoring and quantifying microscale temperatures. With an increased focus on high-speed biological processes at the molecular, chemical, and biophysical levels, there has come a critical need to develop tools that combine direct spatial temperature measurements alongside multiphoton modes of contrast. However, most contact type thermometers are too large to be coupled with microscale imaging techniques. Non-contact thermosensors such as fluorescence molecules have greatly aided our ability to measure microscale temperatures but still run into the same aforementioned issues that plague all fluorescence techniques. Therefore, I demonstrate the first application of SRS microscopy to directly measure the temperature of aqueous solutions by monitoring temperature-dependent O-H Raman bands in water. A neat demonstration of imaging a stationary infrared laser beam while quantifying its radial heat profile is presented along with the quantification of thermal conductivities of subcellular organelles. This work was published in the Journal of Physical Chemistry Letters. Chapter 6 leans into future improvements needed in SRS and I start by demonstrating unpublished work on the development of an optical parametric oscillator (OPO) to increase the sensitivity of our SRS microscope. The output range of the OPO is ~680 – 900 nm, which allows us to increase Raman scattering efficiency by ω^4, increasing detection limits for molecules with small Raman scattering cross-sections or of low abundance in complex systems such as the cellular environments.

1.6 REFERENCES

(1) Mavrakis, M.; Pourquié, O.; Lecuit, T. Lighting up Developmental Mechanisms: How Fluorescence Imaging Heralded a New Era. *Development* **2010**, *137* (3), 373–387. https://doi.org/10.1242/dev.031690.

(2) Lichtman, J. W.; Conchello, J.-A. Fluorescence Microscopy. *Nature Methods* **2005**, *2* (12), 910–919. https://doi.org/10.1038/nmeth817.

(3) Schnell, U.; Dijk, F.; Sjollema, K. A.; Giepmans, B. N. G. Immunolabeling Artifacts and the Need for Live-Cell Imaging. *Nat. Methods* **2012**, *9* (2), 152–158. https://doi.org/10.1038/nmeth.1855.

(4) North, A. J. Seeing Is Believing? A Beginners' Guide to Practical Pitfalls in Image Acquisition. *The Journal of Cell Biology* **2006**, *172* (1), 9–18. https://doi.org/10.1083/jcb.200507103.

(5) Chan, J. W.; Taylor, D. S.; Zwerdling, T.; Lane, S. M.; Ihara, K.; Huser, T. Micro-Raman Spectroscopy Detects Individual Neoplastic and Normal Hematopoietic Cells. *Biophys. J.* **2006**, *90* (2), 648–656. https://doi.org/10.1529/biophysj.105.066761.

(6) Baena, J. R.; Lendl, B. Raman Spectroscopy in Chemical Bioanalysis. *Curr. Opin. Chem. Biol.* **2004**, *8* (5), 534–539. https://doi.org/10.1016/j.cbpa.2004.08.014.

(7) Raman, C. V.; Krishnan, K. S. A New Type of Secondary Radiation. *Nature* **1928**, *121* (3048), 501–502. https://doi.org/10.1038/121501c0.

(8) Nie, S.; Emory, S. R. Probing Single Molecules and Single Nanoparticles by Surface-Enhanced Raman Scattering. *Science* **1997**, *275* (5303), 1102–1106. https://doi.org/10.1126/science.275.5303.1102.

(9) Evans, C. L.; Xie, X. S. Coherent Anti-Stokes Raman Scattering Microscopy: Chemical Imaging for Biology and Medicine. *Annu. Rev. Anal. Chem.* **2008**, *1* (1), 883–909. https://doi.org/10.1146/annurev.anchem.1.031207.112754.

(10) Zumbusch, A.; Holtom, G. R.; Xie, X. S. Three-Dimensional Vibrational Imaging by Coherent Anti-Stokes Raman Scattering. *Phys. Rev. Lett.* **1999**, *82* (20), 4142–4145. https://doi.org/10.1103/PhysRevLett.82.4142.

(11) Cheng, J.-X.; Xie, X. S. Coherent Anti-Stokes Raman Scattering Microscopy: Instrumentation, Theory, and Applications. *J. Phys. Chem. B* **2004**, *108* (3), 827–840. https://doi.org/10.1021/jp035693v.

(12) Cheng, J.-X.; Xie, X. S. Vibrational Spectroscopic Imaging of Living Systems: An Emerging Platform for Biology and Medicine. *Science* **2015**, *350* (6264), aaa8870. https://doi.org/10.1126/science.aaa8870.

(13) Freudiger, C. W.; Min, W.; Saar, B. G.; Lu, S.; Holtom, G. R.; He, C.; Tsai, J. C.; Kang, J. X.; Xie, X. S. Label-Free Biomedical Imaging with High Sensitivity by Stimulated Raman Scattering Microscopy. *Science* **2008**, *322* (5909), 1857–1861. https://doi.org/10.1126/science.1165758.

(14) Hill, A. H.; Fu, D. Cellular Imaging Using Stimulated Raman Scattering Microscopy. *Analytical Chemistry* **2019**. https://doi.org/10.1021/acs.analchem.9b02095.

(15) Cheng, J.-X.; Xie, X. S. *Coherent Raman Scattering Microscopy*; CRC Press: Boca Raton, 2017.

(16) Duncan, M. D.; Reintjes, J.; Manuccia, T. J. Scanning Coherent Anti-Stokes Raman Microscope. *Opt. Lett., OL* **1982**, *7* (8), 350–352. https://doi.org/10.1364/OL.7.000350.

(17) Camp, C. H.; Lee, Y. J.; Cicerone, M. T. Quantitative, Comparable Coherent Anti-Stokes Raman Scattering (CARS) Spectroscopy: Correcting Errors in Phase Retrieval. *J. Raman Spectrosc.* **2016**, *47* (4), 408–415. https://doi.org/10.1002/jrs.4824.

(18) Day, J. P. R.; Domke, K. F.; Rago, G.; Kano, H.; Hamaguchi, H.; Vartiainen, E. M.; Bonn, M. Quantitative Coherent Anti-Stokes Raman Scattering (CARS) Microscopy. *J. Phys. Chem. B* **2011**, *115* (24), 7713–7725. https://doi.org/10.1021/jp200606e.

(19) Cicerone, M. T.; Aamer, K. A.; Lee, Y. J.; Vartiainen, E. Maximum Entropy and Time-Domain Kramers–Kronig Phase Retrieval Approaches Are Functionally Equivalent for CARS Microspectroscopy. *J. Raman Spectrosc.* **2012**, *43* (5), 637–643. https://doi.org/10.1002/jrs.3169.

(20) Vartiainen, E. M.; Rinia, H. A.; Müller, M.; Bonn, M. Direct Extraction of Raman Line-Shapes from Congested CARS Spectra. *Opt. Express* **2006**, *14* (8), 3622–3630. https://doi.org/10.1364/OE.14.003622.

(21) Wang, M. C.; Min, W.; Freudiger, C. W.; Ruvkun, G.; Xie, X. S. RNAi Screening for Fat Regulatory Genes with SRS Microscopy. *Nat. Methods* **2011**, *8* (2), 135–138. https://doi.org/10.1038/nmeth.1556.

(22) Hollon, T. C.; Pandian, B.; Adapa, A. R.; Urias, E.; Save, A. V.; Khalsa, S. S. S.; Eichberg, D. G.; D'Amico, R. S.; Farooq, Z. U.; Lewis, S.; Petridis, P. D.; Marie, T.; Shah, A. H.; Garton, H. J. L.; Maher, C. O.; Heth, J. A.; McKean, E. L.; Sullivan, S. E.; Hervey-Jumper, S. L.; Patil, P. G.; Thompson, B. G.; Sagher, O.; McKhann, G. M.; Komotar, R. J.; Ivan, M. E.; Snuderl, M.; Otten, M. L.; Johnson, T. D.; Sisti, M. B.; Bruce, J. N.; Muraszko, K. M.; Trautman, J.; Freudiger, C. W.; Canoll, P.; Lee, H.; Camelo-Piragua, S.; Orringer, D. A. Near Real-Time Intraoperative Brain Tumor Diagnosis Using Stimulated Raman Histology and Deep Neural Networks. *Nature Medicine* **2020**, *26* (1), 52–58. https://doi.org/10.1038/s41591-019-0715-9.

(23) Fu, D.; Zhou, J.; Zhu, W. S.; Manley, P. W.; Wang, Y. K.; Hood, T.; Wylie, A.; Xie, X. S. Imaging the Intracellular Distribution of Tyrosine Kinase Inhibitors in Living Cells with Quantitative Hyperspectral Stimulated Raman Scattering. *Nat Chem* **2014**, *6* (7), 614–622. https://doi.org/10.1038/nchem.1961.

(24) Cheng, Q.; Wei, L.; Liu, Z.; Ni, N.; Sang, Z.; Zhu, B.; Xu, W.; Chen, M.; Miao, Y.; Chen, L.-Q.; Min, W.; Yang, Y. Operando and Three-Dimensional Visualization of Anion Depletion and Lithium Growth by Stimulated Raman Scattering Microscopy. *Nature Communications* **2018**, *9* (1), 2942. https://doi.org/10.1038/s41467-018-05289-z.

(25) Lu, F.-K.; Ji, M.; Fu, D.; Ni, X.; Freudiger, C. W.; Holtom, G.; Xie, X. S. Multicolor Stimulated Raman Scattering (SRS) Microscopy. *Mol. Phys.* **2012**, *110* (15–16), 1927–1932. https://doi.org/10.1080/00268976.2012.695028.

(26) Fu, D.; Lu, F.-K.; Zhang, X.; Freudiger, C.; Pernik, D. R.; Holtom, G.; Xie, X. S. Quantitative Chemical Imaging with Multiplex Stimulated Raman Scattering Microscopy. *J. Am. Chem. Soc.* **2012**, *134* (8), 3623–3626. https://doi.org/10.1021/ja210081h.

(27) Freudiger, C. W.; Min, W.; Holtom, G. R.; Xu, B.; Dantus, M.; Xie, X. S. Highly Specific Label-Free Molecular Imaging with Spectrally Tailored Excitation Stimulated Raman Scattering (STE-SRS) Microscopy. *Nat. Photonics* **2011**, *5* (2), 103–109. https://doi.org/10.1038/nphoton.2010.294.

(28) Wei, L.; Yu, Y.; Shen, Y.; Wang, M. C.; Min, W. Vibrational Imaging of Newly Synthesized Proteins in Live Cells by Stimulated Raman Scattering Microscopy. *PNAS* **2013**, *110* (28), 11226–11231. https://doi.org/10.1073/pnas.1303768110.

(29) Hu, F.; Zeng, C.; Long, R.; Miao, Y.; Wei, L.; Xu, Q.; Min, W. Supermultiplexed Optical Imaging and Barcoding with Engineered Polyynes. *Nature Methods* **2018**, *15* (3), 194–200. https://doi.org/10.1038/nmeth.4578.

Chapter 2: Label-Free Chemical Imaging of Latent Fingerprints with Stimulated Raman Scattering Microscopy

The work presented in this chapter has been published in the following paper:
1) Figueroa, B.; Chen, Y.; Berry, K.; Francis, A.; Fu, D. "Label-Free Chemical Imaging of Latent Fingerprint with Stimulated Raman Scattering" Analytical Chemistry ***2017****, 89, 8m 4468-4473*

2.1 INTRODUCTION

Analyzing sensitive materials such as latent fingerprints (LFPs) has always been of paramount importance to forensic scientists both for the morphological visualization of the ridge patterns left behind by an impression and for the extraction of chemical information on foreign material. The many components found in LFPs are due both to endogenous and exogenous substances. Endogenous components are composed of substances such as fatty acids, sterols, and epidermal residue which could be used to identify age,[1,2] while cosmetics, explosives, and drugs comprise the exogenous compounds than can be used to link a donor to a crime scene.[3–5] Therefore, chemical imaging of LFPs would aid in the investigation and interpretation of evidence left at crime scenes for forensic scientists and the criminal justice system.[6,7]

The basic principle of LFP development is to produce and enhance a distinct contrast between the ridge pattern and the grooves. Choosing the best detection technique or sequence of physical, chemical, and instrumental techniques for LFP detection is dependent on not only the nature of the substrate where deposition occurred but also the presence of exogenous chemicals, as well as environmental factors.[8] Changes of LFPs over time have also been explored, since these changes are useful in determining the time in which the fingerprint was deposited at the crime scene for assessing it as evidence.[9–11] A major analytical challenge in LFP analysis is to identify the chemical history of the fingerprint.[12,13] A notable example includes drug metabolite detection in LFPs based on the specificity of antigen–antibody interactions.[14] Unfortunately, the dependence of specific

interactions on trace amounts of LFP samples typically requires prior knowledge of target chemicals/biochemicals and time-consuming preparation.

Recently, mass spectrometry (MS) has emerged as a viable tool for imaging LFPs. MS imaging approaches offer great sensitivity and excellent specificity allowing the identification of unknown molecules present in LFPs. Notably, MS imaging was utilized to detect and map LFPs tainted with exogenous chemicals integral to condom lubricants.[15,16] This chemical information could provide stronger support as evidence in alleged cases of sexual assault. Both desorption electrospray ionization MS[17] and matrix-assisted laser desorption/ionization MS[18] have proven valuable as label-free detection techniques for the chemical analysis and imaging of LFPs. However, MS techniques require long sample preparation times and are often destructive to the sample.

It has been shown that vibrational spectroscopy imaging techniques such as Fourier transform infrared spectroscopy (FT-IR)[10,19,20] and Raman spectroscopy (RS)[21,22] can also provide morphological and chemical images of LFPs. Unlike MS, most vibrational imaging techniques require little to no sample preparation. In addition, its nondestructive nature allows for future reanalysis of the sample with different modalities. Although FT-IR and Raman spectroscopy are complementary vibrational detection techniques, a key difference is in their sample preparation procedures. FT-IR spectroscopy requires elaborate sample preparation compared to Raman, which is not desired in handling LFPs. Unfortunately, RS suffers from low signal efficiency, requiring extremely long acquisition times to image a sample. Surface-enhanced RS (SERS) has been shown to increase selectivity, contrast, and sensitivity, through the binding of nanoparticles to specific proteins, among other robust fingerprint constituents, to indirectly provide chemical information regarding the given proteins.[23] As with any labeling techniques, this approach necessitates prior knowledge of targets for interaction purposes. In addition, the need for signal amplification by

nanomaterials requires additional sample processing and could bring in uncertainty for subsequent chemical analysis.

Because spontaneous Raman inherently suffers from slow acquisition rates, poor resolution, and lack of sensitivity, stimulated Raman scattering (SRS) microscopy has emerged as a superior alternative for the imaging of intrinsic molecular vibrations.[24–30] SRS microscopy uses two synchronized ultrashort laser pulses (pump and Stokes) to coherently excite a Raman vibration that has an energy corresponding to the energy difference between the pump and the Stokes. The coherent excitation improves signal intensity by several orders of magnitude and eliminates interference from background fluorescence.[29] Technical advances have pushed the boundary of SRS in terms of spectral acquisition speed, detection sensitivity, spatial resolution, and penetration depth in living systems.[24,31,32] However, the use of this powerful label-free technique outside living systems has rarely been explored.

In this paper, label-free SRS was employed to rapidly and easily image the morphology of the LFP by probing the Raman lipid band. In addition to imaging the pattern of the LFP based on lipid contrasts, we further demonstrate that foreign chemicals can be identified using hyperspectral SRS imaging.[31–33] This analysis was done by utilizing the spectral focusing approach,[31] which mechanically delays one of the two beams in time to provide the scanning of the Raman excitation frequency when the pump and Stokes beams are appropriately chirped. Furthermore, we present a novel approach of chemically imaging an LFP directly off transparent adhesive tape, bypassing the need for dusting and staining to further simplify visualization and eliminate cross contamination. To our knowledge, this paper presents the first introduction of using SRS for forensic analysis.

2.2 METHODS

2.2.1 Chemicals and Materials

Reagent grade methanol, ethanol, potassium nitrate, and benzoic acid were all purchased from Sigma-Aldrich (St. Louis, MO) with purity ≥95%. Blackhorn 209 Muzzleloading Powder (black powder) was purchased from a local Cabela's store. The substrates used for LFP deposition included 1.0 mm thick glass slides, stainless steel, and transparent adhesive tape. Glass coverslips are from Thermo Scientific (Portsmouth NH). All substrates were washed with a combination of water, ethanol, and methanol before use.

2.2.2 Preparation of Fingerprints

All fingerprints were voluntarily provided by a Hispanic male. The donor would simply press his thumb on the desired substrates for about 3 s which were then mounted onto the microscope for imaging. For the LFPs imaged every 24 h, samples were kept at room temperature with low humidity (<30%). For the LFPs imaged 96 h apart, samples were kept in an incubator at 37 °C. To prepare the LFP containing exogenous compounds (black powder and benzoic acid powders), the donor would press on the powder for about 3 s and then proceed to deposit it on the glass slide substrate. Excess loose powder was brushed from the fingertip with another finger before deposition. A similar preparation technique was again carried out for the tape-lifting experiment. The sebum-rich fingerprint was primed by touching one's nose and then deposited on a glass slide. Transparent adhesive tape was then used to lift the fingerprint off the original slide and was subsequently attached to a new slide for imaging.

2.2.3 Hyperspectral SRS Imaging

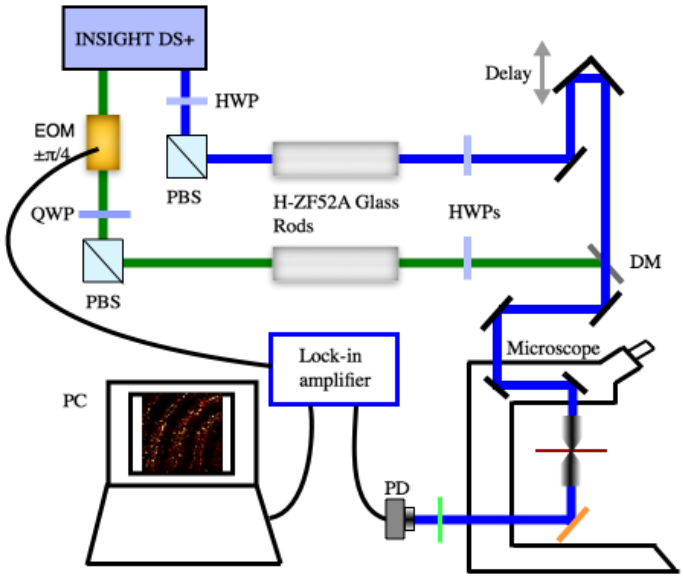

Figure 2.1 Schematic diagram of the SRS spectroscopy setup based on a broadband femtosecond dual beam laser system. EOM, electro-optical beamsplitter; HWP, half waveplate; DM, dichroic mirror.

A broadband femtosecond dual beam laser system (Insight DS+ from Spectra-Physics) is used for SRS imaging. Figure 2.1 shows our experimental setup. The Insight DS+ provides dual output beams at an 80 MHz repetition rate; a tunable beam (pump) ranges from 680 to 1300 nm, and a fixed beam (Stokes) is at 1040 nm. The Stokes beam is modulated by an electro-optical modulator (EOM) at 10 MHz. A motorized delay line is inserted into the pump beam to scan the time delay between the two pulse trains. The Stokes and pump beams are chirped by long high dispersion H-ZF52A glass rods with a total travel length of 48 and 60 cm, respectively. Pulse widths after chirping of the Stokes and pump beams are 1.59 and 2.89 ps, respectively, as measured by a home-built autocorrelator. These changes provide a spectral resolution of ~25 cm^{-1}. After recombining the two beams through the dichroic mirror DMSP1000 (Thorlabs), the laser is sent into a home-built laser scanning microscope (NIKON Eclipse FN1). Nikon microscope objectives of 16× (N16XLWD-PF) and 40× (CFI Apo Lambda S 40XWI) with 0.8 and 1.25 NA, respectively, were

used to focus the beams onto the samples. On the detection side, the Stokes beam is filtered out by a short-pass filter FESH1000 (Thorlabs), and the pump beam is detected by a 10 × 10 mm^2 silicon photodiode (Hamamatsu) biased at 56 V and then amplified by a home-built transimpedance amplifier. Stimulated Raman loss (SRL) signal is detected with a Zurich Instruments lock-in amplifier (H2FLI). Each frame is 512 × 512 pixels and takes 2 s to scan. To obtain a multiframe spectrum, the total acquisition time varied from 30 to 40 s, depending on the spectral range desired. When multiple frames were acquired to build a montage, these scans were stitched together using the Grid/Collection Stitching plugin in ImageJ.

2.3 RESULTS AND DISCUSSION

The human fingerprint residue is a complex mixture of numerous compounds originating from different sources and processes such as epidermal renewal and secretions by secretory glands in the dermis. The vast abundance of lipids and proteins present on the finger can be attributed to the secretory glands and is the main reason why extensive research has focused on these two components to explore LFPs.[10,19,21,22] Lipids and proteins have broad overlapping Raman peaks around 2850 and 2930 cm^{-1}, respectively.[27] Here we focused on the extensively studied Raman band corresponding to lipids to provide our contrasts for LFP imaging. A spontaneous Raman spectrum of LFP deposited on silicon is provided in the Supporting Information in Figure A.1. As a comparison, the spontaneous Raman spectrum of oleic acid is shown to confirm that the Raman signal of LFP that we are targeting originates from sebum lipids. This conclusion agrees with previous literature.[34]

To demonstrate the capability of SRS imaging of endogenous fatty acids in the LFPs on a glass slide substrate, our pump beam was tuned to 800 nm to excite near the CH_2 bonds for lipids (2850 cm^{-1}), while our Stokes beam was fixed at 1040 nm. At the focus, the Stokes and pump beam have an average power of 40 mW each. For SRS spectral peak calibration, dimethyl sulfoxide (DMSO) was acquired at 800 nm and shown in Figure A.2. Figure2.2A shows the general ridge pattern of a LFP which is composed of stitched 20 × 20 SRS frames. Total imaging acquisition time is 8 min. The ridge patterns of the LFPs are clearly visible, as there is no signal from lipids in valley regions. Note that the sebum molecules seem to follow a "railroad" feature along the ridges, with lower signal appearing in between these ledges. This is likely due to the fact that as the ridges are pressed upon the substrate, a majority of the sebum molecules are pushed out from the ridges, giving rise to this particular feature. Nonetheless, this demonstration of SRS for morphologically visualizing

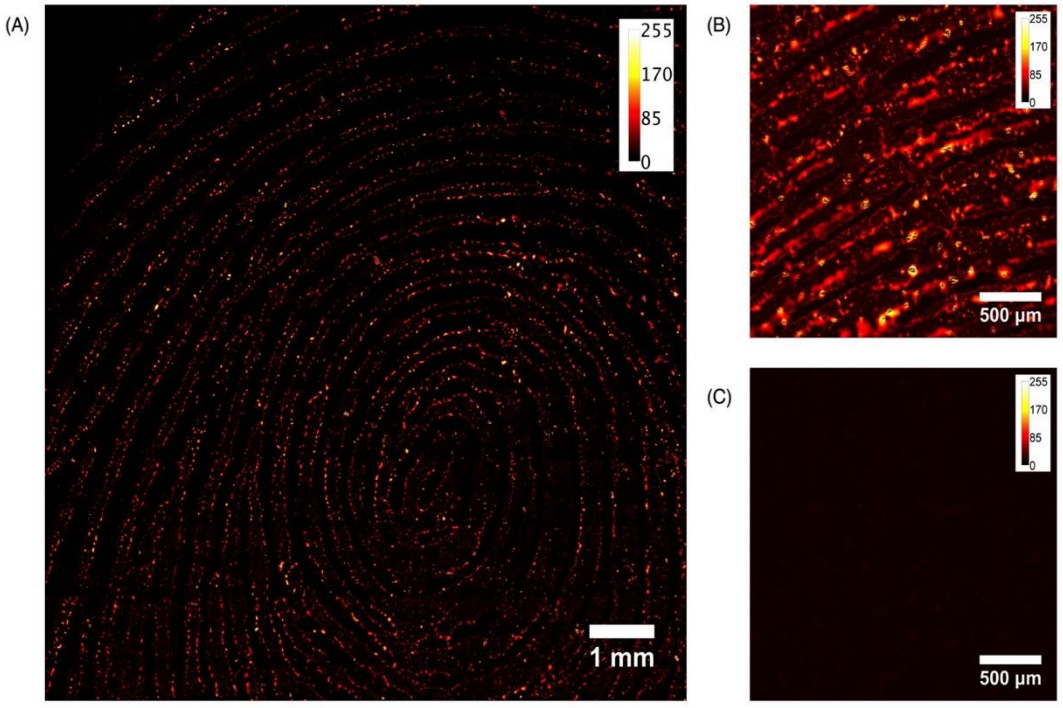

Figure 2.2 Label-free SRS images of LFPs based on lipid contrasted deposited on glass slides. (A) 10 x 10 mm^2 image of an LFP at 2850 cm^{-1}, (B) on-resonance image of a LFP at 2850 cm^{-1}, and (C) off-resonance of the same area around 2800 cm^{-1}.

the LFP based on lipid Raman signal is useful for the identification of an individual based on the patterns of their ridges. For our subsequent experiments, our SRS images were on a smaller scale for proof-of-concept demonstrations. To further validate that the contrasts in our SRS image arise from lipid Raman signal, an on-resonant image (Figure 2.2B) at 2850 cm^{-1} and off-resonant image (Figure 2.2C) at 2800 cm^{-1} were collected. The absence of off-resonant signal confirms that the SRS signal has negligible contribution from other non-Raman optical effects.

To demonstrate the nondestructive imaging capability that SRS microscopy enables, a sequence of images is shown in Figure 2.3 to display the ability of acquiring signal from the sebum molecules every 24 h for 96 h. These images are composed of stitched 5 × 5 SRS frames of a LFP. The ridge patterns of the LFPs are again clearly visible, as there is no signal from lipids in valley regions. Importantly, there is no obvious change of fingerprint pattern during the 96 h of imaging, showing the capacity of SRS to successfully detect LFPs without destroying samples for future analysis. Our imaging result is contrary to the finding of Muramoto and Sisco.[9] It was suggested that lipids migrate over time and gradually smear out the ridge pattern. This feature was used to date the fingerprint. However, in our study of lipids on glass, we did not notice any major lipid

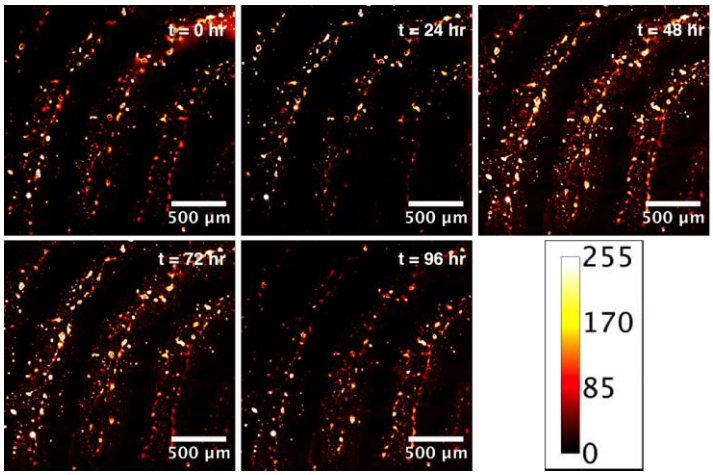

Figure 2.3 Label-Free SRS images of a LFP on a glass slide at t = 0, 24, 48, 72, 96 hr. Images are 2 x 2 mm^2

diffusion. To examine if lipid diffusion/smearing would occur at different temperatures, an SRS image of an LFP was imaged and then left in an incubator for 96 h at 37 °C. Again, no apparent diffusion or smearing was observed as shown in Figure 2.4.

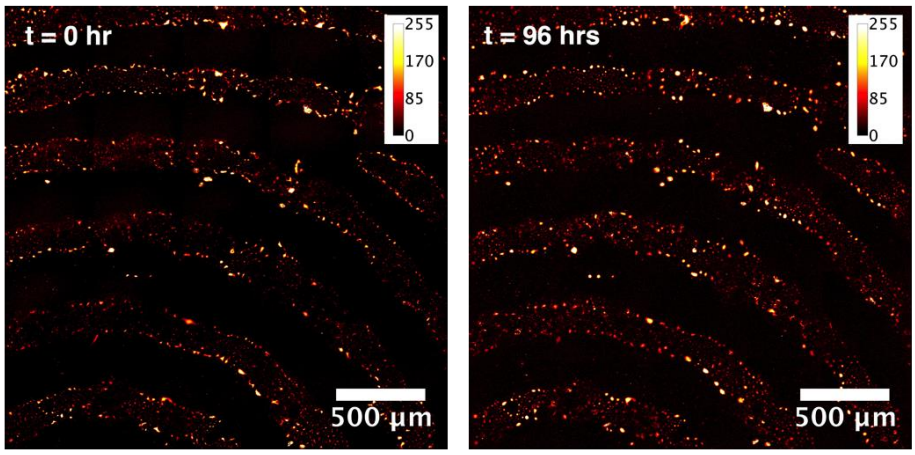

Figure 2.4 Label-Free SRS images of a LFP on a glass slide at t = 0 h and t = 96 h kept at 37°C

To determine whether we can acquire LFP on other substrates and whether lipid diffusion is dependent on substrates, we imaged LFPs deposited on stainless steel. For this particular experiment, the substrate was no longer transparent, and therefore, an epi-mode detection configuration on our Nikon microscope was employed to collect the backscattered photons onto our photodiode. Details pertinent to epi-mode detection can be found in the Supporting Information. For this substrate, we used a 40× objective with a smaller focal volume, to minimize artificial signal collected by the 16× objective due to its larger focal volume generated by the stainless steel substrate due to its large depth of focus. At the focus, the Stokes and pump beam each have an average power of 20 mW. The LFP images are constructed by stitching 7 × 10 frames. From Figure 2.5 it is apparent that SRS signal can be generated from LFPs on a metallic surface even after 120 h. No diffusion was observed. This experiment further confirms that SRS has the capability to detect and image LFPs nondestructively on different substrates over extended periods of time.

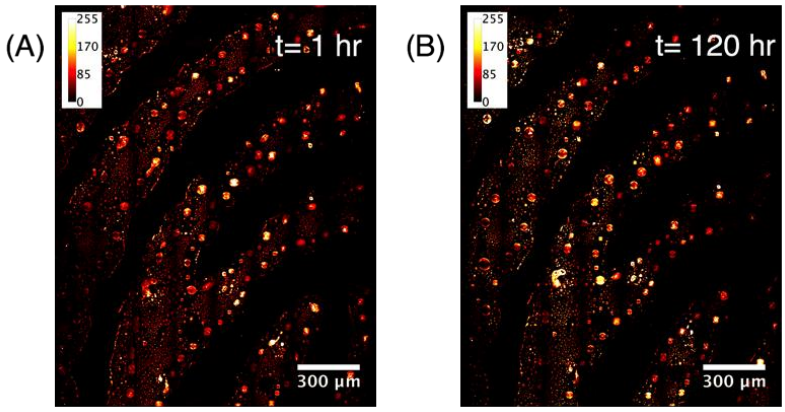

Figure 2.5 Label-Free SRS images of a LFP deposited on a stainless steel substrate at (A) t = 1 h and (B) t = 120 h. Images are 1.5 x 2 mm^2

Next, we demonstrate that chemical contrast and analysis of exogenous compounds in LFP is achievable through SRS, a capability that is important in forensic science to obtain more information relevant to individual identity. To demonstrate this capability, we dosed our LFP with trace amounts of two different exogenous compounds. For the illustration of detecting chemicals that could be used as a propellant in firearms, potassium nitrate (KNO_3) was used as a model exogenous compound to detect on our LFP. For SRS spectral peak calibration of KNO_3, a spectrum of naphthalene was acquired as shown (Figure A.3a). For the basis of our LFP image, Figure 2.6A was captured at 2850 cm^{-1} (gray, lipid), and subsequently, Figure 2.6B was captured at 1067 cm^{-1} (green, KNO_3) to detect our exogenous compound. Easy chemical contrast is achievable upon merging the two images as shown in Figure 2.6C. For correct targeting of the desired Raman signal to be ensured, a SRS spectral scan from 930 to 1210 cm^{-1} by the interpulse delay scanning of our chirped beams is shown in Figure 2.6D.

To demonstrate feasibility of potassium nitrate detection from fingerprints exposed to gunpowder, we performed a similar experiment using Blackhorn 209 Muzzleloading Powder which is a mixture of 75% potassium KNO_3, 15% carbon (charcoal), and 10% sulfur. The Raman band for KNO_3 corresponding to 1067 cm^{-1} was again probed. Similarly, Figure 2.7A was

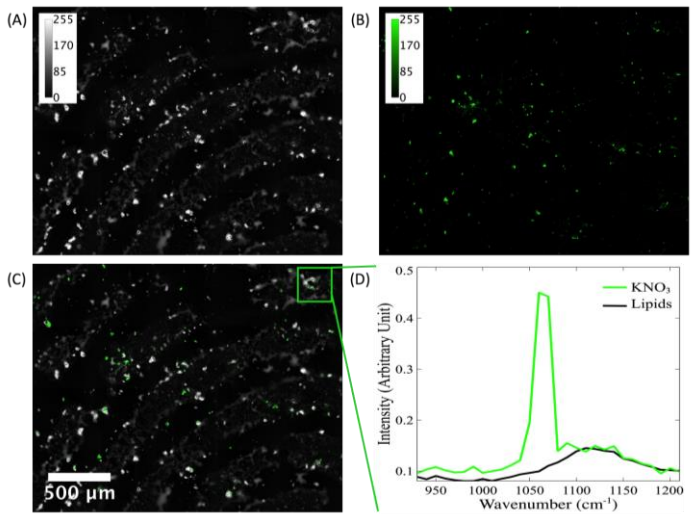

Figure 2.6 SRS images and spectra of LFPs dosed with pure KNO_3. (A) LFP acquired at 2850 cm^{-1} and (B) LFP acquired at 1067 cm^{-1}. (C) Image of merged channels from A and B. (D) SRS spectrum of pure KNO_3. The LFP images were composed of 5 x 5 SRS frames.

captured at 2850 cm^{-1} (gray, lipid), and then Figure 2.7B was captured at 1067 cm^{-1} (green, KNO_3) to detect the target within the mixture. Through the collection process it became evident that the spatially offset, yet broad absorbance peak from charcoal would produce artificial signals, which would interfere with the acquisition of KNO_3 and lipid channel signatures. Nonetheless, with the advantage of KNO_3's narrow vibrational peak, an off-resonance image was acquired to subtract the broad absorbance signal. The remaining signal is thus KNO_3 as shown in Figure 2.7B. Once the channels are merged, the black powder is easily distinguishable from the lipid channel. In contrast to other LFP samples, the "railroad" pattern is mostly absent from the image, and we hypothesize that this is due to the fine powder mixing with the sebaceous molecules in such a fashion as to render a more homogeneous morphology. A SRS spectral span from 930 to 1210 cm^{-1} is shown in Figure 2.7D to confirm that the Raman signal is from KNO_3.

In a similar fashion, for the illustration of detecting illicit drugs, we used benzoic acid powder as our stand-in compound for cocaine, as it is an acknowledged degradation product of cocaine[35] with a reported Raman peak at 1639 cm^{-1}. For SRS spectral peak calibration of benzoic

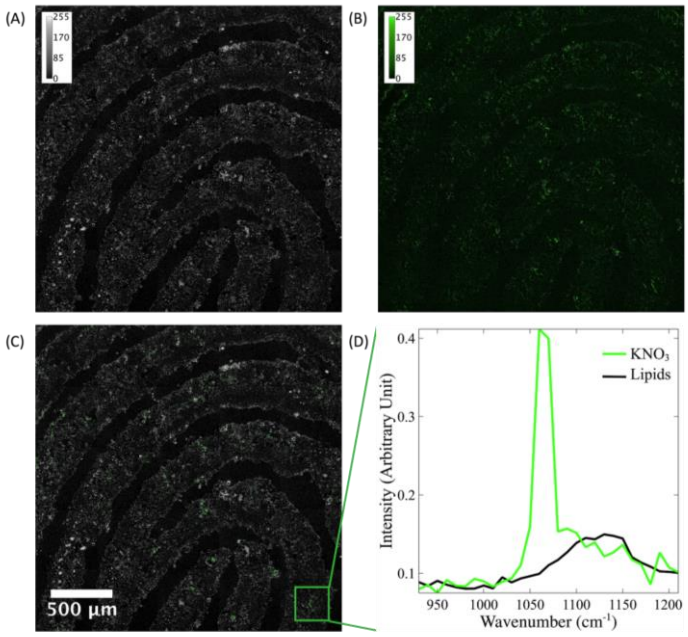

Figure 2.7 SRS images and spectra of LFPs dosed with black powder. (A) LFP acquired at 2850 cm^{-1}. (B) LFP acquired at 1067 cm^{-1}. (C) Image of merged channels from parts A and B. (D) SRS spectrum of KNO_3 within black powder on the LFP. The LFP images were composed of 5 x 5 frames.

acid, a spectrum of a 50/50 solution mixture of oleic acid and acetone (Figure A.3b) was acquired. To gather a complete LFP image, the LFP image was again collected at the two different wavenumbers: Figure 2.8A, captured at 2850 cm^{-1} (gray, lipid), and Figure 2.8B, captured at 1639 cm^{-1} (magenta, benzoic acid). Distinctive chemical contrast is again shown to be achievable upon merging (Figure 2.8C). Hyperspectral SRS imaging spanning from 1490 to 1780 cm^{-1} of the imaged area reveals the spectrum of benzoic acid within the LFP (Figure 2.8D). With this demonstration of the capability of SRS to correctly identify model examples of explosive and drug related material, other compounds pertinent to forensic analysis should also be identifiable including trinitrotoluene (TNT), RDX, pentaerythritol tetranitrate (PETN), cocaine, and amphetamines to name a few. All of these substances have been characterized by spontaneous Raman,[21,36] and therefore can be greatly exploited by SRS.

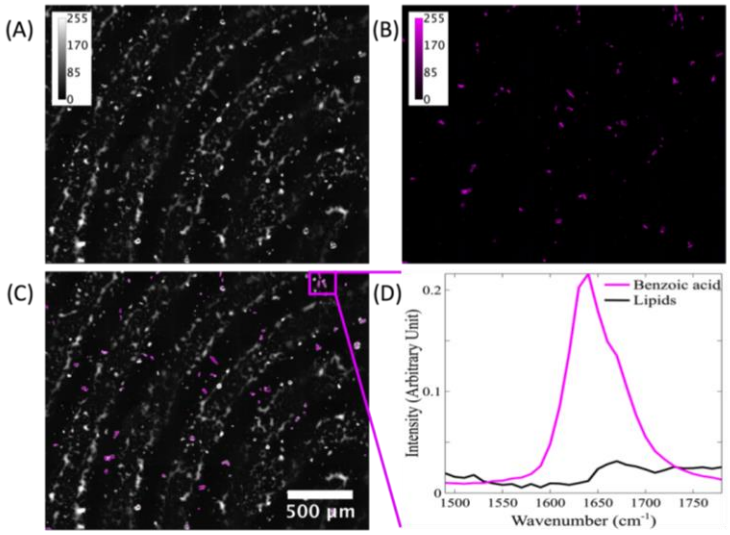

Figure 2.8 (A) SRS images and spectra of LFPs dosed with benzoic acid. (A) LFP acquired at 2850 cm^{-1} and (B) LFP acquired at 1639 cm^{-1}. (C) Imaged of merged channels from A and B. (D) SRS spectrum of benzoic acid.

Exploring exogenous compounds by SRS proves useful as a rapid and simple label-free imaging tool. The spectral acquisition time to determine the exogenous contaminant requires about 35–40 s which is a very suitable time scale for forensic researchers. The dimensions of the particles examined are typically in the range 2–40 µm. Sparsity of the particles was not an issue as the SRS imaging has high throughput with submicron resolution. Figure 2.9A shows an example of a zoomed-in SRS image of a tiny KNO_3 particle on a fingerprint. The size of the particle is determined to be 1.9 × 3.5 μm^2. A line plot across the particle (Figure 2.9B) shows that the signal-to-noise for detecting this small particle is 34. We note that although SRS detection has limited sensitivity in biological applications due to the low concentration of biomolecules, in forensic applications, it is less of an issue because most chemical residuals are present at very high concentrations with sparse localization. This characteristic facilitates chemical identification with SRS imaging.

Lastly, previous reports have demonstrated Raman mapping and chemical information extraction from LFPs lifted by adhesive tapes,[23] but a few challenges were found: (1) Adhesive

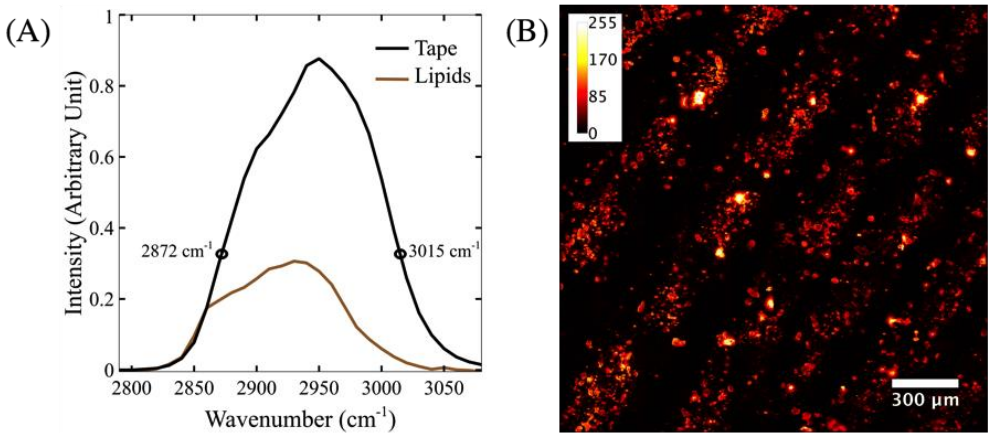

Figure 2.9 (A) SRS spectra of lipids and adhesive tape from 2790 cm^{-1} to 3080 cm^{-1}. (B) SRS image after subtraction of tape signal by two different wavenumbers (2872 cm-1 and 3015 cm^{-1}) SRS images are 2 x 2 mm^2

material has strong spectral features that often overwhelm weak spectral signals of the individual components embedded within the LFP, and (2) the slow speed of Raman imaging is not practical for revealing spatial images of the fingerprint. Although the first challenge can be overcome with multivariate analysis, the long acquisition time required to survey the fingerprint to identify region of interests presents a major problem in chemical analysis, especially for trace amounts of chemicals. We solved this problem by quickly surveying the fingerprint with rapid SRS imaging. To remove the spectral contribution from tape, we performed SRS imaging at two different wavenumbers. The tape has equal SRS signals at these wavenumbers and can be subtracted out, while the sebum signal remains. We chose 2872 and 3015 cm^{-1} as suitable wavenumbers for the eventual subtraction to reveal the lipid SRS signal masked underneath as shown in Figure 2.10A. The two images at different wavenumbers before subtraction are provided in the Supporting Information as Figure A.4. We chose to image with the 40× objective to limit the focal volume during acquisition. The result of our subtraction procedure is shown in Figure 2.10B, which is composed of stitched 10 × 10 SRS frames of a LFP. From Figure 2.10B, it is evident that there is a slight morphological change pertaining to the lipid ridges; there are no longer “railroad” ledges,

and the lipid globules seem to occupy more of the space in between these lipid regions. The reason we currently observe this morphological change is currently unclear to us. We hypothesize that this change could be due to the hydrophobicity of the lifting material, which is different from the hydrophilic glass slide, interacting with the sebum molecules differently. Nonetheless, this technique still provides the morphological features of fingerprints for forensic analysis.

2.4 CONCLUSIONS

The SRS method described in this work fills an important function for the morphological and chemical imaging of latent fingerprints on multiple substrates with no sample destruction and preparation. We have demonstrated raid survey of fingerprint patterns with high spatial resolution. Chemical identification is achieved by hyperspectral SRS imaging. However, difficulties arise when the substrate exhibits a stronger and/or overlapping spectra over the lipid signal from the LFP, such as wood and lifting tape as demonstrated which contain CH_2 stretching bonds. It was shown in this paper, that this is resolved by subjecting the lifted material via tape to SRS and the collected SRS spectra are analyzed by the simple subtraction method. This method does not require prior dusting and staining of the LFP for visualization and analysis. Therefore, LFP substrate-dependent analysis would be no longer an issue for forensic analysts. The attractiveness of SRS imaging is that it does not require long acquisition times such as Raman Imaging. The success of this study shows that this method has great potential in the forensic field to fight crime as it provides chemical sensitivity to detect trace elements within the fingerprint and also bypass the need for any sample preparation, eliminating risks of contamination and sample degradation. Our spectral acquisition range is currently limited by the laser to 300 cm^{-1}. The range can be extended by changing laser wavelengths, but involved additional scanning time. In order to continue progress on this effort beyond the proof-of-concept, future work will focus on improving the

Raman spectral range by imaging with broadband laser sources. Although currently SRS imaging can only be performed in a laser lab, the rapid advancement of fiber laser technology could potentially provide a field-deployable device for forensic analysis.

2.5 REFERENCES

(1) Antoine, K. M.; Mortazavi, S.; Miller, A. D.; Miller, L. M. Chemical Differences Are Observed in Children's Versus Adults' Latent Fingerprints as a Function of Time*. *Journal of Forensic Sciences* **2010**, *55* (2), 513–518. https://doi.org/10.1111/j.1556-4029.2009.01262.x.

(2) Williams, D. K.; Brown, C. J.; Bruker, J. Characterization of Children's Latent Fingerprint Residues by Infrared Microspectroscopy: Forensic Implications. *Forensic Science International* **2011**, *206* (1), 161–165. https://doi.org/10.1016/j.forsciint.2010.07.033.

(3) Leggett, R.; Lee-Smith, E. E.; Jickells, S. M.; Russell, D. A. "Intelligent" Fingerprinting: Simultaneous Identification of Drug Metabolites and Individuals by Using Antibody-Functionalized Nanoparticles. *Angewandte Chemie* **2007**, *119* (22), 4178–4181. https://doi.org/10.1002/ange.200700217.

(4) Peng, T.; Qin, W.; Wang, K.; Shi, J.; Fan, C.; Li, D. Nanoplasmonic Imaging of Latent Fingerprints with Explosive RDX Residues. *Anal. Chem.* **2015**, *87* (18), 9403–9407. https://doi.org/10.1021/acs.analchem.5b02248.

(5) Kazarian, C. R., K. L. Andrew Chan, Sergei G. Combining the Tape-Lift Method and Fourier Transform Infrared Spectroscopic Imaging for Forensic Applications - Camilla Ricci, K. L. Andrew Chan, Sergei G. Kazarian, 2006. *Applied Spectroscopy* **2016**.

(6) Weyermann, C.; Ribaux, O. Situating Forensic Traces in Time. *Science & Justice* **2012**, *52* (2), 68–75. https://doi.org/10.1016/j.scijus.2011.09.003.

(7) van Asten, A. C. On the Added Value of Forensic Science and Grand Innovation Challenges for the Forensic Community. *Science & Justice* **2014**, *54* (2), 170–179. https://doi.org/10.1016/j.scijus.2013.09.003.

(8) Becue, A.; Moret, S.; Champod, C.; Margot, P. Use of Stains to Detect Fingermarks. *Biotechnic & Histochemistry* **2011**, *86* (3), 140–160. https://doi.org/10.3109/10520290903462838.

(9) Muramoto, S.; Sisco, E. Strategies for Potential Age Dating of Fingerprints through the Diffusion of Sebum Molecules on a Nonporous Surface Analyzed Using Time-of-Flight Secondary Ion Mass Spectrometry. *Anal. Chem.* **2015**, *87* (16), 8035–8038. https://doi.org/10.1021/acs.analchem.5b02018.

(10) Girod, A.; Xiao, L.; Reedy, B.; Roux, C.; Weyermann, C. Fingermark Initial Composition and Aging Using Fourier Transform Infrared Microscopy (μ-FTIR). *Forensic Science International* **2015**, *254*, 185–196. https://doi.org/10.1016/j.forsciint.2015.07.022.

(11) Dorakumbura, B. N.; Becker, T.; Lewis, S. W. Nanomechanical Mapping of Latent Fingermarks: A Preliminary Investigation into the Changes in Surface Interactions and Topography over Time. *Forensic Science International* **2016**, *267*, 16–24. https://doi.org/10.1016/j.forsciint.2016.07.024.

(12) Xu, L.; Li, Y.; Wu, S.; Liu, X.; Su, B. Imaging Latent Fingerprints by Electrochemiluminescence. *Angewandte Chemie International Edition* **2012**, *51* (32), 8068–8072. https://doi.org/10.1002/anie.201203815.

(13) Beresford, A. L.; Hillman, A. R. Electrochromic Enhancement of Latent Fingerprints on Stainless Steel Surfaces. *Anal. Chem.* **2010**, *82* (2), 483–486. https://doi.org/10.1021/ac9025434.

(14) Hazarika, P.; Jickells, S. M.; Wolff, K.; Russell, D. A. Imaging of Latent Fingerprints through the Detection of Drugs and Metabolites. *Angewandte Chemie International Edition* **2008**, *47* (52), 10167–10170. https://doi.org/10.1002/anie.200804348.

(15) Bradshaw, R.; Wolstenholme, R.; Blackledge, R. D.; Clench, M. R.; Ferguson, L. S.; Francese, S. A Novel Matrix-Assisted Laser Desorption/Ionisation Mass Spectrometry Imaging Based Methodology for the Identification of Sexual Assault Suspects. *Rapid Communications in Mass Spectrometry* **2011**, *25* (3), 415–422. https://doi.org/10.1002/rcm.4858.

(16) Musah, R. A.; Cody, R. B.; Dane, A. J.; Vuong, A. L.; Shepard, J. R. E. Direct Analysis in Real Time Mass Spectrometry for Analysis of Sexual Assault Evidence. *Rapid Communications in Mass Spectrometry* **2012**, *26* (9), 1039–1046. https://doi.org/10.1002/rcm.6198.

(17) Ifa, D. R.; Manicke, N. E.; Dill, A. L.; Cooks, R. G. Latent Fingerprint Chemical Imaging by Mass Spectrometry. *Science* **2008**, *321* (5890), 805–805. https://doi.org/10.1126/science.1157199.

(18) Wolstenholme, R.; Bradshaw, R.; Clench, M. R.; Francese, S. Study of Latent Fingermarks by Matrix-Assisted Laser Desorption/Ionisation Mass Spectrometry Imaging of Endogenous Lipids. *Rapid Communications in Mass Spectrometry* **2009**, *23* (19), 3031–3039. https://doi.org/10.1002/rcm.4218.

(19) Ricci, C.; Bleay, S.; Kazarian, S. G. Spectroscopic Imaging of Latent Fingermarks Collected with the Aid of a Gelatin Tape. *Anal. Chem.* **2007**, *79* (15), 5771–5776. https://doi.org/10.1021/ac070580j.

(20) Crane, N. J.; Bartick, E. G.; Perlman, R. S.; Huffman, S. Infrared Spectroscopic Imaging for Noninvasive Detection of Latent Fingerprints. *Journal of Forensic Sciences* **2007**, *52* (1), 48–53. https://doi.org/10.1111/j.1556-4029.2006.00330.x.

(21) Day, J. S.; Edwards, H. G. M.; Dobrowski, S. A.; Voice, A. M. The Detection of Drugs of Abuse in Fingerprints Using Raman Spectroscopy I: Latent Fingerprints. *Spectrochimica Acta Part A: Molecular and Biomolecular Spectroscopy* **2004**, *60* (3), 563–568. https://doi.org/10.1016/S1386-1425(03)00263-4.

(22) Widjaja, E. Latent Fingerprints Analysis Using Tape-Lift, Raman Microscopy, and Multivariate Data Analysis Methods. *Analyst* **2009**, *134* (4), 769–775. https://doi.org/10.1039/B808259F.

(23) Song, W.; Mao, Z.; Liu, X.; Lu, Y.; Li, Z.; Zhao, B.; Lu, L. Detection of Protein Deposition within Latent Fingerprints by Surface-Enhanced Raman Spectroscopy Imaging. *Nanoscale* **2012**, *4* (7), 2333–2338. https://doi.org/10.1039/C2NR12030E.

(24) Freudiger, C. W.; Min, W.; Saar, B. G.; Lu, S.; Holtom, G. R.; He, C.; Tsai, J. C.; Kang, J. X.; Xie, X. S. Label-Free Biomedical Imaging with High Sensitivity by Stimulated Raman Scattering Microscopy. *Science* **2008**, *322* (5909), 1857–1861. https://doi.org/10.1126/science.1165758.

(25) Cheng, J.-X.; Xie, X. S. Vibrational Spectroscopic Imaging of Living Systems: An Emerging Platform for Biology and Medicine. *Science* **2015**, *350* (6264), aaa8870. https://doi.org/10.1126/science.aaa8870.

(26) Lu, F.-K.; Basu, S.; Igras, V.; Hoang, M. P.; Ji, M.; Fu, D.; Holtom, G. R.; Neel, V. A.; Freudiger, C. W.; Fisher, D. E.; Xie, X. S. Label-Free DNA Imaging in Vivo with Stimulated Raman Scattering Microscopy. *PNAS* **2015**, *112* (37), 11624–11629. https://doi.org/10.1073/pnas.1515121112.

(27) Ji, M.; Orringer, D. A.; Freudiger, C. W.; Ramkissoon, S.; Liu, X.; Lau, D.; Golby, A. J.; Norton, I.; Hayashi, M.; Agar, N. Y. R.; Young, G. S.; Spino, C.; Santagata, S.; Camelo-Piragua, S.; Ligon, K. L.; Sagher, O.; Xie, X. S. Rapid, Label-Free Detection of Brain Tumors with Stimulated Raman Scattering Microscopy. *Science Translational Medicine* **2013**, *5* (201), 201ra119-201ra119. https://doi.org/10.1126/scitranslmed.3005954.

(28) Camp Jr, C. H.; Cicerone, M. T. Chemically Sensitive Bioimaging with Coherent Raman Scattering. *Nat Photon* **2015**, *9* (5), 295–305. https://doi.org/10.1038/nphoton.2015.60.

(29) Cheng, J.-X.; Xie, X. S. *Coherent Raman Scattering Microscopy*; CRC Press: Boca Raton, 2017.

(30) Tipping, W. J.; Lee, M.; Serrels, A.; Brunton, V. G.; Hulme, A. N. Stimulated Raman Scattering Microscopy: An Emerging Tool for Drug Discovery. *Chem. Soc. Rev.* **2016**, *45* (8), 2075–2089. https://doi.org/10.1039/C5CS00693G.

(31) Fu, D.; Holtom, G.; Freudiger, C.; Zhang, X.; Xie, X. S. Hyperspectral Imaging with Stimulated Raman Scattering by Chirped Femtosecond Lasers. *J. Phys. Chem. B* **2013**, *117* (16), 4634–4640. https://doi.org/10.1021/jp308938t.

(32) Fu, D.; Zhou, J.; Zhu, W. S.; Manley, P. W.; Wang, Y. K.; Hood, T.; Wylie, A.; Xie, X. S. Imaging the Intracellular Distribution of Tyrosine Kinase Inhibitors in Living Cells with Quantitative Hyperspectral Stimulated Raman Scattering. *Nat Chem* **2014**, *6* (7), 614–622. https://doi.org/10.1038/nchem.1961.

(33) Fu, D.; Lu, F.-K.; Zhang, X.; Freudiger, C.; Pernik, D. R.; Holtom, G.; Xie, X. S. Quantitative Chemical Imaging with Multiplex Stimulated Raman Scattering Microscopy. *J. Am. Chem. Soc.* **2012**, *134* (8), 3623–3626. https://doi.org/10.1021/ja210081h.

(34) Czamara, K.; Majzner, K.; Pacia, M. Z.; Kochan, K.; Kaczor, A.; Baranska, M. Raman Spectroscopy of Lipids: A Review. *Journal of Raman Spectroscopy* **2015**, *46* (1), 4–20. https://doi.org/10.1002/jrs.4607.

(35) Penido, C. A. F. de O.; Pacheco, M. T. T.; Lednev, I. K.; Silveira, L. Raman Spectroscopy in Forensic Analysis: Identification of Cocaine and Other Illegal Drugs of Abuse. *Journal of Raman Spectroscopy* **2016**, *47* (1), 28–38. https://doi.org/10.1002/jrs.4864.

(36) Zabetakis, G. C., Charles K. Manka, Jacob Grun, Sergei Nikitin, Daniel. Identification of Explosives with Two-Dimensional Ultraviolet Resonance Raman Spectroscopy - Gelu Comanescu, Charles K. Manka, Jacob Grun, Sergei Nikitin, Daniel Zabetakis, 2008. *Applied Spectroscopy* **2008**.

Chapter 3: Detecting and Quantifying Microscale Chemical Reactions in Pharmaceutical Tablets by Stimulated Raman Scattering Microscopy

The work presented in this chapter has been published in the following paper:
1) Figueroa, B.; Nguyen, T.; Sotthivirat, M.; Xu, X,; Rhodes, T.; Lamm, M. S.; Smith, R. L.; John, C.T.; Su, Y.; Fu, D. "Detecting and Quantifying Microscale Chemical Reactions in Pharmaceutical Tablet by Stimulated Raman Scattering Microscopy" Analytical Chemistry ***2019****, 91, 10, 6894-6901*

3.1 INTRODUCTION

Overcoming poor water solubility and low bioavailability of pharmaceutical candidates has been of great interest in drug development with the rapid growth of small molecule drugs in recent years.[1–3] Most formulation techniques aim to improve the physicochemical properties of an ionizable compound through formation of a weakly basic (or acidic) salt.[4] These formulations greatly increase the water solubility, bioavailability, and dissolution rate of the active pharmaceutical ingredients (APIs).[5,6] In addition to pharmacochemical advantages, salt formation also improves API stability during manufacturing and storage.[7,8] However, due to processing conditions or reactions with other formulation ingredients (excipients), salt forms of APIs have a propensity to revert back to the less soluble free base (or acid) form. This process is generally referred to as salt disproportionation.[4,9,10] Salt disproportionation is extremely undesirable as it results in suboptimal physicochemical stability and decreased pharmaceutical bioavailability.[11–13] Thus, it is important to determine the mechanism and kinetics of salt disproportionation in order to develop formulation strategies to prevent it.

Salt disproportionation as a chemical reaction is highly dependent on the local pH created by the excipients. Although the concept of pH does not typically apply to solids, the local pH refers to

the pH in a microscopic layer of adsorbed water at a solid surface in which the surface molecules are mobilized.[4,10,14] In the case of solid dosage forms, the local pH can be greatly influenced by excipients possessing acid/base functionalities that are in intimate contact in a multicomponent formulation. A variety of studies have been performed to investigate the roles of excipient chemistry, formulation storage, and stability to reveal influential factors in disproportionation.[13,15–18] One commonly used excipient is magnesium stearate (Mgst) which serves as a lubricant that reduces the adhesion between the powder and the processing equipment. However, Mgst is known to induce significant salt disproportionation of acidic APIs, especially at high relative humidity (RH).[5,15,19–21] Recently, the HCl salt form of pioglitazone (PIO-HCl), which is used for treating type II diabetes, has become a popular model API for proof-of-concept methods to study disproportionation.[5,15,19,21,22] PIO-HCl has a tendency to readily undergo disproportionation to its free base (PIO-FB) due to its low disproportionation pH (pH_{max}) when interacting with problematic excipients.[15,23,24] Although previous studies have suggested that disproportionation is a solution-mediated transformation, the physical and chemical interplay between PIO-HCl, Mgst, and humidity are not well understood. Thus, to assist designs of robust formulations, it is critical to develop a complete mechanistic understanding of salt disproportionation.

Significant gaps exist today in the characterization capabilities available in solids due to the diverse requirements of the information needed and the desire for high spatial resolution to resolve drug particle heterogeneity. Very few tools currently provide the ability to non-invasively monitor microscale chemical reactions in a heterogenous solid system. Although techniques such as thermal analysis, X-ray powder diffraction, and IR/Raman/NMR spectroscopy can determine the presence of phase or chemical changes, they have limited sensitivity (especially for low drug loading samples) and cannot provide chemical mapping of relevant species at high spatial

resolution or detailed insights into the microscale interactions within formulations.[25] Addressing this challenge will advance our understanding of the stability of drug formulations and the molecular mechanisms of deleterious physicochemical changes such as salt disproportionation.

Various analytical techniques have been used to study salt disproportionation of PIO-HCl.[4–6,15,16,19,21,22,26] Hirsh et al. used ^{35}Cl solid-state NMR (ssNMR) to characterize the disproportionation reaction of PIO-HCl in mixtures with metallic stearates.[22] By directly probing the Cl^- anions in both the intact salt and disproportionation products, the ssNMR spectra provided proof of the reactions between the chloride anions in the API salt and the metal cations in the stearates to produce solid salts such as NaCl or $MgCl_2$. However, the information obtained through these bulk measurements does not reveal the spatial heterogeneity that is present in complex multicomponent tablets. By utilizing high resolution synchrotron X-ray diffractometry (SXRD), Koranne et al. have investigated the spatiotemporal mapping of PIO-HCl disproportionation for the first time.[21] The findings provided an in-depth understanding of the spatial heterogeneity of the disproportionation reaction, with the initiation of the reaction occurring at the tablet surface and moving toward the core. Although it was demonstrated that water plays a role in the reaction through a fluorescence dye, the inability to monitor the chemical interplay between the API, excipients, and water limits the applicability of SXRD for monitoring the dynamic physicochemical changes of solid formulation. Label-free chemical imaging based on Raman spectroscopy can potentially address these limitations. Nie et al. demonstrated that Raman spectroscopy could be used to study the disproportionation kinetics of PIO-HCL in a multi-component tablet matrix at low quantities (5% drug loading) using a statistically optimized sampling method.[19] Using the proposed approach, Raman imaging was successfully shown to detect disproportionation within the microenvironment of the API particle in tablet matrices with

a lower detection limit than conventional Raman spectroscopy. However, challenges inherent to spontaneous Raman, such as low sensitivity, slow acquisition speed, and inadequate spatial resolution, still impede detection and quantification of components in drug tablets at common pharmaceutical dosages.

To overcome the limitations of spontaneous Raman, coherent Raman scattering microscopies, including coherent anti-Stokes Raman Scattering (CARS) and stimulated Raman scattering (SRS) have emerged as powerful alternatives for characterization of solid-state materials.[27–31] These methods are widely used to generate chemical contrasts to investigate drug distribution and dissolution.[32–40] CARS and SRS microscopy provide the same vibrational information, but SRS microscopy has been shown to provide better image quality, higher sensitivity, and superior quantification capability than CARS microscopy due to its lack of a non-resonant background.[41,42] However, high resolution imaging and quantification of changing chemicals in drug formulations due to chemical transformation have not been reported. In this manuscript, we apply hyperspectral SRS (hsSRS) imaging to investigate the disproportionation reaction of the PIO salt with submicron spatial resolution. We demonstrate that SRS microscopy, in combination with chemometric modelling, can detect and quantify salt disproportionation in a complex multicomponent tablet at low drug loadings (1% DL). We then investigate the impact of Mgst on the disproportionation reaction of PIO-HCl into its free base in a tablet matrix and elucidate the mechanism by which the reaction occurs. Furthermore, most formulations contain less than 1% of Mgst, which present an analytical challenge for previous reports.[5,19,21,22] Herein, we demonstrate that hsSRS imaging can quantitatively detect ingredients with low concentration and monitor their chemical and physical changes in multicomponent drug formulations. Moreover, we provide, to the best of our knowledge, the first direct evidence for water mediated salt disproportionation. These results

highlight the potential of hsSRS imaging as a powerful analytical platform for monitoring and quantifying microscale chemical reactions, a capability that will prove to be widely useful for studying not only pharmaceutical drugs, but also many other solid-state systems.

3.2 EXPERIMENTAL SECTION

3.2.1 Materials and Tablet Preparations

Pioglitazone HCl salt (PIO-HCl) and free base (PIO-FB) were purchased from Fischer Scientific (Waltham, MA, USA). Magnesium stearate, Avicel pH 102, Mannitol SD 200, and Crospovidone were provided by Merck & Co, Inc. (Kenilworth, NJ, USA). Deuterated stearate acid was purchased from Sigma Aldrich (Saint Louis, MO, USA) for in-house synthesis of deuterated magnesium stearic (d-MgSt).[43] Briefly, saponification between d-stearic acid and sodium hydroxide produced deuterated sodium stearate, which was used in a double decomposition reaction with magnesium sulfate to obtain d-Mgst.

A few binary and multicomponent tablets were produced as listed in Table B.1. Briefly, PIO-HCl was ground with a mortar and pestle to reduce polarization effects due to crystallinity structure before tablet production. Then, the desired amount of components were weighed, added to a bottle and blended for 10 min at 50 rpm using a Turbula mixer (Model T2F, Glen Mills, Clifton, NJ). Binary formulations were composed of MgSt and PIO-HCl. A placebo blend consisting of 31.5 g Avicel pH 102, 15 g Mannitol SD 200, and 2.5 g Crospovidone 2.5 g was utilized for multicomponent formulations. The final blends (100 mg) were weighed out and compressed into tablets on an instrumented servo-hydraulic single station tablet press (Roland Research Devices Inc., model CS-1) using a 9/32 inch flat faced round tooling using a 9/32 inch flat faced round tooling. Tablets were compressed at approximately 7 kN, stored in 5 °C or stressed under 40°C/75% RH conditions for 9 days for reaching the equilibrium of the reaction.[5]

3.2.2 Hyperspectral SRS Imaging

A broadband femtosecond dual beam laser system (Insight DS+ from Spectra-Physics) used for hsSRS imaging has been described in previous publications.[39,44] Figure B.1 shows our experimental setup. Briefly, the Insight DS+ provides dual output beams at an 80 MHz repetition rate: a tunable beam (pump) which ranges from 680 to 1300 nm, and a fixed beam (Stokes) at 1040 nm. The pump and Stokes beams are chirped by a grating-based pulse stretcher.[45,46] An Nikon microscope objective of 25 (XLPN25XWMP2) with 1.15 NA in epi-mode configuration, was used to focus the beams onto the samples. At the focus, the Stokes and pump beam have an average power of 40 mW, each. Backscattered light by the sample was collected by the excitation objective and reflected by a polarizing beamsplitter (PBS). A quarter waveplate was placed between the PBS and the objective to produce circularly polarized light. The reflected light was then focused on to the photodiode. Raster scanning of the laser focus generates SRS images with 512 x 512 pixels at 8 μs/pixel dwell time (frame rate 0.5 frame/second). Hyperspectral acquisition was done via the spectral focusing approach,[47] which mechanically delays one arm in time to provide the sequential scanning of the Raman excitation frequency when the femtosecond pump and Stokes beams are appropriately chirped. This generates a Raman spectrum for each pixel in the image. The spectral resolution of our hsSRS system is ~ 12 cm^{-1}.

3.2.3 Chemometric Analysis of Imaging Data

All chemometric models were built using the PLS Toolbox by Eigenvector and in-house Matlab scripts. To generate our calibration curve, we prepared binary mixtures of PIO-HCl and PIO-FB ranging from 100% PIO-HCl to 50% PIO-HCl (50% PIO-FB). HsSRS imaging of these binary mixtures at six different fields of view (FOV) were used to build the calibration model, which was then applied to the chemometric analysis of drug formulation samples.

3.3 RESULTS AND DISCUSSION

To validate that our SRS technique is capable of quantifying changes of chemical composition in a solid-state system, we first generated a Partial Least Squares (PLS) model to test the capability of SRS to differentiate and quantify the amount of disproportionation. PLS is a multivariate regression method used to build quantitative calibration models and has been previously employed to study hyperspectral data of pharmaceutical formulations using NIR and Raman spectroscopy.[19,48–51] By mixing different ratios of PIO-HCl to PIO-FB, it is clear that the peak at 1610 cm^{-1} increases while the peak at 1640 cm^{-1} decreases as free base amount is increased (Fig 3.1A). For model development, the mean spectra of the obtained hyperspectral data cubes of mixed drug powder were used. The PLS models were built using 2 latent variables, to avoid overfitting.[52] This number was chosen because it minimized root mean squares error of cross-validation (RMSECV) and explains 99.49% of X variance and 99.58% variance of Y for PIO-FB. Cross-validation was performed by contiguous block leave-one-out cross-validation. A low value of RMSECV indicates the balance between predictive power and fitting (Fig 3.1B).

Next, we validated our PLS model by testing mixtures that were not included in building our model (1, 19, 29, and 51% PIO-FB), resulting in a root mean squares error of prediction (RMSEP) of 1.183% which confirms the robustness of our PLS model (Fig. 3.1B). We note that residual error is likely due to incomplete mixing of powder samples and limited sampling size. The chemical mapping of the validation mixtures can then be generated by the regression vectors of the PLS model to convert the spectral information of each pixel into predicted relative concentrations, with red and blue pixels representing PIO-HCl and PIO-FB, respectively. Generated PLS predictions images of validation samples containing 1% and 51% PIO-FB are shown in Fig. 3.1C and D, respectively. The predicted compound concentration of the imaged

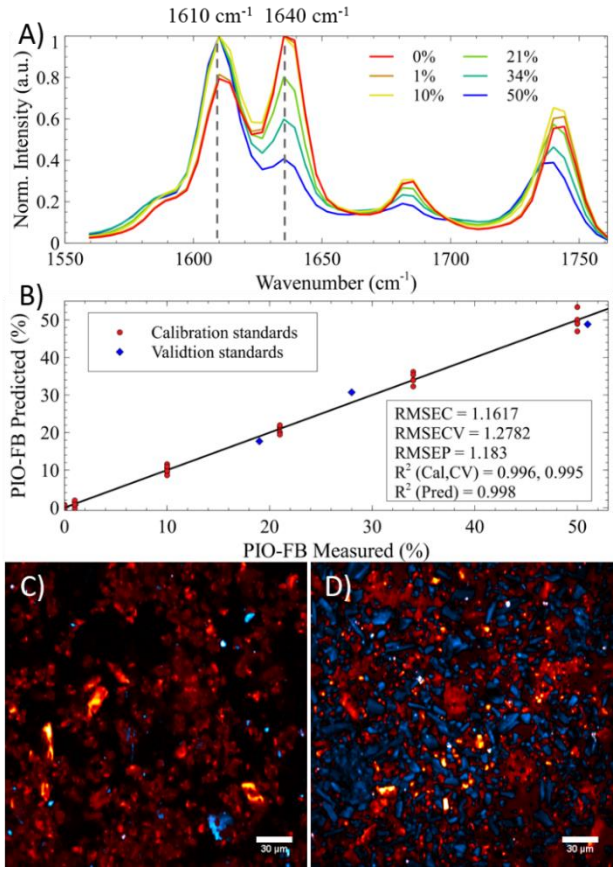

Figure 3.1 (A) Measured SRS spectra of six binary mixtures of PIO-HCl and PIO-FB mixed at different measures of PIO-FB (%w/w). (B) PLS model for the calibration mixture. Chemical image of 1% (C) and 51% (D) PIO-HCl/PIO-FB mixed samples generated from the PLS regression vectors. PIO-HCl and PIO-FB are represented in red and blue, respectively.

samples is calculated by the mean value of all predicted pixel relative concentrations. The predicted amounts were 0.72% for Fig. 1C and 48.85% for Fig. 3.1D. Therefore, SRS demonstrates to be a rapid, robust, and quantitative technique for the determination salt disproportionation.

Following the high-speed mapping of API (Fig. B.4), hsSRS imaging of selected regions of interest containing API were performed and analyzed to quantify drug disproportionation. Multicomponent tablets consisting of 1% API DL were prepared under two different storage conditions: one unstressed condition stored at 5° C and another stressed at 40° C and 75% RH

(Table A.1). Five different FOV were scanned for each condition. Based on the validated PLS model, prediction of the disproportionation amount was carried out for each condition (Table 3.1). Our results reveal higher values of PIO salt conversion ratio compared with previous measurements obtained from other techniques (~20-30%) with the consideration that the extent of the salt to free base form conversion depends on various physiochemical properties and formulation parameters.[15,19,21] Additionally, our measurement is sensitive to the surface, where the reaction is most active, while other techniques provide bulk measurements. We confirmed that the disproportionation is higher on the surface than inside by performing a cross-sectional scan of the tablet after exposing the tablet to high humidity (Fig. B.5). Nonetheless, these numbers are consistent with the consensus that the relative humidity is an important factor in the salt disproportionation process through a solution mediated reaction.[53] It is apparent that the disproportionation extent varies substantially for the stressed condition at different locations of the tablet, indicating the heterogeneity of the reaction across the surface of the tablet. Understanding the molecular mechanism behind the disproportionation reaction, could offer possible insights into the spatial heterogeneity of the disproportionation conversion across the surface of tablet sample.

Table 3.1 Quantification of relative salt disproportionation in multicomponent tablets at 1% DL

TRIAL	CONTROL (%)	STRESSED (%)
1	2.74	23.41
2	6.27	33.29
3	8.68	52.95
4	2.22	36.13
5	0.22	39.05

For PIO disproportionation to happen, a proton acceptor is required, a role that is believed to be played by Mgst. Mgst is believed to play this role for several reasons. First, Mgst (pK_a ~ 4.5) can elevate the microenvironmental pH value beyond the pH_{max} of the salt as confirmed by slurry pH

tests.[15] Second, the carboxylate group in Mgst acts as a proton acceptor to convert the salt form to its free base form and produce stearic acid and deliquescent $MgCl_2$ through the following reaction.[12,26]

$$2\,PIO - HCl + (R - COOH^-)_2Mg^{2+} \xrightarrow{75\%\,RH,\ 40°C} 2\,PIO + 2\,(R - COOH) + MgCl_2$$

Equation 3.1 Proposed disproportionation reaction of Pioglitazone-HCl with Mgst

To elucidate the mechanism of salt disproportionation, we then performed time-lapse imaging of a multicomponent control tablet (1% PIO-HCl, 1% Mgst, and 98% excipients) and stressed it at 45 °C and 60% RH for 90 hours. We imaged the same FOV at 0, 1, 2, 3, 4, and 90 hours (Fig. 3.2). The disproportionation reaction was examined in our hyperspectral data using a straightforward spectral unmixing procedure (non-negative least squares) based on *a priori* knowledge of the basis SRS spectra measured from pure compounds (Fig. B.2) to obtain chemical maps.[47,54] This is due to drift in experimental setup overtime, resulting in less accurate fitting with the PLS model. At the unstressed condition (0 hour), no apparent PIO-FB is detected within the matrix of PIO-HCl, which agrees well with our previous imaging results (Table 3.1). As the sample is stressed from the zero time-point up to 90 hours we can then start to visualize how PIO-FB resides spatially adjacent to the PIO-HCl salt from which it came. This disproportion process begins quickly within a few hours and continues over time. At the 90th hour, some API fragments have almost completely reverted to the free base form with only a small detectable presence of the PIO-HCl usually residing at the center of the particle. It is interesting to note that the amount of Mgst (magenta colored pixels) is equivalent to that of the API but is largely unobserved in this field of view; a testament to the heterogeneity of the drug formulation. Moreover, the disproportionation reaction occurs without Mgst spatially located near the API fragment(s), which suggests that physical contact between Mgst and PIO-HCl is not required for disproportionation to occur. However,

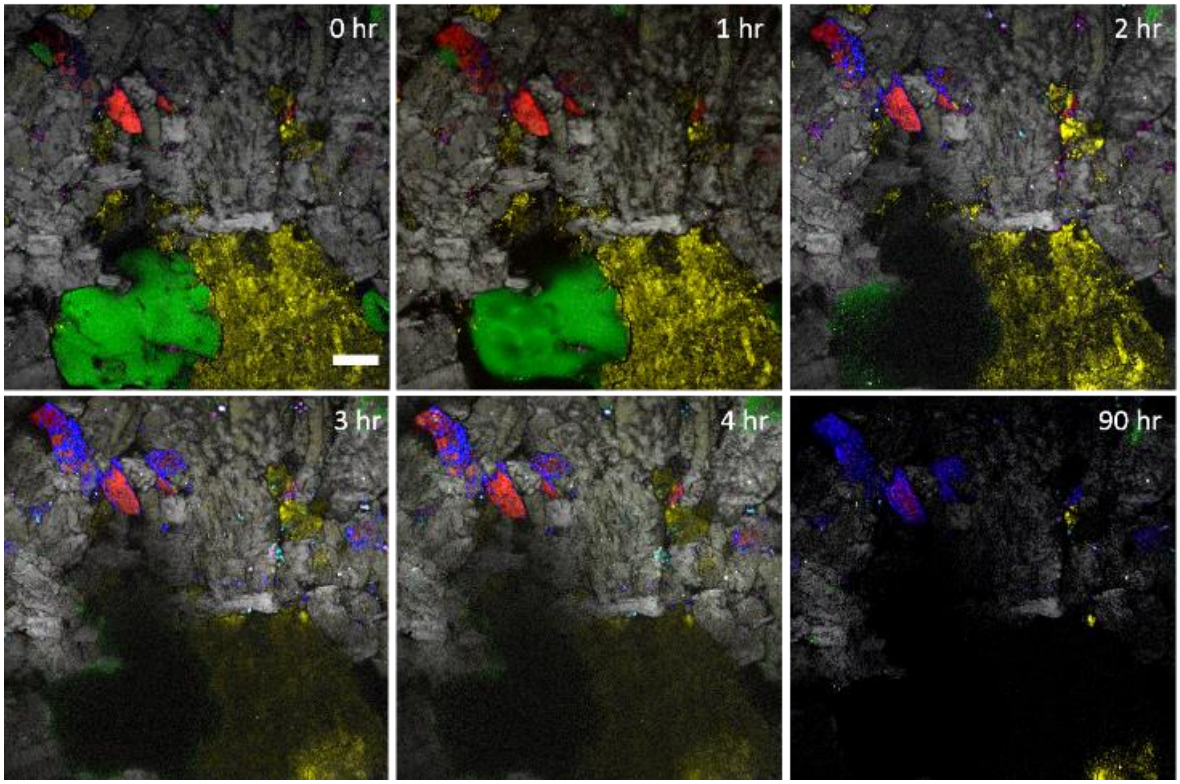

Figure 3.2 Time-lapse SRS imaging of a multicomponent tablet containing the API (PIO-HCl and PIO-FB in red and blue pixels, respectively), Mgst (magenta, stearic acid in cyan), crospovidone (green), mannitol (yellow), and avicel (grey). Scale bar = 30 μm.

observation of SRS signal from stearic acid (cyan colored pixels) still validates the proposed reaction (Eqn. 3.1). Our data suggests that this reaction occurs through a more indirect interaction (*vide infra*).

Another benefit of SRS microscopy is the ability to monitor the kinetics of various excipients which is valuable for characterizing pharmaceutical properties. For example, we observed that the crospovidone fragment gradually fades as is no longer detected after three hours. This phenomenon can be attributed to the fact that crosprovidone is used in formulation designs as a disintegrant to help release the API on contact with moisture. As crosprovidone swells, the density of packing is reduced and consequently the Raman signal decreases as a result of a smaller molecular density within the excitation volume (Fig. B.6). At 90 hrs, we observed that the overall signal across the

FOV decreased and can be attributed to crosprovidone swelling across the FOV. Therefore, hsSRS imaging can provide a comprehensive description of chemical concentration and distribution in heterogenous samples.

While the time lapse study provided clear evidence of increasing Pioglitazone disproportion over time, it is challenging to fully disentangle the influence of individual components within a multicomponent matrix that contribute to disproportionation, especially when their SRS spectra strongly overlaps with each other. This unfortunately leads to decreased predictive power in concentration mapping. To help elucidate the disproportionation mechanism, previous reports formulated binary mixtures to help reduce the spectral interference from inert excipient.[5,15,19,21] Thus for the following experiments we prepared binary mixtures of the problematic excipient and PIO-HCl. Furthermore, the binary tablets were prepared with the deuterated analog of Mgst to minimize the interference between the peaks of Mgst, stearic acid, PIO-FB, and PIO-HCl for robust data analysis (Table B.1, Fig. B.7).

Even though extensive studies are reported on the disproportionation kinetics in binary or multicomponent tablet formulations, the information obtained is only by bulk measurements and does not reveal either the spatial heterogeneity or the molecular mechanism behind disproportionation. It has been hypothesized that water can act as the medium for proton exchange between Mgst and PIO-HCl.[5,15,19,21] Visualization of water distribution (measured by fluorescence of rhodamine 6G) was previously used to help explain the spatial heterogeneity of disproportionation across the tablet surface when exposed stressed at 40° C/75% R.H.[21] While these results further confirmed the hypothesis that humidity plays a central role in the disproportionation kinetics, the direct correlation of water and disproportionation of PIO-HCl

along with Mgst has yet to be observed. We therefore examine this reaction at the microscopic level to determine which reaction pathway plays a dominant role in PIO disproportionation.

To this end, we first imaged the control tablets to examine the extent of the disproportionation reaction. Due to the reduced complexity of the system, we used a simple model of four compounds (PIO-FB, PIO-HCl, d-Mgst, and d-stearic acid to analyse the SRS hyperspectral imaging results (Fig. 3.3J). We examined the tablet in the spectral regions between 1560-1760 cm^{-1} and 2000-2200 cm^{-1}. In addition, to assess the influence of humidity on the disproportionation reaction, we obtained a single SRS image at the water Raman transition (3400 cm^{-1}). We imaged these SRS regions on a control tablet with a total of four different (FOV) across the surface of the tablet. The spectra were then fit using a non-negative least squares algorithm with the five basis spectra in Fig. 3.3J to provide a concentration map for each component. A representative FOV and the spectral decomposition results of the four compounds are shown in Fig. 3.3A-D. From the chemical mapping, we observe that a large portion of the image is composed of PIO-HCl (Fig. 3.3A), with a small fraction of the image composed of d-Mgst, which is validated by examining the spectra of pixels 1 and 2 (Fig. 3.3K) with respect to the basis spectra (Fig. 3.3J). From the chemical map generated for PIO-FB (Fig. 3.3B), it is observed that there is no detectable amount of free base, corroborating previous results that showed little to no PIO-FB when the tablet was not stressed. Furthermore, examining the merged channels of d-Mgst and d-stearic acid shows solely d-Mgst with no presence of d-stearic acid (Fig. 3.3C). This is expected since there should not be any d-stearic acid if the disproportionation reaction has not occurred. Lastly, it is apparent that there is no water signature detected on this tablet (Fig. 3.3D), which is unsurprising given the storage conditions.

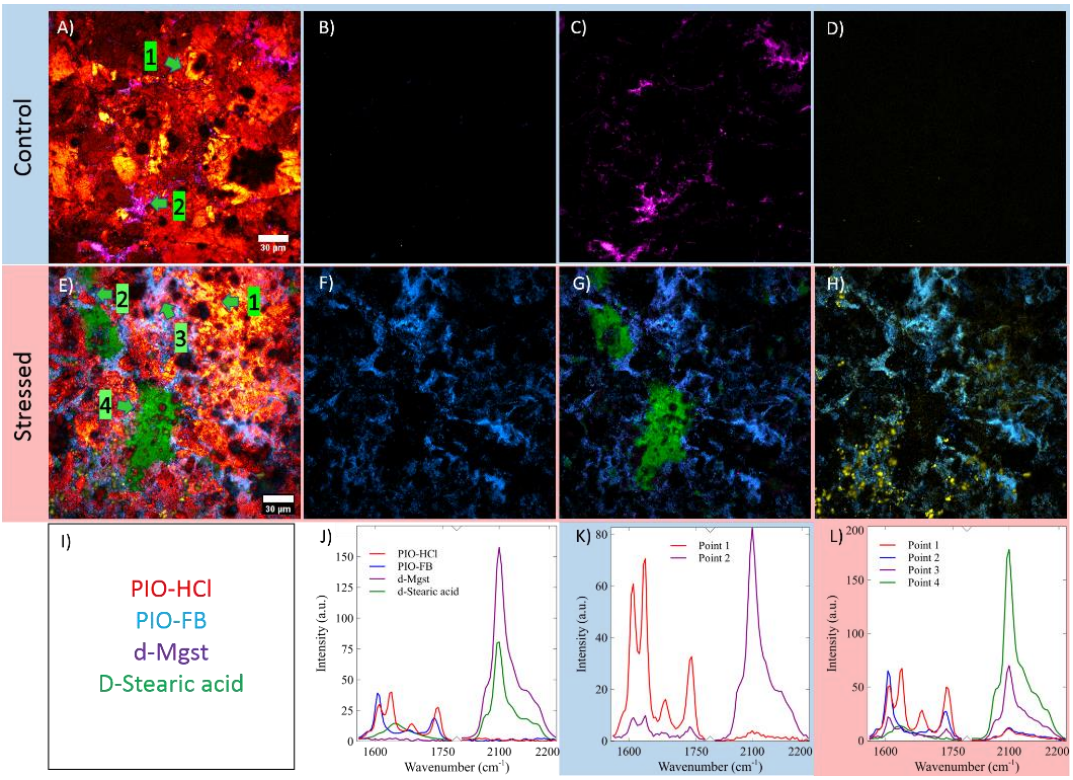

Figure 3.3 Comparison between control and stressed tablets. A) Nonnegative least-squares algorithm-derived chemical mapping of the four spectral components in the control tablet merged in a single frame B) Chemical mapping of PIO-FB. C) Merged chemical maps of d-Mgst and d-stearic acid. D). Merged SRS image of PIO-FB and water. E) Nonnegative least-squares algorithm-derived chemical mapping of the four spectral components in the stressed tablet merged in a single frame. F) Chemical mapping of PIO-FB. G) Merged chemical maps of PIO-FB, d-Mgst, and d-stearic acid. H) Merged SRS image of PIO-FB and water. I) Color scheme for chemical maps. J) SRS reference spectra. K) SRS spectra at two individual pixels in the control tablet (A-D). L) SRS spectra at four individual pixels in the stressed tablet (E-H).

To contrast with this condition, we then imaged the tablets stressed at 40° C/75% RH with a total of 4 different FOV across the surface of the tablet. A representative FOV and the spectral decomposition results for the four compounds are shown in Fig. 3.3E-H. From the chemical mapping, we still observe that a large portion of the image is composed of PIO-HCl (Fig. 3.3E). However, because the tablet was stressed, there is now a detectable signal from the free base which is interlaced between the matrix of the API (Figs. 3.3E and F). In addition, signal originating from d-stearic acid along with weaker signatures of d-Mgst are observable (Fig. 3.3G). The spectrum of

the selected points 1-4 (Fig. 3.3L) are again validated against the basis spectra from Fig. 3.3J. The merged channels of PIO-FB, d-Mgst, and d-stearic acid in Fig. 3.3G shows interesting results. It is hypothesized that colocalization of d-stearic acid and PIO-FB should occur due to the proton exchange in the disproportionation reaction.[19] In contrast, we observe PIO-FB to be randomly distributed across the matrix of the tablet with no apparent dependence on the location of d-stearic acid. It is apparent that the Raman signatures of water content exhibit large colocalization with PIO-FB, which provides direct evidence for the water mediated disproportionation reaction mechanism (Fig 3.3H).

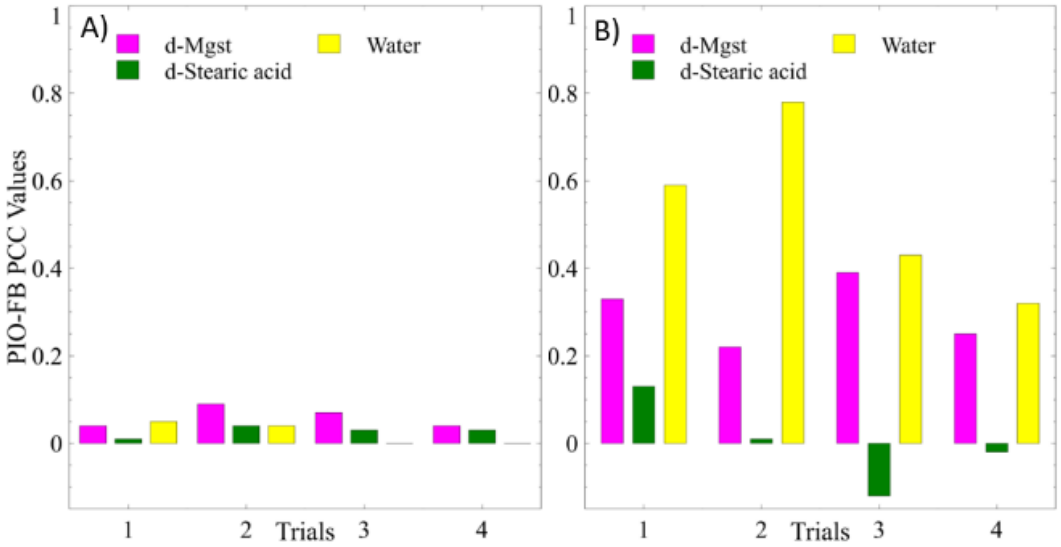

Figure 3.4 Quantitative colocalization analysis. PCC values of PIO-FB with d-Mgst, d-stearid acid, and water at several FOV across the A) unstressed tablet and B) stressed tablet.

To examine the mechanism of this reaction more quantitatively, we performed colocalization analyses that have been well-established in studies of objects and processes in dual-color confocal microscopy.[55–60] Among these measures, the Pearson correlation coefficient (PCC) is a robust statistical parameter that is often used to quantify colocalization. PCC values range from +1 for

two images whose intensities are perfectly correlated, 0 for no correlation, and -1 for perfectly anti-correlated images. Applying this analysis to the four FOVs in the unstressed tablet, we can quantify the amount of correlation (or lack thereof) between PIO-FB and d-Mgst as well as disproportionation by-products such as d-stearic acid and water. The PCC values are all relatively low (< 0.09) suggesting no correlation between PIO-FB and these components (Fig. 3.4A). The FOV shown in Fig. 3.3A-D is shown as trial 1 in Fig. 3.4A. For trials 1 and 2 we calculated the PCC values for PIO-FB and water as 0.05 and 0.04, respectively.

Applying the same quantitative approach to the stressed tablet reveals larger PCC values (> 0.25) highlighting correlation between the disproportionation reaction components and PIO-FB. We can observe that water has the highest PCC values with PIO-FB (max = 0.78), which again provides strong evidence suggesting that the salt disproportionation reaction is solution mediated through water (Fig. 3.4B). Interesting, we primarily see small and/or negative PCC values between PIO-FB and d-stearic acid. For example, in trial 3 (shown in Fig 3.3E-H), we see the largest negative PCC value of -0.12. This negative PCC value is attributed to the fact that sizable amounts of d-stearic acid are not colocalized with PIO-FB therefore exhibiting exclusive or anti-colocalization (Fig. 3.3G). These results further corroborate that the reaction is long range (mediated by solution) instead of local. Further colocalization analysis using Mander's Correlation Coefficient were employed and similar results were acquired (Fig. B.8). Additionally, analyzing the disproportionation of PIO-HCl as a function of depth in tablets revealed the penetration and migration of adsorbed water to be colocalized with PIO-FB (supplementary Fig. B.9). Together, these experimental evidences strongly support the conclusion that water is the dominant factor in salt disproportionation between PIO-HCl and d-Mgst by mediating proton transfer.

3.4 CONCLUSION

This study demonstrated the first example of SRS microscopy for investigating the chemical mechanism and molecular interplay between drug substance and excipients in pharmaceutical tablets. The fast imaging capability allows rapid chemical mapping of chemicals of interests in large samples, which is not possible with spontaneous Raman imaging. Together with chemometric analysis, hsSRS imaging provides a robust tool to quantify the chemical composition of drug tablets even at very low drug loading which was hitherto proven unsuccessful. To the best of our knowledge, this is the first demonstration of using deuterated analogs for Raman spectroscopy on pharmaceutical tablets. Contrary to the prevailing hypothesis in which near-field proton exchange is the dominant factor in disproportionation, our data suggests that this plays a small role in the overall reaction dynamics. By monitoring the presence and spatial dynamics of the disproportionation product d-stearic acid, we were able to elucidate the molecular mechanism behind the chemical reaction. This hypothesis is validated both qualitatively and quantitatively by the strong colocalization of water and free base.

Besides salt disproportionation, our study demonstrates the tremendous potential of hsSRS imaging to study other physicochemical changes in drug formulations such as phase changes, hydrolysis, oxidation, isomerization, photochemical decomposition, and polymerization, can be further implemented.[61] Furthermore, our hsSRS microscope can potentially provide accurate stability measurements of solids to accelerate advances in a wide range of research areas such as solid-state batteries, solar cells, and functional polymers.[62–6565]

Compared to the increasing use of SRS imaging in studying biological systems, SRS imaging of solid-state systems is still nascent with very few applications to date. Solids samples have sharp Raman peaks, requiring high spectral resolution to distinguish the various chemical components

in complex systems. Moreover, a multicomponent system typically involves many overlapping Raman peaks, creating challenging for quantification. The situation is even worse considering the fact that SRS signal is polarization dependent for crystalline samples. In our study, we used circularly polarized light and chemometrics to mitigate this issue. Another challenge in SRS imaging of solid-state system is that relevant processes involved often require harsher environments such as high temperature and humidity. Existing studies were limited to separate sample treatment and imaging, which not only creates challenges for spatial registration, but also decreases the temporal resolution of chemical imaging.[37,38] To overcome this problem, development of an *in situ* SRS imaging platform with full environmental control will be conducted in the future. With improvements in speed, resolution, specificity, and *in situ* imaging capability, SRS microscopy could become a powerful technological platform for spatiotemporally resolved characterization of chemical and physical changes of solid-state samples.

3.5 REFERENCES

(1) Lipinski, C. Poor Aqueous Solubility - An Industry Wide Problem in Drug Discovery. *Am Pharm Rev* **2002**, *5* (3), 82–85.

(2) Lipinski, C. A. Drug-like Properties and the Causes of Poor Solubility and Poor Permeability. *J Pharmacol Toxicol Methods* **2000**, *44* (1), 235–249.

(3) Gribbon, P.; Andreas, S. High-Throughput Drug Discovery: What Can We Expect from HTS? *Drug Discovery Today* **2005**, *10* (1), 17–22. https://doi.org/10.1016/S1359-6446(04)03275-1.

(4) Guerrieri, P.; Taylor, L. S. Role of Salt and Excipient Properties on Disproportionation in the Solid-State. *Pharm Res* **2009**, *26* (8), 2015–2026. https://doi.org/10.1007/s11095-009-9918-y.

(5) Nie, H.; Xu, W.; Ren, J.; Taylor, L. S.; Marsac, P. J.; John, C. T.; Byrn, S. R. Impact of Metallic Stearates on Disproportionation of Hydrochloride Salts of Weak Bases in Solid-State Formulations. *Mol. Pharmaceutics* **2016**, *13* (10), 3541–3552. https://doi.org/10.1021/acs.molpharmaceut.6b00630.

(6) Thakral, N. K.; Behme, R. J.; Aburub, A.; Peterson, J. A.; Woods, T. A.; Diseroad, B. A.; Suryanarayanan, R.; Stephenson, G. A. Salt Disproportionation in the Solid State: Role of Solubility and Counterion Volatility. *Mol. Pharmaceutics* **2016**, *13* (12), 4141–4151. https://doi.org/10.1021/acs.molpharmaceut.6b00745.

(7) Zhang, G. G. Z.; Law, D.; Schmitt, E. A.; Qiu, Y. Phase Transformation Considerations during Process Development and Manufacture of Solid Oral Dosage Forms. *Adv. Drug Deliv. Rev.* **2004**, *56* (3), 371–390. https://doi.org/10.1016/j.addr.2003.10.009.

(8) Saal, C.; Becker, A. Pharmaceutical Salts: A Summary on Doses of Salt Formers from the Orange Book. *Eur J Pharm Sci* **2013**, *49* (4), 614–623. https://doi.org/10.1016/j.ejps.2013.05.026.

(9) Pj, S.; D, Z. Disproportionation of a Crystalline Citrate Salt of a Developmental Pharmaceutical Compound: Characterization of the Kinetics Using PH Monitoring and Online Raman Spectroscopy plus Quantitation of the Crystalline Free Base Form in Binary Physical Mixtures Using FT-Raman, XRPD and DSC. *J Pharm Biomed Anal* **2014**, *90*, 186–191. https://doi.org/10.1016/j.jpba.2013.12.001.

(10) Stephenson, G. A.; Aburub, A.; Woods, T. A. Physical Stability of Salts of Weak Bases in the Solid-State. *JPharmSci* **2011**, *100* (5), 1607–1617. https://doi.org/10.1002/jps.22405.

(11) Williams, A. C.; Cooper, V. B.; Thomas, L.; Griffith, L. J.; Petts, C. R.; Booth, S. W. Evaluation of Drug Physical Form during Granulation, Tabletting and Storage. *International Journal of Pharmaceutics* **2004**, *275* (1), 29–39. https://doi.org/10.1016/j.ijpharm.2004.01.042.

(12) Rohrs, B. R.; Thamann, T. J.; Gao, P.; Stelzer, D. J.; Bergren, M. S.; Chao, R. S. Tablet Dissolution Affected by a Moisture Mediated Solid-State Interaction Between Drug and Disintegrant. *Pharm Res* **1999**, *16* (12), 1850–1856. https://doi.org/10.1023/A:1018951309506.

(13) Zannou, E. A.; Ji, Q.; Joshi, Y. M.; Serajuddin, A. T. M. Stabilization of the Maleate Salt of a Basic Drug by Adjustment of Microenvironmental PH in Solid Dosage Form. *International Journal of Pharmaceutics* **2007**, *337* (1), 210–218. https://doi.org/10.1016/j.ijpharm.2007.01.005.

(14) Preformulation in Solid Dosage Form Development 0824758099 | Acid Dissociation Constant | Physical Chemistry https://www.scribd.com/doc/118825655/Preformulation-in-Solid-Dosage-Form-Development-0824758099 (accessed Jun 26, 2017).
(15) John, C. T.; Xu, W.; Lupton, L. K.; Harmon, P. A. Formulating Weakly Basic HCl Salts: Relative Ability of Common Excipients to Induce Disproportionation and the Unique Deleterious Effects of Magnesium Stearate. *Pharm Res* **2013**, *30* (6), 1628–1641. https://doi.org/10.1007/s11095-013-1002-y.
(16) Christensen, N. P. A.; Rantanen, J.; Cornett, C.; Taylor, L. S. Disproportionation of the Calcium Salt of Atorvastatin in the Presence of Acidic Excipients. *Eur J Pharm Biopharm* **2012**, *82* (2), 410–416. https://doi.org/10.1016/j.ejpb.2012.07.003.
(17) Patel, M. A.; Luthra, S.; Shamblin, S. L.; Arora, K. K.; Krzyzaniak, J. F.; Taylor, L. S. Assessing the Risk of Salt Disproportionation Using Crystal Structure and Surface Topography Analysis. *Crystal Growth & Design* **2018**, *18* (11), 7027–7040. https://doi.org/10.1021/acs.cgd.8b01188.
(18) Patel, M. A.; Luthra, S.; Shamblin, S. L.; Arora, K.; Krzyzaniak, J. F.; Taylor, L. S. Impact of Solid-State Form on the Disproportionation of Miconazole Mesylate. *Mol. Pharmaceutics* **2018**, *15* (1), 40–52. https://doi.org/10.1021/acs.molpharmaceut.7b00694.
(19) Nie, H.; Liu, Z.; Marks, B. C.; Taylor, L. S.; Byrn, S. R.; Marsac, P. J. Analytical Approaches to Investigate Salt Disproportionation in Tablet Matrices by Raman Spectroscopy and Raman Mapping. *J Pharm Biomed Anal* **2016**, *118*, 328–337. https://doi.org/10.1016/j.jpba.2015.10.024.
(20) Nie, H.; Byrn, S. R.; Zhou, Q. (Tony). Stability of Pharmaceutical Salts in Solid Oral Dosage Forms. *Drug Development and Industrial Pharmacy* **2017**, *43* (8), 1215–1228. https://doi.org/10.1080/03639045.2017.1304960.
(21) Koranne, S.; Govindarajan, R.; Suryanarayanan, R. Investigation of Spatial Heterogeneity of Salt Disproportionation in Tablets by Synchrotron X-Ray Diffractometry. *Mol. Pharmaceutics* **2017**, *14* (4), 1133–1144. https://doi.org/10.1021/acs.molpharmaceut.6b01052.
(22) Hirsh, D. A.; Su, Y.; Nie, H.; Xu, W.; Stueber, D.; Variankaval, N.; Schurko, R. W. Quantifying Disproportionation in Pharmaceutical Formulations with 35Cl Solid-State NMR. *Mol. Pharmaceutics* **2018**, *15* (9), 4038–4048. https://doi.org/10.1021/acs.molpharmaceut.8b00470.
(23) Rasouli, N.; Raue, U.; Miles, L. M.; Lu, T.; Gregorio, G. B. D.; Elbein, S. C.; Kern, P. A. Pioglitazone Improves Insulin Sensitivity through Reduction in Muscle Lipid and Redistribution of Lipid into Adipose Tissue. *American Journal of Physiology - Endocrinology and Metabolism* **2005**, *288* (5), E930–E934. https://doi.org/10.1152/ajpendo.00522.2004.
(24) Sanrame, C. N.; Remenar, J. F.; Blumberg, L. C.; Waters, J.; Dean, R. L.; Dong, N.; Kriksciukaite, K.; Cao, P.; Almarsson, O. Prodrugs of Pioglitazone for Extended-Release (XR) Injectable Formulations. *Mol. Pharm.* **2014**, *11* (10), 3617–3623. https://doi.org/10.1021/mp500359a.
(25) Jamrógiewicz, M. Consequences of New Approach to Chemical Stability Tests to Active Pharmaceutical Ingredients. *Front Pharmacol* **2016**, *7*. https://doi.org/10.3389/fphar.2016.00017.

(26) Merritt, J. M.; Viswanath, S. K.; Stephenson, G. A. Implementing Quality by Design in Pharmaceutical Salt Selection: A Modeling Approach to Understanding Disproportionation. *Pharmaceutical research* **2013**, *30* (1), 203–217.
(27) Freudiger, C. W.; Min, W.; Saar, B. G.; Lu, S.; Holtom, G. R.; He, C.; Tsai, J. C.; Kang, J. X.; Xie, X. S. Label-Free Biomedical Imaging with High Sensitivity by Stimulated Raman Scattering Microscopy. *Science* **2008**, *322* (5909), 1857–1861. https://doi.org/10.1126/science.1165758.
(28) Camp Jr, C. H.; Cicerone, M. T. Chemically Sensitive Bioimaging with Coherent Raman Scattering. *Nat Photon* **2015**, *9* (5), 295–305. https://doi.org/10.1038/nphoton.2015.60.
(29) Saar, B. G.; Freudiger, C. W.; Reichman, J.; Stanley, C. M.; Holtom, G. R.; Xie, X. S. Video-Rate Molecular Imaging in Vivo with Stimulated Raman Scattering. *Science* **2010**, *330* (6009), 1368–1370. https://doi.org/10.1126/science.1197236.
(30) Cheng, J.-X.; Xie, X. S. Coherent Anti-Stokes Raman Scattering Microscopy: Instrumentation, Theory, and Applications. *J. Phys. Chem. B* **2004**, *108* (3), 827–840. https://doi.org/10.1021/jp035693v.
(31) Evans, C. L.; Xie, X. S. Coherent Anti-Stokes Raman Scattering Microscopy: Chemical Imaging for Biology and Medicine. *Annu. Rev. Anal. Chem.* **2008**, *1* (1), 883–909. https://doi.org/10.1146/annurev.anchem.1.031207.112754.
(32) Fussell, A. L.; Kleinebudde, P.; Herek, J.; Strachan, C. J.; Offerhaus, H. L. Coherent Anti-Stokes Raman Scattering (CARS) Microscopy Visualizes Pharmaceutical Tablets During Dissolution. *J Vis Exp* **2014**, No. 89. https://doi.org/10.3791/51847.
(33) Kang, E.; Wang, H.; Kwon, I. K.; Song, Y.-H.; Kamath, K.; Miller, K. M.; Barry, J.; Cheng, J.-X.; Park, K. Application of Coherent Anti-Stokes Raman Scattering Microscopy to Image the Changes in a Paclitaxel–Poly(Styrene-b-Isobutylene-b-Styrene) Matrix Pre- and Post-Drug Elution. *Journal of Biomedical Materials Research Part A* **2008**, *87A* (4), 913–920. https://doi.org/10.1002/jbm.a.31813.
(34) Fussell, A. L.; Grasmeijer, F.; Frijlink, H. W.; Boer, A. H. de; Offerhaus, H. L. CARS Microscopy as a Tool for Studying the Distribution of Micronised Drugs in Adhesive Mixtures for Inhalation. *Journal of Raman Spectroscopy* **2014**, *45* (7), 495–500. https://doi.org/10.1002/jrs.4515.
(35) Kang, E.; Wang, H.; Kwon, I. K.; Robinson, J.; Park, K.; Cheng, J.-X. In Situ Visualization of Paclitaxel Distribution and Release by Coherent Anti-Stokes Raman Scattering Microscopy. *Anal. Chem.* **2006**, *78* (23), 8036–8043. https://doi.org/10.1021/ac061218s.
(36) Kang, E.; Robinson, J.; Park, K.; Cheng, J.-X. Paclitaxel Distribution in Poly(Ethylene Glycol) / Poly(Lactide-Co-Glycolic Acid) Blends and Its Release Visualized by Coherent Anti-Stokes Raman Scattering Microscopy. *J Control Release* **2007**, *122* (3), 261–268. https://doi.org/10.1016/j.jconrel.2007.05.007.
(37) Windbergs, M.; Jurna, M.; Offerhaus, H. L.; Herek, J. L.; Kleinebudde, P.; Strachan, C. J. Chemical Imaging of Oral Solid Dosage Forms and Changes upon Dissolution Using Coherent Anti-Stokes Raman Scattering Microscopy. *Anal. Chem.* **2009**, *81* (6), 2085–2091. https://doi.org/10.1021/ac8020856.
(38) Fussell, A.; Garbacik, E.; Offerhaus, H.; Kleinebudde, P.; Strachan, C. In Situ Dissolution Analysis Using Coherent Anti-Stokes Raman Scattering (CARS) and Hyperspectral CARS Microscopy. *European Journal of Pharmaceutics and Biopharmaceutics* **2013**, *85* (3, Part B), 1141–1147. https://doi.org/10.1016/j.ejpb.2013.08.012.

(39) Francis, A. T.; Nguyen, T. T.; Lamm, M. S.; Teller, R.; Forster, S. P.; Xu, W.; Rhodes, T.; Smith, R. L.; Kuiper, J.; Su, Y.; Fu, D. In Situ Stimulated Raman Scattering (SRS) Microscopy Study of the Dissolution of Sustained-Release Implant Formulation. *Mol. Pharmaceutics* **2018**. https://doi.org/10.1021/acs.molpharmaceut.8b00965.

(40) N. Slipchenko, M.; Chen, H.; R. Ely, D.; Jung, Y.; Teresa Carvajal, M.; Cheng, J.-X. Vibrational Imaging of Tablets by Epi-Detected Stimulated Raman Scattering Microscopy. *Analyst* **2010**, *135* (10), 2613–2619. https://doi.org/10.1039/C0AN00252F.

(41) Cheng, J.-X.; Xie, X. S. Vibrational Spectroscopic Imaging of Living Systems: An Emerging Platform for Biology and Medicine. *Science* **2015**, *350* (6264), aaa8870. https://doi.org/10.1126/science.aaa8870.

(42) Min, W.; Freudiger, C. W.; Lu, S.; Xie, X. S. Coherent Nonlinear Optical Imaging: Beyond Fluorescence Microscopy. *Annual Review of Physical Chemistry* **2011**, *62* (1), 507–530. https://doi.org/10.1146/annurev.physchem.012809.103512.

(43) Magnesium stearate CAS#: 557-04-0 https://www.chemicalbook.com/ProductChemicalPropertiesCB5330900_EN.htm (accessed Dec 7, 2018).

(44) Figueroa, B.; Chen, Y.; Berry, K.; Francis, A.; Fu, D. Label-Free Chemical Imaging of Latent Fingerprints with Stimulated Raman Scattering Microscopy. *Anal. Chem.* **2017**, *89* (8), 4468–4473. https://doi.org/10.1021/acs.analchem.6b04213.

(45) Lai, M.; Lai, S. T.; Swinger, C. Single-Grating Laser Pulse Stretcher and Compressor. *Appl. Opt., AO* **1994**, *33* (30), 6985–6987. https://doi.org/10.1364/AO.33.006985.

(46) Pessot, M.; Maine, P.; Mourou, G. 1000 Times Expansion/Compression of Optical Pulses for Chirped Pulse Amplification. *Optics Communications* **1987**, *62* (6), 419–421. https://doi.org/10.1016/0030-4018(87)90011-3.

(47) Fu, D.; Holtom, G.; Freudiger, C.; Zhang, X.; Xie, X. S. Fast Hyperspectral Imaging with Stimulated Raman Scattering by Chirped Femtosecond Lasers. *J Phys Chem B* **2013**, *117* (16), 4634–4640. https://doi.org/10.1021/jp308938t.

(48) Fortunato de Carvalho Rocha, W.; Sabin, G. P.; Março, P. H.; Poppi, R. J. Quantitative Analysis of Piroxicam Polymorphs Pharmaceutical Mixtures by Hyperspectral Imaging and Chemometrics. *Chemometrics and Intelligent Laboratory Systems* **2011**, *106* (2), 198–204. https://doi.org/10.1016/j.chemolab.2010.04.015.

(49) Ravn, C.; Skibsted, E.; Bro, R. Near-Infrared Chemical Imaging (NIR-CI) on Pharmaceutical Solid Dosage Forms—Comparing Common Calibration Approaches. *Journal of Pharmaceutical and Biomedical Analysis* **2008**, *48* (3), 554–561. https://doi.org/10.1016/j.jpba.2008.07.019.

(50) Martens, H.; Næs, T. Multivariate Calibration. In *Chemometrics*; NATO ASI Series; Springer, Dordrecht, 1984; pp 147–156. https://doi.org/10.1007/978-94-017-1026-8_5.

(51) Wold, S.; Sjöström, M.; Eriksson, L. PLS-Regression: A Basic Tool of Chemometrics. *Chemometrics and Intelligent Laboratory Systems* **2001**, *58* (2), 109–130. https://doi.org/10.1016/S0169-7439(01)00155-1.

(52) Gowen, A. A.; Downey, G.; Esquerre, C.; O'Donnell, C. P. Preventing Over-Fitting in PLS Calibration Models of near-Infrared (NIR) Spectroscopy Data Using Regression Coefficients. *Journal of Chemometrics 25* (7), 375–381. https://doi.org/10.1002/cem.1349.

(53) Stahl, P. H.; Heinrich, C. G. *Pharmaceutical Salts: Properties, Selection, and Use, 2nd Revised Edition*; Wiley, 2011.

(54) Zimmermann, T.; Rietdorf, J.; Pepperkok, R. Spectral Imaging and Its Applications in Live Cell Microscopy. *FEBS Lett.* **2003**, *546* (1), 87–92.
(55) Manders, E. M. M.; Verbeek, F. J.; Aten, J. A. Measurement of Co-Localization of Objects in Dual-Colour Confocal Images. *Journal of Microscopy* **1993**, *169* (3), 375–382. https://doi.org/10.1111/j.1365-2818.1993.tb03313.x.
(56) Costes, S. V.; Daelemans, D.; Cho, E. H.; Dobbin, Z.; Pavlakis, G.; Lockett, S. Automatic and Quantitative Measurement of Protein-Protein Colocalization in Live Cells. *Biophys. J.* **2004**, *86* (6), 3993–4003. https://doi.org/10.1529/biophysj.103.038422.
(57) Bolte, S.; Cordelières, F. P. A Guided Tour into Subcellular Colocalization Analysis in Light Microscopy. *Journal of Microscopy* **2006**, *224* (3), 213–232. https://doi.org/10.1111/j.1365-2818.2006.01706.x.
(58) Dunn, K. W.; Kamocka, M. M.; McDonald, J. H. A Practical Guide to Evaluating Colocalization in Biological Microscopy. *Am J Physiol Cell Physiol* **2011**, *300* (4), C723–C742. https://doi.org/10.1152/ajpcell.00462.2010.
(59) Krauß, S. D.; Petersen, D.; Niedieker, D.; Fricke, I.; Freier, E.; El-Mashtoly, S. F.; Gerwert, K.; Mosig, A. Colocalization of Fluorescence and Raman Microscopic Images for the Identification of Subcellular Compartments: A Validation Study. *The Analyst* **2015**, *140* (7), 2360–2368. https://doi.org/10.1039/C4AN02153C.
(60) El-Mashtoly, S. F.; Niedieker, D.; Petersen, D.; Krauss, S. D.; Freier, E.; Maghnouj, A.; Mosig, A.; Hahn, S.; Kötting, C.; Gerwert, K. Automated Identification of Subcellular Organelles by Coherent Anti-Stokes Raman Scattering. *Biophysical Journal* **2014**, *106* (9), 1910. https://doi.org/10.1016/j.bpj.2014.03.025.
(61) Narang, A. S.; Desai, D.; Badawy, S. Impact of Excipient Interactions on Solid Dosage Form Stability. *Pharm Res* **2012**, *29* (10), 2660–2683. https://doi.org/10.1007/s11095-012-0782-9.
(62) Kerman, K.; Luntz, A.; Viswanathan, V.; Chiang, Y.-M.; Chen, Z. Review—Practical Challenges Hindering the Development of Solid State Li Ion Batteries. *J. Electrochem. Soc.* **2017**, *164* (7), A1731–A1744. https://doi.org/10.1149/2.1571707jes.
(63) Niu, G.; Guo, X.; Wang, L. Review of Recent Progress in Chemical Stability of Perovskite Solar Cells. *J. Mater. Chem. A* **2015**, *3* (17), 8970–8980. https://doi.org/10.1039/C4TA04994B.
(64) Guo, Y.; Shalaev, E.; Smith, S. Physical Stability of Pharmaceutical Formulations: Solid-State Characterization of Amorphous Dispersions. *TrAC Trends in Analytical Chemistry* **2013**, *49*, 137–144. https://doi.org/10.1016/j.trac.2013.06.002.
(65) Cheng, Q.; Wei, L.; Liu, Z.; Ni, N.; Sang, Z.; Zhu, B.; Xu, W.; Chen, M.; Miao, Y.; Chen, L.-Q.; Min, W.; Yang, Y. Operando and Three-Dimensional Visualization of Anion Depletion and Lithium Growth by Stimulated Raman Scattering Microscopy. *Nature Communications* **2018**, *9* (1), 2942. https://doi.org/10.1038/s41467-018-05289-z.

Chapter 4: Broadband Hyperspectral Stimulated Raman Scattering Microscopy with a Parabolic Fiber Amplifier Source

The work presented in this chapter has been published in the following paper:
*1) Figueroa, B.; Fu, W.; Nguyen, T.; Shin, K.; Manifold, B.; Wise, F.; Fu, D. "Broadband Hyperspectral Stimulated Raman Scattering Microscopy with a Parabolic Fiber Amplifier Source" Biomedical Optics Express **2018**, 9, 12, 6116-6131*

4.1 INTRODUCTION

Optical microscopy has become a fundamental and indispensable tool for biomedical research. Because biological systems are heterogeneous at all scales, chemical imaging capable of probing a vast range of molecules *in situ* is becoming increasingly important [1]. Raman spectroscopy is a powerful technique for non-invasive characterization of biological material through their intrinsic molecular vibrational contrasts. Extending this capability to microscopy, a Raman microscope becomes especially useful for the study of biological samples [2–4]. However, the extremely small cross section of spontaneous Raman scattering, makes it unsuitable for high-speed imaging. To address this limitation, Coherent anti-Stokes Raman scattering (CARS) has been developed, which offers orders-of-magnitude higher sensitivity and video-rate imaging [5–7]. However, it has a well-known nonresonant background problem which originates from a four-wave mixing process that distorts vibrational spectra and causes image artifacts [7,8]. Developments in CARS microscopy have mitigated the nonresonant background problem by optimizing experiment procedures and post-image data processing [9–11]. In particular, broadband CARS microscopy followed by phase retrieval has significantly advanced the capability of CARS imaging [12]. In parallel development, stimulated Raman scattering (SRS) microscopy has emerged as an alternative to CARS as a powerful non-destructive and label-free chemical imaging technique [13–21]. It has shown tremendous potential in detecting tumor margins [22–24], unraveling dysregulated lipid metabolism [25,26], and tracing small molecule metabolites and drugs [27–31]. These capabilities benefit from the high sensitivity of SRS

imaging as well as the molecular selectivity of Raman spectroscopy. In both CARS and SRS microscopy, two synchronized, ultrashort laser pulses (pump and Stokes) are focused tightly onto a sample. The energy difference between the two pulses coherently excites an intrinsic Raman vibrational mode allowing for chemically selective imaging. The growing popularity of SRS microscopy over CARS stems from the fact that, unlike CARS, SRS inherently removes the nonresonant background and has a strict linear relationship with molecular concentration, thus facilitating quantitative chemical imaging [14,21]. In comparison, quantitative CARS through background removal (typically using phase retrieval) is a nontrivial task [8]. However, CARS has a major advantage over SRS in that broadband Raman spectra can be easily acquired at high speed due to its lock-in free detection scheme and resistance to laser intensity noise. In fact, this is one of the major limitations of SRS. High resolution and broadband vibrational spectra are of paramount importance to resolve minute chemical composition variation in biological samples and detect small molecules. To differentiate and quantify different molecules based on their unique vibrational signatures, multiple Raman transitions must be probed with SRS, necessitating the use of multiplex SRS or hsSRS imaging [32–36].

In a typical SRS microscopy setup, transform-limited picosecond lasers with narrow bandwidths, which are less than the Raman line widths (<10 cm^{-1}), are used to probe Raman-active vibrations of interest with high spectral resolution. To probe a different transition, the energy difference between the two pulses must be tuned by changing one of the two wavelengths. This tuning process typically involves changing the crystal temperature or cavity length of the optical parametric oscillator [23,37]. Additionally, only a limited wavelength range can be scanned without time-consuming adjustments. In practice, wavelength tuning of typical laser sources is usually slow and

susceptible to optical power and wavelength drifts, which limits the acquisition speed and quantification accuracy of SRS imaging.

Another way to acquire spectroscopic information is to employ a combination of picosecond and femtosecond laser sources. This can be achieved with either a grating based spectrometer or Fourier-transform spectrometer [38,39]. With this method, imaging at 4 μs per spectrum can be achieved, enabling applications in flow cytometry. While pico-femto based SRS imaging approaches work well for simple systems, the complicated instrumentation and limited sensitivity restrain their use mostly to SRS imaging in the C-H imaging for lipids and proteins. One reason for the limited sensitivity is that the optical power is distributed among many Raman vibrational modes so that each Raman transition is less efficient than that of SRS excitation with picosecond lasers.

An alternative approach to SRS excitation with picosecond lasers is SRS imaging with femtosecond lasers and the "spectral-focusing" approach [35,36,40–45]. The spectral focusing approach offers much higher spectral resolution than direct femtosecond laser excitation by sending the pulses through a dispersive medium. This introduces linear chirp through the temporal spreading of the frequency components of the two femtosecond excitation sources, leading to narrower instantaneous bandwidths. Tuning different vibrational frequencies within the range of the broad laser bandwidth is done by simply varying the temporal delay between the two chirped pulses. Early reports have demonstrated the capability of employing the spectral focusing approach for SRS using a femtosecond oscillator and a fiber-generated secondary source [35,41]. However, in these reports, the low power output from the fiber limited the acquisition sensitivity and imaging speed.

In either pico-femto or femto-femto SRS imaging, suitable synchronized laser sources are required. The introduction of the commercial dual output femtosecond lasers such as the Insight

DS+ (SpectraPhysics) offers a robust and simple solution to the excitation laser requirement. Such systems are advantageous compared to Ti:sapphire and fiber based laser systems because of their simple tuning, high power, and synchronization stability. Thus, it is becoming the leading laser source for hsSRS imaging. The laser outputs a fixed 1040 nm laser with ~60 cm-^{1} bandwidth and a tunable laser with ~150 cm^{-1} bandwidth. In both pico-femto and femto-femto hsSRS configurations, the spectral coverage of SRS is limited by the spectral bandwidths of the laser sources. With Insight DS+, it is limited to <300 cm^{-1}. Additionally, the spectral resolution of most current systems is limited to ~20-25 cm^{-1} [46,47]. While these capabilities are often sufficient for imaging in the high wavenumber region (2800-3050 cm^{-1}), they are insufficient for imaging in the fingerprint region (700-1800 cm^{-1}).

SRS imaging spanning a large spectral range is under intense technical development. Beier et al. demonstrated the acquisition of a reliable Raman spectrum over a large spectral range using a supercontinuum generated by a photonic crystal fiber as either the pump or the Stokes beam [41]. However, this approach suffers from low signal-to-noise ratio (SNR) due to two reasons: (1) large bandwidth mismatch and (2) low power output from the fiber, which significantly limit the imaging speed to (3 ms/pixel). Most recently, Karpf et al. developed a broadband SRS time-encoded technique using rapidly wavelength-swept continuous wave probe lasers combined with a short-duty-cycle actively modulated pump laser[48]. High speed, broad spectral coverage (750-3150 cm^{-1}) and high resolution were achieved in this, albeit, complex configuration. However, the low power output limited the system's sensitivity and with it the imaging speed to achieve a sufficient SNR (250 μs per spectral point).

In this manuscript, we present a simple and novel approach for broadband hsSRS imaging based on parabolic pulse amplification, which offers increased spectral range and spectral resolution [49].

It has been shown that propagating an ultrashort pulse through a sufficiently long, normally-dispersive fiber amplifier results in a linearly chirped parabolic pulse, which is the asymptotic self-similar solution of the nonlinear Schrodinger equation with gain [50–53]. In addition, it is within this self-similar regime that the seed pulse spectrum will be significantly broadened due to self-phase modulation. It is important to note, however, that additional higher-order linear or nonlinear effects may occur and ultimately limit the propagation length of the parabolic pulses and/or introduce parasitic effects [54–56]. Nonetheless, numerous studies have performed numerical and experimental studies which provide a series of guidelines in determining the design of fiber amplifiers to operate in the asymptotic parabolic pulse regime [52,53,57,58].

Besides spectral broadening, parabolic amplification has two noteworthy properties: (1) the peak power, duration, and shape of the resulting pulses depend only on the seed pulse energy and (2) the output pulse has nearly perfect linear up-chirp. As a result, linearly chirped pulses with ~50 nm (or 500 cm^{-1}) bandwidth centered around 1050 nm can be readily obtained. In combination with the existing pump pulse provided by the Insight DS+, a 650 cm^{-1} spectral range, a 2-fold increase over our previous system, can be covered by hsSRS without changing laser wavelength. Due to the increased bandwidth, the Stokes laser will also be much longer in pulse duration after chirping, leading to improved spectral resolution. To optimize the spectral resolution, the linear chirp of the pump and the Stokes are matched. We achieve and demonstrate that a maximum spectral resolution of 10 cm^{-1} is possible when the chirps of the excitation beams are properly matched. We then validate the benefit of employing parabolic pulse amplification on our system by the hsSRS imaging of mammalian cells and brain tissue.

4.2 MATERIALS AND METHODS

4.2.1 Chemical and Materials

Reagent grade methanol, oleic acid, benzonitrile, nitrobenzene, dimethyl sulfoxide (DMSO), hydrochloride acid, and insulin were all purchased from Sigma-Aldrich (St. Lous, MO) with purity ≥ 95%. Glass slides were purchased from VWR (Radnor, PA). Glass coverslips are from Thermo Scientific (Porthsmouth, NH).

4.2.2 Cell Culture

Human embryonic kidney (HEK293) cells were maintained at 37˚ C in a humidified 5% (vol/vol) CO2 air incubator and cultured in DMEM (Invitrogen Carlsbad, CA) supplemented with 10% (vol/vol) FBS and 1% (vol/vol) penicillin/streptomycin. Before imaging, HEK293 cells were seeded on glass cover slips and fixed with 4% paraformaldehyde (PFA) for 30 minutes.

4.2.3 Insulin Fibrils Control Samples

10 mg of insulin was placed into 4 ml of HCl. The solution was mixed at 300 rpm in a water bath kept at a constant temperature of 70˚ C for 18 hours to induce the fibril formation. The final sample was centrifuged for 5 minutes to isolate fibrils from dissolved insulin. The insulin fibril sample was mounted on a glass slide and a coverslip was added prior to imaging.

4.2.4 Alzheimer's brain samples

Brain tissue from a donor was provided by University of Washington Neuropathology Core, Seattle, WA. A superior temporal gyrus brain tissue was collected less than 8 hours of postmortem interval, fixed in 10% neutrally buffered formalin solution. A cross section through cortex and white matter at ~500 μm was mounted on a glass slide and a coverslip was added prior to imaging.

4.2.5 Hyperspectral SRS Imaging with a Parabolic Fiber Amplifier

A broadband femtosecond dual beam laser system (Insight DS+ from Spectra-Physics) was used for hsSRS imaging as described in our earlier publication [46,59]. Figure 4.1 shows our experimental setup. The Stokes beam is coupled into a 4-m polarization maintaining Yb-doped fiber (YB1200-6/125 DC-PM Thorlabs) with a beam collimator and acts as the seed for laser amplification. An input pulse seed energy of 25 pJ was used for amplification throughout this entire study which ensures convergence to the parabolic regime [51–53,58]. A half wave plate was placed at the input to optimize polarization of the seed pulse transmitting through the fiber. The gain fiber is then pumped in the counter-propagation pumping scheme by a 976-nm high power laser diode (BWT) and combined with the seed using a wavelength division multiplexer with a power rating of 7 W (PMC02112340 IFT Technologies). An electro-optical modulator is then placed in the amplified Stokes beam, modulating at 20 MHz. A motorized delay line is inserted into the Stokes beam to scan the time delay between the pump and the Stokes. After collinearly recombining the two beams through the dichroic mirror DMSP1000 (Thorlabs), the beams were directed in to a home-built laser scanning microscope (NIKON Eclipse FN1). An Olympus microscope objective of 25× (XLPLN25XWMP2) with 1.05 NA was used to focus the beams onto the samples. On the detection side, the Stokes beam is filtered out by a short–pass filter FESH1000 (Thorlabs), and the pump beam is detected by a 10 × 10 mm^2 silicon photodiode (Hamamatsu) biased at 56 V and then amplified by a home-built transimpedance amplifier. Stimulated Raman loss (SRL) signal is detected with a Zurich Instruments lock-in amplifier (H2FLI). For SRS imaging, the lock-in time constant is at 8 μs and each frame is 512 × 512 pixels with 0.5 frame/sec acquisition speed, unless noted otherwise.

For hsSRS imaging with spectral focusing, the pump beam is chirped by a grating stretcher in quadruple-pass configuration [60,61] while the amplified Stokes pulse is chirped further by 36 cm of

high dispersion H-ZF52A glass rods to appropriately match the chirp of the pump beam. To compare the imaging capability of the new laser system versus the old laser system, a spectral-focusing SRS setup with outputs directly from the Insight laser was employed. In this setup, the pump is chirped by 60 cm of high dispersion glass rods, while the Stokes is chirped by a grating stretcher setup.

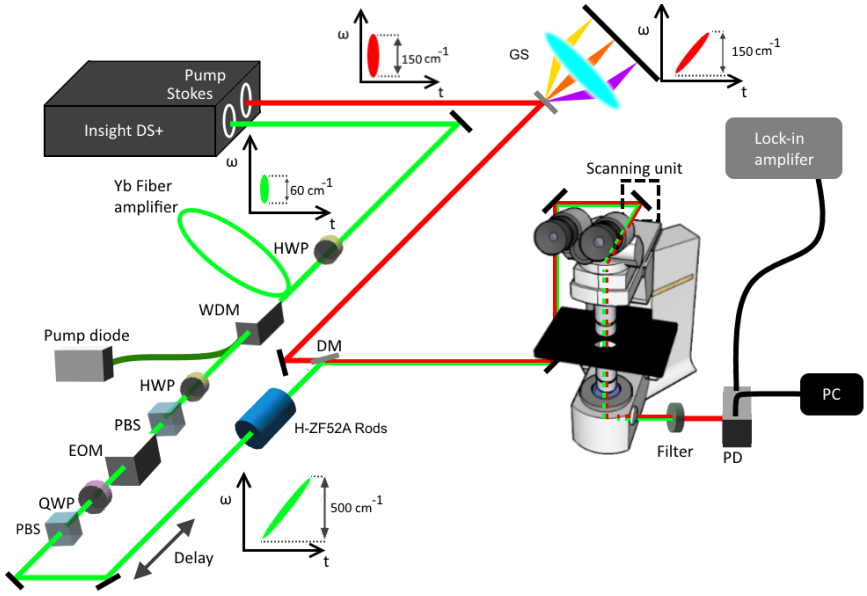

Figure 4.1 Schematic diagram of the hsSRS imaging setup based on a femtosecond dual beam laser system. Abbreviations: GS, grating-stretcher; HWP, half waveplate; WDM, wavelength division multiplexer; PBS, polarizing beam splitter; EOM, electro-optical modulator; QWP, quarter waveplate; DM, dichroic mirror; PD, photodiode.

4.3 RESULTS AND DISCUSSION

We first measured the pulse properties of the parabolic fiber amplifier output. Seeding the fiber amplifier with 2 mW (25 pJ) of ~280 fs pulses, ensures the generation of linearly chirped parabolic pules which experience large temporal and spectral broadening as can be seen in Fig. 4.2. From Fig. 4.2A and B it is apparent that the spectrum of the amplified Stokes pulses increases in an almost linear fashion with only large amplification showing deviation from linearity (7 W). The ability to tune to different bandwidths solely by changing the 976 nm pump power that is launched

into the fiber provides a quick and easy tool for various applications as will be shown later. Likewise, the pulse width of the Stokes pulse significantly broadens from the nearly transform-limited input seed pulse (Fig. 4.2B). Although a linear increase in pulse width is exhibited, an exponential increase in pulse widths is expected from the parabolic output [50–53,58]. We hypothesize that this is due to the addition of the 36 cm of dispersion glass rods used for matching the chirp rates between the pump and Stokes for SRS imaging, and therefore could be masking the exponential increase that is expected. Another additional benefit of employing parabolic amplification is the production of up to 2.5 W average output power which is more than plenty of optical power for hsSRS imaging, which therefore does not experience the limitations characteristic of other broadband SRS setups.[35,41,48] The slope efficiency is about 43% with respect to the absorbed pump power which is shown in Fig. 4.2C. With these improvements, increased spectral resolution and spectral coverage is expected due the enlarged pulse width and bandwidth of the Stokes beam.

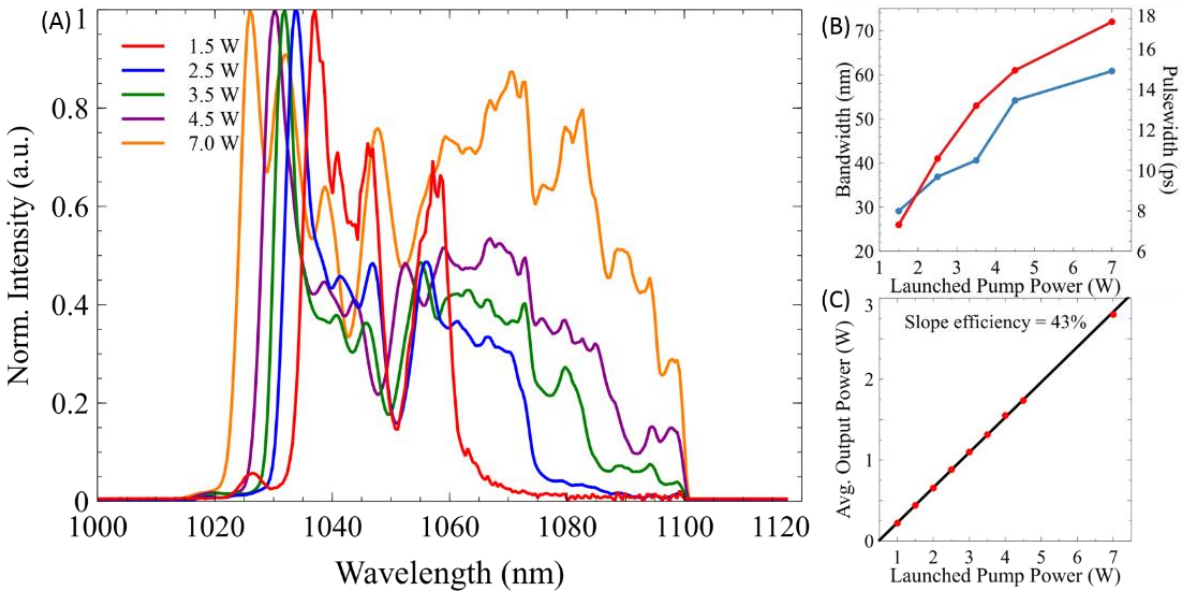

Figure 4.2 A) The optical spectra of the Stokes pulse in a parabolic fiber amplifier as a function of launched pump power. B) The bandwidth at FWHM (red) and pulse width (blue) of the amplified pulse after the 336 cm of glass rods as a function of launched pump power. C) Output power characteristics of the parabolic fiber amplifier.

To demonstrate the benefit of employing parabolic pulse amplification for increased SRS spectral coverage, SRS spectra of various organic solvents were taken using the traditional SRS setup and compared with results from the fiber amplifier setup. The spectral region of interest that would most benefit from the increased spectral coverage is the so-called "fingerprint region." Sharp Raman vibrational modes in this region provide particularly valuable information for molecular identification. We first demonstrated the limitations of our previous SRS setup to probe the entire fingerprint region (Fig. 4.3A). We measured the SRS spectra by recording the SRS signal while scanning the interpulse time delay between the pump and the unamplified Stokes beam. The pump beam was tuned to 916 nm to center our probed Raman spectra at 1300 cm^{-1}. Fig. 4.3A shows the SRS spectra of oleic acid, nitrobenzene, benzonitrile, and methanol collected with 220 spectral points with each point acquired with a 100 μs pixel dwell time. Here the spectral range is limited by the bandwidth of the femtosecond laser beams to ~ 300 cm^{-1}. Due to the limited bandwidth of the pump and Stokes lasers, it is evident that tuning of the pump beam to scan throughout the fingerprint region (700 – 1700 cm^{-1}) is unavoidable and requires a minimum of 4 different pump excitation frequencies, with each wavelength change requiring several seconds for stabilization. In addition, the spectral resolution achieved was experimentally determined to be approximately 19 cm^{-1} though a Lorentzian fitting of 1347 cm^{-1} peak of nitrobenzene. For comparison, Fig. 4.3B shows the spectra of these same solvents by employing parabolic amplification of the Stokes pulse, collected under the same imaging parameters as before. To obtain the broadest possible spectral coverage, the Yb-doped fiber was pumped with a power of 7 W, which leads to the Stokes bandwidth being amplified to ~70 nm for a total theoretical coverage of approximately 800 cm^{-1} as shown in Fig. 4.3B. Here, we used a pump excitation wavelength of 927 nm, to center our Raman transition at ~1300 cm^{-1}. The spectral resolution achieved with this

large bandwidth was approximately 14 cm^{-1}, calculated by Lorentzian fitting of the 1347 cm^{-1} peak of nitrobenzene. However, pumping the gain fiber with high power does not come without its limitations. As can be seen, pumping beyond the fiber's gain bandwidth begins to introduce higher order nonlinear chirp [55,62,63], which distorts the SRS spectra, particularly at lower wavenumbers compared to the spontaneous Raman spectra shown in Fig. 4.4B. We note that this might be the reason for the lower than expected spectral resolution. Nonetheless, this improvement in spectral resolution provides the ability to resolve many closely spaced Raman peaks such as the 1177 and 1192 cm^{-1} peaks from benzonitrile. Thus, careful balance of bandwidth and linearity in spectral resolution should be considered when optimizing for a given experiment. Therefore, operating the parabolic fiber amplifier within the gain bandwidth limit should produce the most optimum experimental condition for SRS microscopy.

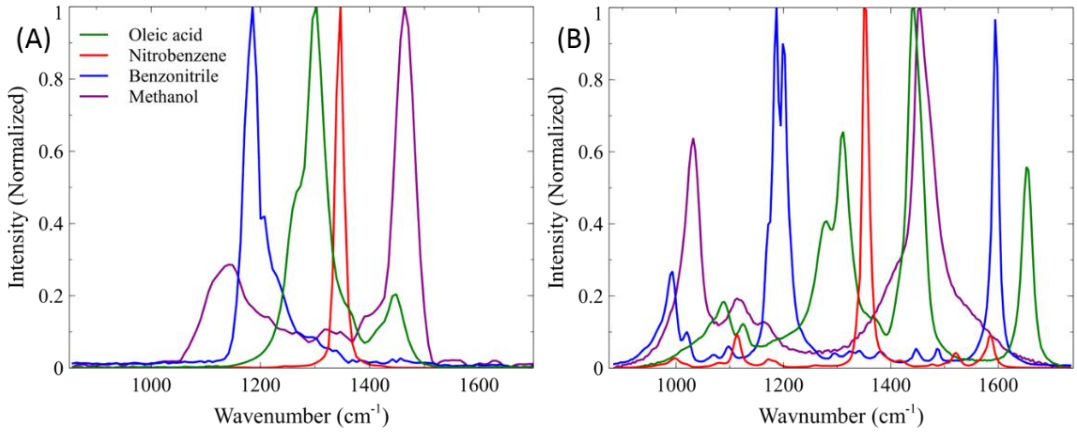

Figure 4.3 (A) SRS spectra of organic solvents using 60 cm of high dispersion glass rods and pump wavelength of 916 nm. (B) SRS spectra of organic solvents using stretcher-grating pairs and Yb-doped fiber amplifier pumped at 7 W. I_P and I_S = 40 mW.

To this end, we demonstrated that the entire fingerprint region could be examined with a minimum of two changes in pump excitation wavelength (912 and 949 nm) for optimum spectral resolution, as can be seen in Fig. 4.4A. Pumping the gain fiber with a power of 3.5 W for a bandwidth of ~50 nm (500 cm^{-1}) allows us to probe from ~1200 to 1750 cm^{-1}, while pumping at 4.5 W allows for the coverage from 700 to 1200 cm^{-1}. This total spectral coverage was again

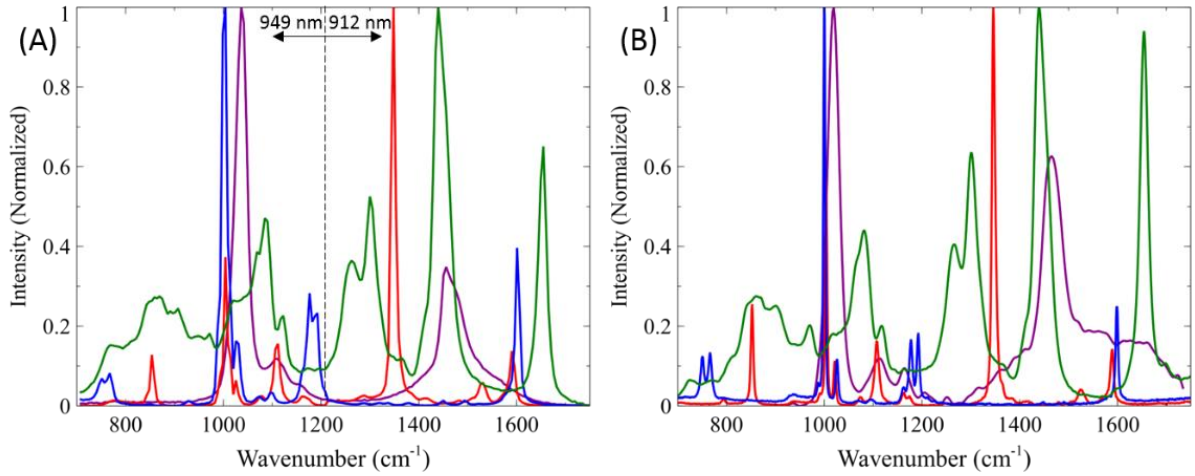

Figure 4.4 (A) Stitched SRS spectra of organic solvents covering the entire fingerprint region using two pump wavelengths: 949 nm and 912 nm and the Yb-doped fiber amplifier pumped at 4.5 W and 3.5 W, respectively. I_P and I_S = 40 mW. (B) Spontaneous Raman spectra of organic solvents. Green: oleci acid, red: nitrobenzene, blue: benzonitrile, magenta: methanol

collected with 240 spectral points with each point acquired with a 100 μs pixel dwell time. For comparison, Fig. 4.4B shows the spontaneous Raman spectra of nitrobenzene, oleic acid, benzonitrile, and methanol by a commercial confocal Raman instrument (Renishaw InVia). It is evident that the SRS and spontaneous Raman spectra are almost identical except for the slightly better spectral resolution than that achieved by our system. The validation of this increase in spectral range is a significant advantage in convenient and rapid hsSRS imaging compared to the multiple wavelength tuning process necessary with standard synchronized femtosecond beams. We demonstrated that with our new laser system, a spectral resolution of ~10 cm^{-1} is achieved, ~2 fold better than the original SRS system.

To demonstrate the capability of the improved hsSRS imaging in biological samples, we imaged PFA fixed HEK293 cells via the traditional glass rod setup and our parabolic fiber amplifier. In most Raman studies of biological samples, the region from 2800-3050 cm^{-1} is studied due to the CH_2 stretching vibration of lipids (2850 cm^{-1}) and the CH_3 stretching vibration of proteins (2930 cm^{-1}). Because protein and lipids have distinct SRS spectra in this high wavenumber region,

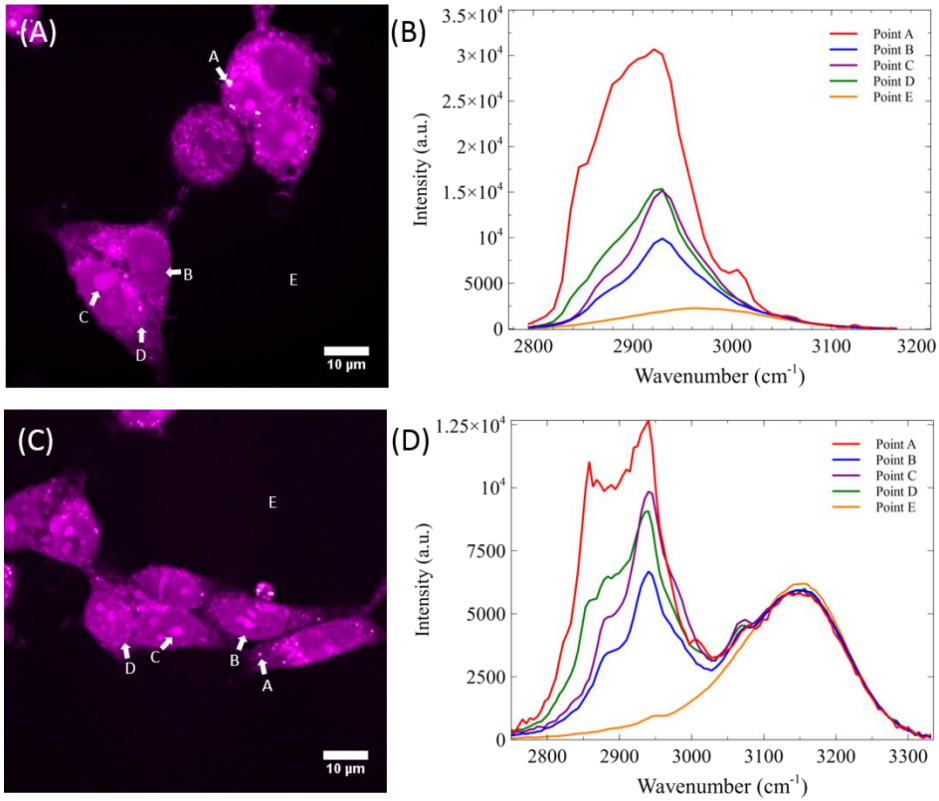

Figure 4.5 (A) SRS frame at 2930 cm^{-1} of two fixed cells using unamplified Stokes pulse. (B) SRS spectra at four individual pixels A, B, C, D, and E with negligible water signal in the area surrounding the fixed cells. (C) SRS spectra frame at 2930 cm^{-1} with amplified Stokes pulse by pumping the amplifier at 2.5 W. (D) SRS spectra of four individual pixels A, B, C, D, and E. Images are acquired at 8 us pixel dwell time. I_p and I_S = 40 mW.

visualization of cell morphology can be readily achieved due to heterogeneous distribution of biomolecules in different cellular compartments. Fig. 4.5A shows a SRS frame (512 x 512 pixels) at 2930 cm^{-1} of fixed HEK293 cells using the glass rod setup with an 800 nm pump beam. We imaged PFA fixed HEK293 cells with a total of 45 spectral frames at wavenumbers ranging from 2795 to 3165 cm^{-1} at 0.5 frame/sec with a pixel dwell time of 8 μs. At every single pixel in the frame, a spectrum can be plotted (equivalent to 360 μs per spectral acquisition). Fig. 4.5C shows HEK293 cells imaged with the parabolic amplifier pumped at 2.5 W. The Stokes bandwidth is ~ 40nm, which provides nearly doubled spectral range (510 cm^{-1}) than the original SRS system. This improvement can be readily observed when the SRS spectra of a cell's lipid droplet, nucleus, nucleolus, cytoplasm, and background/water are plotted as points A, B, C, D, and E respectively.

Because we acquired a larger range from 2745 to 3330 cm^{-1} with a total of 115 spectral images, our equivalent spectral acquisition time increased to 920 μs per spectrum. However, depending on the application, the number of spectral points can be reconfigured dynamically for faster imaging speed, but it is beyond the scope of this manuscript. In Fig. 4.5B, we can see that although the spectra of lipid droplet and the nucleolus are distinct from each other, the subtler differences between the nucleolus and cytoplasm are harder to discern. However, with the increased resolution in Fig. 4.5D, we are better suited to resolve not only the fine spectral features of lipid droplets, but also those of the nucleolus and the cytoplasm. This enhanced capability should prove useful in monitoring cellular processes such as cell division, cell differentiation and apoptosis, which

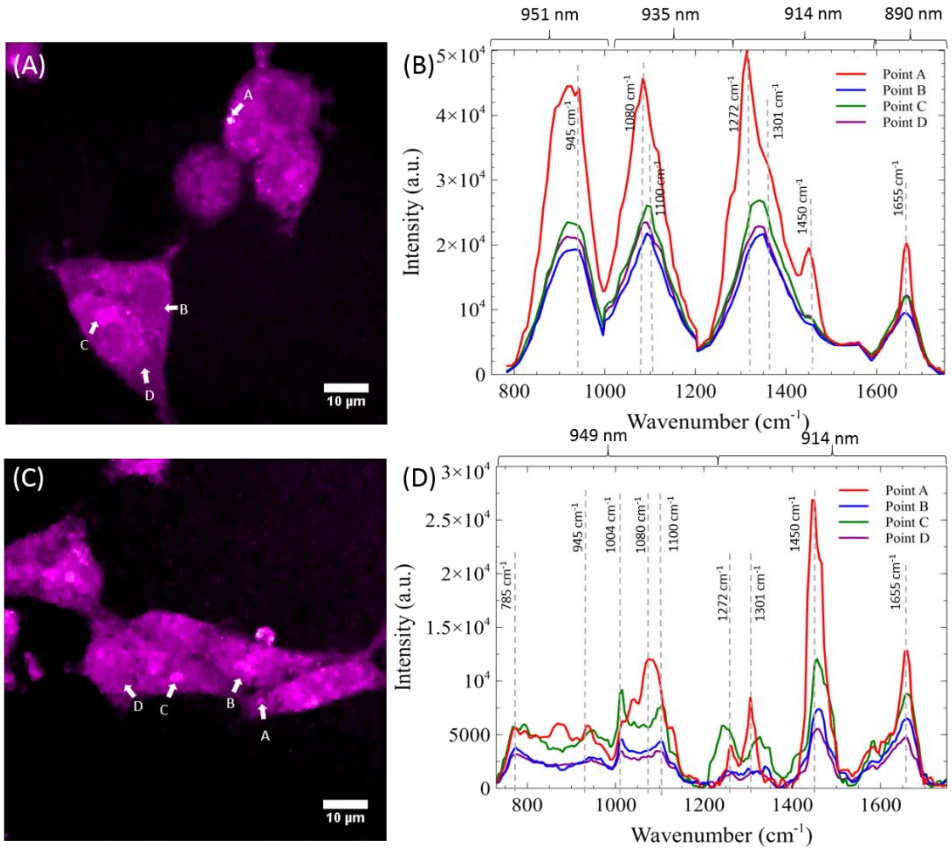

Figure 4.6 (A) SRS frame at 1090 cm^{-1} of two fixed cells using unamplified Stokes pulse. (B) SRS spectra at four individual pixels A, B, C, and D. (C) SRS frame at 1090 cm^{-1} with amplified Stokes pulse by pimping the amplifier at 4.5 W. (D) SRS spectra of four individual pixels A, B, C, and D. Images are acquired at 8 us pixel dwell time.

involve the redistribution of lipids, proteins, and nucleic acids [64,65]. Additionally, with this improved bandwidth, we start to see the detectable signal from water, which can be very useful for studying the intracellular hydrodynamics in single cells [66,67].

To further validate the benefits of employing parabolic fiber amplifier for hsSRS imaging, we demonstrated hsSRS imaging of mammalian cells in the fingerprint region from 750-1700 cm^{-1}. To cover the spectral region spanning 750 to 1700 cm^{-1}, it is necessary to scan through four different wavelengths (890, 914, 935, and 951 nm) and concatenate the resulting hyperspectral data using the original laser system. As mentioned before, having to tune the laser wavelength takes several seconds and this proves inconvenient when having to tune to four different excitation wavelengths. To cover the full fingerprint region, we acquire 135 spectral images. Fig. 4.6A shows a SRS frame at 1090 cm^{-1} using the glass rod setup, which shows lower signal compared to the SRS image in the high wavenumber region. To produce a SRS spectrum covering the region from 750 to 1700 cm^{-1}, the hyperspectral information generated by the pixels labeled A, B, C, and D were stitched together and shown in Fig. 4.6B. As before, pixels A, B, C, and D represent the spectra of a lipid droplet, nucleus, nucleolus, and cytoplasm, respectively. We used pump excitation wavelengths of 890, 914, 935, and 951 nm to probe the regions spanning 1550 to 1700 cm^{-1}, 1200 to 1550 cm^{-1}, 955 to 1200 cm^{-1}, and 750 to 955 cm^{-1} respectively. The SRS spectral data from the few respective cellular features are shown in Fig. 4.6A and B. The spectrum of the lipid droplet exhibits similar features to that of oleic acid as can be seen in in the region of 1200 to 1500 cm^{-1} in Fig. 4.6A. This is further corroborated with the Raman transition at 1655 cm^{-1} that originates from the C=C vibrations of unsaturated lipids, which overlaps with the broader Amide I band of proteins located in the nucleus and cytoplasm (points B and C). Unfortunately, the distinction between these points is not very apparent due to the low spectral resolution afforded in

this SRS configuration. In comparison, the increased bandwidth enabled by the parabolic fiber amplifier allows us to reduce the hyperspectral imaging to just two regions: 1700 – 1300 cm^{-1} and 1300 – 700 cm^{-1}. We acquired these two regions by tuning the pump excitation wavelength to 912 nm for the upper region of the fingerprint region and 949 nm for the lower part (Fig. 4.6D), with a total of 195 spectral images. SRS image at 1090 cm^{-1} with the parabolic amplifier is shown in Fig. 4.6C. To compensate for the signal loss due to long Stokes pulses, we increase the Stokes power from 40 mW to 90 mW, which is still below typical values used for SRS imaging within the cell's fingerprint region[18,22,28,68,69]. The SRS spectral data from points A, B, C, and D in Fig. 4.6C are shown in Fig. 4.6D. With the higher spectral resolution, the lipid droplet signal more closely resembles that of oleic acid (Fig. 4.3B). In addition, peaks originating from the nucleus and cytoplasm become more distinct and separable. These include the peak at 1004 cm^{-1} which originates from the ring-breathing mode of phenylalanine in proteins[68], the 1084 cm^{-1} peak from skeletal C-C vibrations, and the 1100 cm^{-1} peak of nucleic acids[70]. In addition, the small and sharp signal at 785 cm^{-1} originating from the symmetric phosphodiester stretch of nucleic acids further differentiates nucleus from the broad peak from lipids and proteins. These rich spectra features demonstrate that potential of parabolic amplification for broadband spectroscopic imaging across the fingerprint region.

To further demonstrate the use of broadband hsSRS in biomedical imaging, we applied our instrument to study amyloid plaques in human brains with Alzheimer's Disease. Alzheimer's disease (AD) is currently one of the most common causes of dementia and many resources are spent to improve early detection as well as mechanistic understanding of the disease. Raman spectroscopy and CARS has previously been implemented to study biochemical composition of AD plaques including Aβ peptide aggregates, fibrils, and associated lipids to characterize the effect

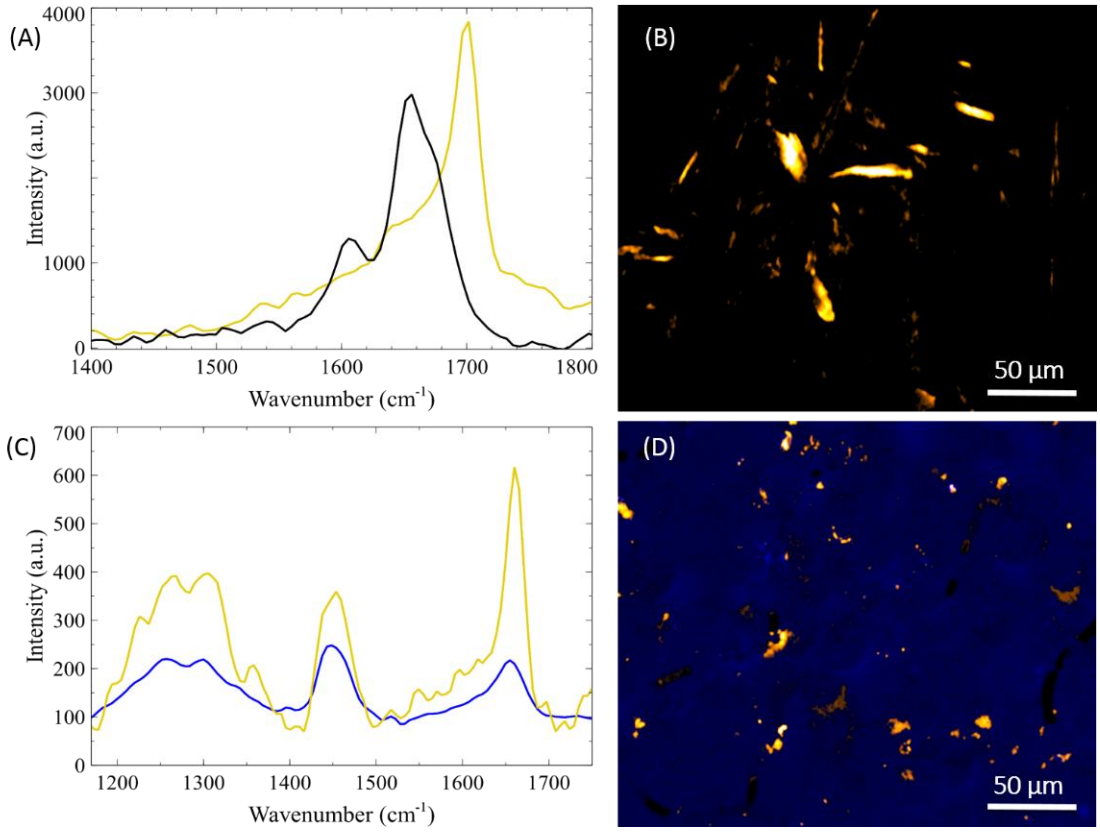

Figure 4.7 (A) SRS spectra of dissolved insulin (black) and insulin fibrils (gold). (B) Hyperspectral imaging frame at 1673 cm^{-1} of insulin fibrils. (C) SRS spectra of cortex uninvolved with plaque (blue) and Aβ fibrils (gold), one of the main components of AD induced plaques. (D) Spectrally separated uninvolved tissue and plaques through a non-negative least squares algorithm. The areas of Aβ are highlighted (gold) in the background of the brain cortex (blue).

of Alzheimer's disease on human brain tissue[71,72]. However, the low acquisition speed (50 ms/pixel) of spontaneous Raman spectroscopy and CARS (20 s/image) can be prohibitive when studying large pieces of tissue in clinical setting. Here, we exploit the benefit of broadband hsSRS over spontaneous Raman or CARS for fast, hyperspectral imaging (8 µs/pixel).

We first performed calibration studies on spectroscopic properties of insulin and insulin fibrils as a control for beta-sheets prevalent in fibril formation. Examination of the spectrum of formed fibrils showed the presence of a sharp peak around 1670 cm^{-1} (Fig. 4.7A). Using the β-sheet signatures at 1670 cm^{-1}, we were able to visualize insulin fibrils as seen in Fig. 4.7B. We then

proceeded to perform hsSRS imaging on a section of a superior temporal gyrus collected postmortem from a donor patient with clinically confirmed AD. Obtaining hyperspectral data for AD plaques, we were able to measure the fingerprint region of tissue and plaques. With the spectral information, the chemical composition can be extracted by employing a non-negative least squares algorithm along with the basis spectra for the individual components. Therefore, running our hsSRS imaging provides detailed chemical mapping between the uninvolved tissue and plaques, where we have determined the presence of β-sheet formation corresponding to AD plaques and neurofibrillary tangles.

Lastly, we note that although we significantly increased our hsSRS bandwidth over the previous configuration, the overall detection sensitivity decreased. This is due to a mismatch of the bandwidths which results in wasted spectral power density when matching a vibrational frequency via the spectral focusing approach. In addition, the longer pulse duration used also decreases pulse peak power with resulting lower sensitivity. However, depending on the application, if large

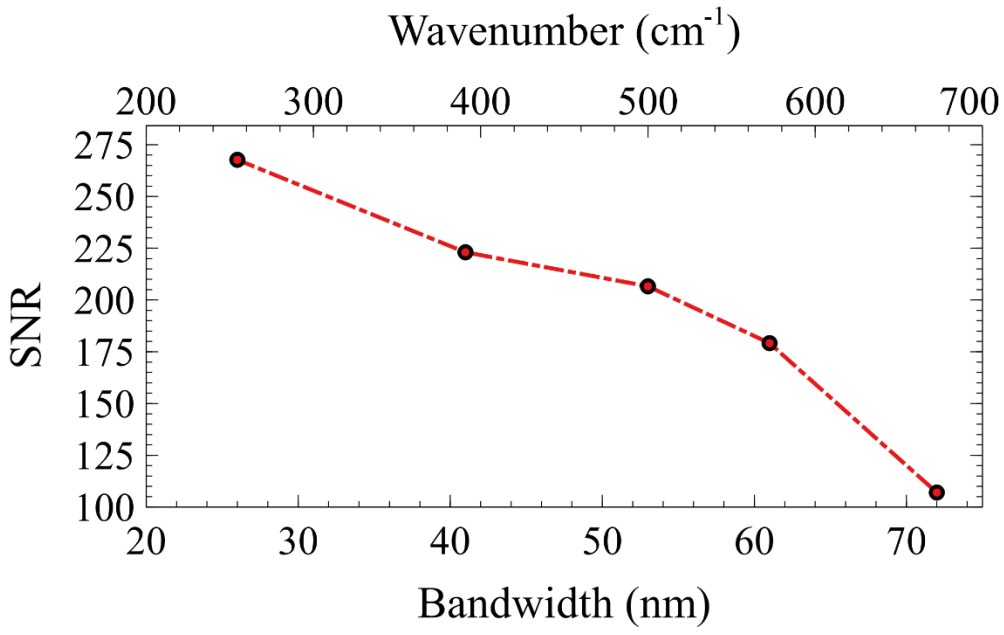

Figure 4.8 Sensitivity of SRS based on parabolic pulse amplification. Images are acquired at 4 μs pixel dwell time. I_P and I_S = 15 mW.

bandwidths are not required, the spectral tunability of the parabolic amplifier allows us to produce a gain in signal by reducing the Stokes bandwidth. Here we demonstrate that the sensitivity of hsSRS imaging depends on the bandwidth of the amplified output Stokes beam. In addition to matching the chirp rates between the pump and Stokes beam, theory predicts that optimal SRS signal will be achieved when the bandwidths of both beams are approximately equal[36]. Because our tunable pump bandwidth is ~150 cm^{-1}, we expect to see highest sensitivity as the amplified Stokes bandwidth approaches the pump's bandwidth. As seen in Fig. 4.8, the SNR decreases linearly with increasing Stokes bandwidth. Therefore, an approximate enhancement in SNR of 2.5-fold can be achieved when the bandwidths are comparable instead of maximizing the Stokes bandwidth. The nonlinear behavior observed is due to higher order dispersion when the bandwidth is very large. Nonetheless, the decrease in sensitivity with large spectral bandwidth can be partly compensated with higher optical power due to lower photodamage from longer Stokes pulse duration. Therefore, the laser bandwidth for a particular imaging application should be chosen based on the spectral bandwidth and sensitivity required.

4.4 CONCLUSION

The employment of parabolic pulse amplification provides a viable technique for increasing the bandwidth of the widely used Insight DS+ laser system for hsSRS spectral coverage to a maximum of 3-fold. This technique could be useful for the spectroscopic imaging of biological cells and tissues. We showed that with spectral broadening, hsSRS imaging could cover up to ~680 cm^{-1} without the need to change wavelengths. The entire fingerprint region can be covered with two separate scans at two different pump wavelengths. In addition to increased spectral coverage, we demonstrate an improvement in spectral resolution compared to traditional spectral-focusing hsSRS setups. The resolution is currently limited to ~10 cm^{-1}, close to the natural linewidth of the

Raman peak measured. It can be further improved by incorporating prism pairs or pulse shapers to correct the higher order chirp on the amplified Stokes beam. We demonstrated fast hsSRS imaging in the fingerprint region with the parabolic amplifier which offers much richer spectral features than our original SRS system. At the current stage, our data acquisition speed is mostly limited by the delay line stage movement, scanning mirrors, and software setup for a minimum pixel dwell time of 4 us. Even with an 8 us pixel dwell time that was used for imaging, the equivalent acquisition time per spectra in the fingerprint region is 1.6 ms/spectra, which enables acquisitions speeds faster than references 40 and 46, but comparable to broadband CARS imaging, which has achieved spectral acquisition time of 3.5 ms with a spectral coverage of ~ 425 – 2,000 cm^{-1}.[12] However, we note that quantitative spectral measurement of CARS requires phase-retrieval, and therefore it is necessary to acquire the full spectrum at high spectral resolution. In contrast, because hyperspectral SRS does not have the non-resonant background problem and the signal is strictly linearly proportional to concentration, it is not necessary to sample the entire spectrum. In fact, discrete sampling at selected wavenumbers via feature selection is more effective in quantitative analysis of a multicomponent system [73,74]. This has been illustrated in SRS imaging of nucleic acids using only three wavenumbers in the C-H region [16]. In our spectral focusing SRS configuration, discrete sampling can be readily achieved by programming delay stage positions to sequentially perform SRS imaging at predetermined wavenumbers. This will significantly speed up SRS imaging and is a unique advantage over quantitative CARS imaging. We anticipate broad biomedical imaging applications of our proposed platform. Label-free chemical mapping of individual cells by hsSRS microscopy opens new opportunities of quantitative chemical imaging of metabolites and small molecule drugs in cells, tissues, and animals. Future studies will focus on

improving spectral resolution, removing higher order chirp, improving sensitivity, and applying hsSRS imaging via parabolic pulse amplification to study lipid metabolism and tissue diagnosis.

4.5 REFERENCES

(1) Stender, A. S.; Marchuk, K.; Liu, C.; Sander, S.; Meyer, M. W.; Smith, E. A.; Neupane, B.; Wang, G.; Li, J.; Cheng, J.-X.; Huang, B.; Fang, N. Single Cell Optical Imaging and Spectroscopy. *Chem. Rev.* **2013**, *113* (4), 2469–2527. https://doi.org/10.1021/cr300336e.

(2) Chan, J. W.; Taylor, D. S.; Zwerdling, T.; Lane, S. M.; Ihara, K.; Huser, T. Micro-Raman Spectroscopy Detects Individual Neoplastic and Normal Hematopoietic Cells. *Biophys. J.* **2006**, *90* (2), 648–656. https://doi.org/10.1529/biophysj.105.066761.

(3) Manen, H.-J. van; Kraan, Y. M.; Roos, D.; Otto, C. Single-Cell Raman and Fluorescence Microscopy Reveal the Association of Lipid Bodies with Phagosomes in Leukocytes. *Proc. Natl. Acad. Sci. U.S.A* **2005**, *102* (29), 10159–10164. https://doi.org/10.1073/pnas.0502746102.

(4) Baena, J. R.; Lendl, B. Raman Spectroscopy in Chemical Bioanalysis. *Curr. Opin. Chem. Biol.* **2004**, *8* (5), 534–539. https://doi.org/10.1016/j.cbpa.2004.08.014.

(5) Evans, C. L.; Xie, X. S. Coherent Anti-Stokes Raman Scattering Microscopy: Chemical Imaging for Biology and Medicine. *Annu. Rev. Anal. Chem.* **2008**, *1* (1), 883–909. https://doi.org/10.1146/annurev.anchem.1.031207.112754.

(6) Zumbusch, A.; Holtom, G. R.; Xie, X. S. Three-Dimensional Vibrational Imaging by Coherent Anti-Stokes Raman Scattering. *Phys. Rev. Lett.* **1999**, *82* (20), 4142–4145. https://doi.org/10.1103/PhysRevLett.82.4142.

(7) Cheng, J.-X.; Xie, X. S. Coherent Anti-Stokes Raman Scattering Microscopy: Instrumentation, Theory, and Applications. *J. Phys. Chem. B* **2004**, *108* (3), 827–840. https://doi.org/10.1021/jp035693v.

(8) Camp, C. H.; Lee, Y. J.; Cicerone, M. T. Quantitative, Comparable Coherent Anti-Stokes Raman Scattering (CARS) Spectroscopy: Correcting Errors in Phase Retrieval. *J. Raman Spectrosc.* **2016**, *47* (4), 408–415. https://doi.org/10.1002/jrs.4824.

(9) Day, J. P. R.; Domke, K. F.; Rago, G.; Kano, H.; Hamaguchi, H.; Vartiainen, E. M.; Bonn, M. Quantitative Coherent Anti-Stokes Raman Scattering (CARS) Microscopy. *J. Phys. Chem. B* **2011**, *115* (24), 7713–7725. https://doi.org/10.1021/jp200606e.

(10) Cicerone, M. T.; Aamer, K. A.; Lee, Y. J.; Vartiainen, E. Maximum Entropy and Time-Domain Kramers–Kronig Phase Retrieval Approaches Are Functionally Equivalent for CARS Microspectroscopy. *J. Raman Spectrosc.* **2012**, *43* (5), 637–643. https://doi.org/10.1002/jrs.3169.

(11) Vartiainen, E. M.; Rinia, H. A.; Müller, M.; Bonn, M. Direct Extraction of Raman Line-Shapes from Congested CARS Spectra. *Opt. Express* **2006**, *14* (8), 3622–3630. https://doi.org/10.1364/OE.14.003622.

(12) Camp Jr, C. H.; Lee, Y. J.; Heddleston, J. M.; Hartshorn, C. M.; Walker, A. R. H.; Rich, J. N.; Lathia, J. D.; Cicerone, M. T. High-Speed Coherent Raman Fingerprint Imaging of Biological Tissues. *Nat. Photonics* **2014**, *8* (8), 627–634. https://doi.org/10.1038/nphoton.2014.145.

(13) Fu, D. Quantitative Chemical Imaging with Stimulated Raman Scattering Microscopy. *Curr. Opin. Chem. Biol.* **2017**, *39*, 24–31. https://doi.org/10.1016/j.cbpa.2017.05.002.

(14) Cheng, J.-X.; Xie, X. S. Vibrational Spectroscopic Imaging of Living Systems: An Emerging Platform for Biology and Medicine. *Science* **2015**, *350* (6264), aaa8870. https://doi.org/10.1126/science.aaa8870.

(15) Freudiger, C. W.; Min, W.; Saar, B. G.; Lu, S.; Holtom, G. R.; He, C.; Tsai, J. C.; Kang, J. X.; Xie, X. S. Label-Free Biomedical Imaging with High Sensitivity by Stimulated Raman Scattering Microscopy. *Science* **2008**, *322* (5909), 1857–1861. https://doi.org/10.1126/science.1165758.

(16) Lu, F.-K.; Basu, S.; Igras, V.; Hoang, M. P.; Ji, M.; Fu, D.; Holtom, G. R.; Neel, V. A.; Freudiger, C. W.; Fisher, D. E.; Xie, X. S. Label-Free DNA Imaging in Vivo with Stimulated Raman Scattering Microscopy. *PNAS* **2015**, *112* (37), 11624–11629. https://doi.org/10.1073/pnas.1515121112.

(17) Camp Jr, C. H.; Cicerone, M. T. Chemically Sensitive Bioimaging with Coherent Raman Scattering. *Nat Photon* **2015**, *9* (5), 295–305. https://doi.org/10.1038/nphoton.2015.60.

(18) Ji, M.; Orringer, D. A.; Freudiger, C. W.; Ramkissoon, S.; Liu, X.; Lau, D.; Golby, A. J.; Norton, I.; Hayashi, M.; Agar, N. Y. R.; Young, G. S.; Spino, C.; Santagata, S.; Camelo-Piragua, S.; Ligon, K. L.; Sagher, O.; Xie, X. S. Rapid, Label-Free Detection of Brain Tumors with Stimulated Raman Scattering Microscopy. *Science Translational Medicine* **2013**, *5* (201), 201ra119-201ra119. https://doi.org/10.1126/scitranslmed.3005954.

(19) Cheng, J.-X.; Xie, X. S. *Coherent Raman Scattering Microscopy*; CRC Press: Boca Raton, 2017.

(20) J. Tipping, W.; Lee, M.; Serrels, A.; G. Brunton, V.; N. Hulme, A. Stimulated Raman Scattering Microscopy: An Emerging Tool for Drug Discovery. *Chemical Society Reviews* **2016**, *45* (8), 2075–2089. https://doi.org/10.1039/C5CS00693G.

(21) Min, W.; Freudiger, C. W.; Lu, S.; Xie, X. S. Coherent Nonlinear Optical Imaging: Beyond Fluorescence Microscopy. *Annual Review of Physical Chemistry* **2011**, *62* (1), 507–530. https://doi.org/10.1146/annurev.physchem.012809.103512.

(22) Orringer, D. A.; Pandian, B.; Niknafs, Y. S.; Hollon, T. C.; Boyle, J.; Lewis, S.; Garrard, M.; Hervey-Jumper, S. L.; Garton, H. J. L.; Maher, C. O.; Heth, J. A.; Sagher, O.; Wilkinson, D. A.; Snuderl, M.; Venneti, S.; Ramkissoon, S. H.; McFadden, K. A.; Fisher-Hubbard, A.; Lieberman, A. P.; Johnson, T. D.; Xie, X. S.; Trautman, J. K.; Freudiger, C. W.; Camelo-Piragua, S. Rapid Intraoperative Histology of Unprocessed Surgical Specimens via Fibre-Laser-Based Stimulated Raman Scattering Microscopy. *Nat. Biomed. Eng.* **2017**, *1* (2), 0027. https://doi.org/10.1038/s41551-016-0027.

(23) Ji, M.; Lewis, S.; Camelo-Piragua, S.; Ramkissoon, S. H.; Snuderl, M.; Venneti, S.; Fisher-Hubbard, A.; Garrard, M.; Fu, D.; Wang, A. C.; Heth, J. A.; Maher, C. O.; Sanai, N.; Johnson, T. D.; Freudiger, C. W.; Sagher, O.; Xie, X. S.; Orringer, D. A. Detection of Human Brain Tumor Infiltration with Quantitative Stimulated Raman Scattering Microscopy. *Sci. Transl. Med.* **2015**, *7* (309), 309ra163-309ra163. https://doi.org/10.1126/scitranslmed.aab0195.

(24) Lu, F.-K.; Calligaris, D.; Olubiyi, O. I.; Norton, I.; Yang, W.; Santagata, S.; Xie, X. S.; Golby, A. J.; Agar, N. Y. R. Label-Free Neurosurgical Pathology with Stimulated Raman Imaging. *Cancer Res.* **2016**, *76* (12), 3451–3462. https://doi.org/10.1158/0008-5472.CAN-16-0270.

(25) Li, J.; Condello, S.; Thomes-Pepin, J.; Ma, X.; Xia, Y.; Hurley, T. D.; Matei, D.; Cheng, J.-X. Lipid Desaturation Is a Metabolic Marker and Therapeutic Target of Ovarian Cancer Stem Cells. *Cell Stem Cell* **2017**, *20* (3), 303-314.e5. https://doi.org/10.1016/j.stem.2016.11.004.

(26) Yue, S.; Cheng, J.-X. Deciphering Single Cell Metabolism by Coherent Raman Scattering Microscopy. *Curr. Opin. Chem. Biol.* **2016**, *33*, 46–57. https://doi.org/10.1016/j.cbpa.2016.05.016.

(27) Fu, D.; Zhou, J.; Zhu, W. S.; Manley, P. W.; Wang, Y. K.; Hood, T.; Wylie, A.; Xie, X. S. Imaging the Intracellular Distribution of Tyrosine Kinase Inhibitors in Living Cells with Quantitative Hyperspectral Stimulated Raman Scattering. *Nat Chem* **2014**, *6* (7), 614–622. https://doi.org/10.1038/nchem.1961.

(28) Wei, L.; Hu, F.; Shen, Y.; Chen, Z.; Yu, Y.; Lin, C.-C.; Wang, M. C.; Min, W. Live-Cell Imaging of Alkyne-Tagged Small Biomolecules by Stimulated Raman Scattering. *Nat. Methods* **2014**, *11* (4), 410–412. https://doi.org/10.1038/nmeth.2878.

(29) Hu, F.; Chen, Z.; Zhang, L.; Shen, Y.; Wei, L.; Min, W. Vibrational Imaging of Glucose Uptake Activity in Live Cells and Tissues by Stimulated Raman Scattering. *Angew. Chem. Int. Ed.* **2015**, *54* (34), 9821–9825. https://doi.org/10.1002/anie.201502543.

(30) Crawford, J. M.; Portmann, C.; Zhang, X.; Roeffaers, M. B. J.; Clardy, J. Small Molecule Perimeter Defense in Entomopathogenic Bacteria. *Proc. Natl. Acad. Sci. U.S.A* **2012**, *109* (27), 10821–10826. https://doi.org/10.1073/pnas.1201160109.

(31) Hong, S.; Chen, T.; Zhu, Y.; Li, A.; Huang, Y.; Chen, X. Live-Cell Stimulated Raman Scattering Imaging of Alkyne-Tagged Biomolecules. *Angew. Chem. Int. Ed.* **2014**, *53* (23), 5827–5831. https://doi.org/10.1002/anie.201400328.

(32) Fu, D.; Lu, F.-K.; Zhang, X.; Freudiger, C.; Pernik, D. R.; Holtom, G.; Xie, X. S. Quantitative Chemical Imaging with Multiplex Stimulated Raman Scattering Microscopy. *J. Am. Chem. Soc.* **2012**, *134* (8), 3623–3626. https://doi.org/10.1021/ja210081h.

(33) Zhang, D.; Wang, P.; Slipchenko, M. N.; Ben-Amotz, D.; Weiner, A. M.; Cheng, J.-X. Quantitative Vibrational Imaging by Hyperspectral Stimulated Raman Scattering Microscopy and Multivariate Curve Resolution Analysis. *Anal. Chem.* **2013**, *85* (1), 98–106. https://doi.org/10.1021/ac3019119.

(34) Ozeki, Y.; Umemura, W.; Sumimura, K.; Nishizawa, N.; Fukui, K.; Itoh, K. Stimulated Raman Hyperspectral Imaging Based on Spectral Filtering of Broadband Fiber Laser Pulses. *Opt. Lett.* **2012**, *37* (3), 431–433. https://doi.org/10.1364/OL.37.000431.

(35) Andresen, E. R.; Berto, P.; Rigneault, H. Stimulated Raman Scattering Microscopy by Spectral Focusing and Fiber-Generated Soliton as Stokes Pulse. *Opt. Lett.* **2011**, *36* (13), 2387–2389. https://doi.org/10.1364/OL.36.002387.

(36) Fu, D.; Holtom, G.; Freudiger, C.; Zhang, X.; Xie, X. S. Hyperspectral Imaging with Stimulated Raman Scattering by Chirped Femtosecond Lasers. *J. Phys. Chem. B* **2013**, *117* (16), 4634–4640. https://doi.org/10.1021/jp308938t.

(37) Suhalim, J. L.; Chung, C.-Y.; Lilledahl, M. B.; Lim, R. S.; Levi, M.; Tromberg, B. J.; Potma, E. O. Characterization of Cholesterol Crystals in Atherosclerotic Plaques Using Stimulated Raman Scattering and Second-Harmonic Generation Microscopy. *Biophys. J.* **2012**, *102* (8), 1988–1995. https://doi.org/10.1016/j.bpj.2012.03.016.

(38) Liao, C.-S.; Slipchenko, M. N.; Wang, P.; Li, J.; Lee, S.-Y.; Oglesbee, R. A.; Cheng, J.-X. Microsecond Scale Vibrational Spectroscopic Imaging by Multiplex Stimulated Raman Scattering Microscopy. *Light-Sci. Appl.* **2015**, *4* (3), e265. https://doi.org/10.1038/lsa.2015.38.

(39) Réhault, J.; Crisafi, F.; Kumar, V.; Ciardi, G.; Marangoni, M.; Cerullo, G.; Polli, D. Broadband Stimulated Raman Scattering with Fourier-Transform Detection. *Opt. Express* **2015**, *23* (19), 25235–25246. https://doi.org/10.1364/OE.23.025235.

(40) Hellerer, T.; Enejder, A. M. K.; Zumbusch, A. Spectral Focusing: High Spectral Resolution Spectroscopy with Broad-Bandwidth Laser Pulses. *Appl. Phys. Lett.* **2004**, *85* (1), 25–27. https://doi.org/10.1063/1.1768312.

(41) Beier, H. T.; Noojin, G. D.; Rockwell, B. A. Stimulated Raman Scattering Using a Single Femtosecond Oscillator with Flexibility for Imaging and Spectral Applications. *Opt. Express* **2011**, *19* (20), 18885–18892. https://doi.org/10.1364/OE.19.018885.

(42) Pegoraro, A. F.; Ridsdale, A.; Moffatt, D. J.; Jia, Y.; Pezacki, J. P.; Stolow, A. Optimally Chirped Multimodal CARS Microscopy Based on a Single Ti:Sapphire Oscillator. *Opt. Express* **2009**, *17* (4), 2984. https://doi.org/10.1364/OE.17.002984.

(43) Rocha-Mendoza, I.; Langbein, W.; Borri, P. Coherent Anti-Stokes Raman Microspectroscopy Using Spectral Focusing with Glass Dispersion. *Appl. Phys. Lett.* **2008**, *93* (20), 201103. https://doi.org/10.1063/1.3028346.

(44) Pegoraro, A. F.; Slepkov, A. D.; Ridsdale, A.; Moffatt, D. J.; Stolow, A. Hyperspectral Multimodal CARS Microscopy in the Fingerprint Region. *J. Biophotonics* **2014**, *7* (1–2), 49–58. https://doi.org/10.1002/jbio.201200171.

(45) Langbein, W.; Rocha-Mendoza, I.; Borri, P. Coherent Anti-Stokes Raman Micro-Spectroscopy Using Spectral Focusing: Theory and Experiment. *J. Raman. Spectrosc.* **2009**, *40* (7), 800–808. https://doi.org/10.1002/jrs.2264.

(46) Figueroa, B.; Chen, Y.; Berry, K.; Francis, A.; Fu, D. Label-Free Chemical Imaging of Latent Fingerprints with Stimulated Raman Scattering Microscopy. *Anal. Chem.* **2017**, *89* (8), 4468–4473. https://doi.org/10.1021/acs.analchem.6b04213.

(47) Liu, B.; Lee, H. J.; Zhang, D.; Liao, C.-S.; Ji, N.; Xia, Y.; Cheng, J.-X. Label-Free Spectroscopic Detection of Membrane Potential Using Stimulated Raman Scattering. *Appl. Phys. Lett.* **2015**, *106* (17), 173704. https://doi.org/10.1063/1.4919104.

(48) Karpf, S.; Eibl, M.; Wieser, W.; Klein, T.; Huber, R. A Time-Encoded Technique for Fibre-Based Hyperspectral Broadband Stimulated Raman Microscopy. *Nat. Commun.* **2015**, *6*, 6784. https://doi.org/10.1038/ncomms7784.

(49) Paschotta, R.; Nilsson, J.; Tropper, A. C.; Hanna, D. C. Ytterbium-Doped Fiber Amplifiers. *IEEE J. Quantum Electron.* **1997**, *33* (7), 1049–1056. https://doi.org/10.1109/3.594865.

(50) Fermann, M. E.; Kruglov, V. I.; Thomsen, B. C.; Dudley, J. M.; Harvey, J. D. Self-Similar Propagation and Amplification of Parabolic Pulses in Optical Fibers. *Phys. Rev. Lett.* **2000**, *84* (26), 6010–6013. https://doi.org/10.1103/PhysRevLett.84.6010.

(51) Kruglov, V. I.; Peacock, A. C.; Dudley, J. M.; Harvey, J. D. Self-Similar Propagation of High-Power Parabolic Pulses in Optical Fiber Amplifiers. *Opt. Lett.* **2000**, *25* (24), 1753–1755. https://doi.org/10.1364/OL.25.001753.

(52) Kruglov, V. I.; Peacock, A. C.; Harvey, J. D.; Dudley, J. M. Self-Similar Propagation of Parabolic Pulses in Normal-Dispersion Fiber Amplifiers. *Jour. Opt. Soc. Am. B* **2002**, *19* (3), 461–469. https://doi.org/10.1364/JOSAB.19.000461.

(53) Finot, C.; Dudley, J. M.; Kibler, B.; Richardson, D. J.; Millot, G. Optical Parabolic Pulse Generation and Applications. *IEEE Journal of Quantum Electronics* **2009**, *45* (11), 1482–1489. https://doi.org/10.1109/JQE.2009.2027446.

(54) Peacock, A. C.; Kruhlak, R. J.; Harvey, J. D.; Dudley, J. M. Solitary Pulse Propagation in High Gain Optical Fiber Amplifiers with Normal Group Velocity Dispersion. *Opt. Comm.* **2002**, *206* (1), 171–177. https://doi.org/10.1016/S0030-4018(02)01382-2.

(55) Soh, D. B.; Nilsson, J.; Grudinin, A. B. Efficient Femtosecond Pulse Generation Using a Parabolic Amplifier Combined with a Pulse Compressor I Stimulated Raman-Scattering Effects. *Jour. Opt. Soc. Am. B* **2006**, *23* (1), 1. https://doi.org/10.1364/JOSAB.23.000001.
(56) Soh, D. B.; Nilsson, J.; Grudinin, A. B. Efficient Femtosecond Pulse Generation Using a Parabolic Amplifier Combined with a Pulse Compressor. II. Finite Gain-Bandwidth Effect. *J. Opt. Soc. Am. B* **2006**, *23* (1), 10–19. https://doi.org/10.1364/JOSAB.23.000010.
(57) Deng, Y.; Chien, C.-Y.; Fidric, B. G.; Kafka, J. D. Generation of Sub-50 Fs Pulses from a High-Power Yb-Doped Fiber Amplifier. *Opt. Lett.* **2009**, *34* (22), 3469–3471. https://doi.org/10.1364/OL.34.003469.
(58) Limpert, J.; Schreiber, T.; Clausnitzer, T.; Zöllner, K.; Fuchs, H.-J.; Kley, E.-B.; Zellmer, H.; Tünnermann, A. High-Power Femtosecond Yb-Doped Fiber Amplifier. *Opt. Express* **2002**, *10* (14), 628. https://doi.org/10.1364/OE.10.000628.
(59) Francis, A.; Berry, K.; Chen, Y.; Figueroa, B.; Fu, D. Label-Free Pathology by Spectrally Sliced Femtosecond Stimulated Raman Scattering (SRS) Microscopy. *PLOS ONE* **2017**, *12* (5), e0178750. https://doi.org/10.1371/journal.pone.0178750.
(60) Lai, M.; Lai, S. T.; Swinger, C. Single-Grating Laser Pulse Stretcher and Compressor. *Appl. Opt., AO* **1994**, *33* (30), 6985–6987. https://doi.org/10.1364/AO.33.006985.
(61) Pessot, M.; Maine, P.; Mourou, G. 1000 Times Expansion/Compression of Optical Pulses for Chirped Pulse Amplification. *Optics Communications* **1987**, *62* (6), 419–421. https://doi.org/10.1016/0030-4018(87)90011-3.
(62) Chang, G.; Galvanauskas, A.; Winful, H. G.; Norris, T. B. Dependence of Parabolic Pulse Amplification on Stimulated Raman Scattering and Gain Bandwidth. *Opt. Lett., OL* **2004**, *29* (22), 2647–2649. https://doi.org/10.1364/OL.29.002647.
(63) Papadopoulos, D. N.; Zaouter, Y.; Hanna, M.; Druon, F.; Mottay, E.; Cormier, E.; Georges, P. Generation of 63 Fs 4.1 MW Peak Power Pulses from a Parabolic Fiber Amplifier Operated beyond the Gain Bandwidth Limit. *Opt. Lett., OL* **2007**, *32* (17), 2520–2522. https://doi.org/10.1364/OL.32.002520.
(64) Uzunbajakava, N.; Lenferink, A.; Kraan, Y.; Volokhina, E.; Vrensen, G.; Greve, J.; Otto, C. Nonresonant Confocal Raman Imaging of DNA and Protein Distribution in Apoptotic Cells. *Biophys. J.* **2003**, *84* (6), 3968–3981.
(65) Puppels, G. J.; Mul, F. F. M. de; Otto, C.; Greve, J.; Robert-Nicoud, M.; Arndt-Jovin, D. J.; Jovin, T. M. Studying Single Living Cells and Chromosomes by Confocal Raman Microspectroscopy. *Nat.* **1990**, *347* (6290), 301–303. https://doi.org/10.1038/347301a0.
(66) Potma, E. O.; Boeij, W. P. de; Haastert, P. J. M. van; Wiersma, D. A. Real-Time Visualization of Intracellular Hydrodynamics in Single Living Cells. *Proc. Natl. Acad. Sci. U.S.A* **2001**, *98* (4), 1577–1582. https://doi.org/10.1073/pnas.98.4.1577.
(67) Cheng, J.-X.; Pautot, S.; Weitz, D. A.; Xie, X. S. Ordering of Water Molecules between Phospholipid Bilayers Visualized by Coherent Anti-Stokes Raman Scattering Microscopy. *Proc. Natl. Acad. Sci. U.S.A* **2003**, *100* (17), 9826–9830. https://doi.org/10.1073/pnas.1732202100.
(68) Zhang, X.; Roeffaers, M. B. J.; Basu, S.; Daniele, J. R.; Fu, D.; Freudiger, C. W.; Holtom, G. R.; Xie, X. S. Label-Free Live Cell Imaging of Nucleic Acids Using Stimulated Raman Scattering (SRS) Microscopy. *Chemphyschem* **2012**, *13* (4), 1054–1059. https://doi.org/10.1002/cphc.201100890.
(69) Freudiger, C. W.; Min, W.; Holtom, G. R.; Xu, B.; Dantus, M.; Xie, X. S. Highly Specific Label-Free Molecular Imaging with Spectrally Tailored Excitation Stimulated Raman

Scattering (STE-SRS) Microscopy. *Nat. Photonics* **2011**, *5* (2), 103–109. https://doi.org/10.1038/nphoton.2010.294.

(70) Goodwin, D. C.; Brahms, J. Form of DNA and the Nature of Interactions with Proteins in Chromatin. *Nucleic Acids Res* **1978**, *5* (3), 835–850.

(71) Michael, R.; Lenferink, A.; Vrensen, G. F. J. M.; Gelpi, E.; Barraquer, R. I.; Otto, C. Hyperspectral Raman Imaging of Neuritic Plaques and Neurofibrillary Tangles in Brain Tissue from Alzheimer's Disease Patients. *Sci. Rep.* **2017**, *7* (1), 15603. https://doi.org/10.1038/s41598-017-16002-3.

(72) Kiskis, J.; Fink, H.; Nyberg, L.; Thyr, J.; Li, J.-Y.; Enejder, A. Plaque-Associated Lipids in Alzheimer's Diseased Brain Tissue Visualized by Nonlinear Microscopy. *Sci. Rep.* **2015**, *5*, 13489. https://doi.org/10.1038/srep13489.

(73) Yi-Zeng, L.; Yu-Long, X.; Ru-Qin, Y. Accuracy Criteria and Optimal Wavelength Selection for Multicomponent Spectrophotometric Determinations. *Anal. Chim. Acta* **1989**, *222* (1), 347–357. https://doi.org/10.1016/S0003-2670(00)81909-1.

(74) Fu, D.; Xie, X. S. Reliable Cell Segmentation Based on Spectral Phasor Analysis of Hyperspectral Stimulated Raman Scattering Imaging Data. *Anal. Chem.* **2014**, *86* (9), 4115–4119. https://doi.org/10.1021/ac500014b.

Chapter 5: Real-Time Microscale Temperature imaging by Stimulated Raman Scattering

The work presented in this chapter has been published in the following paper:

Figueroa, B., Hu, R., Rayner, S. G., Zheng, Y. & Fu, D. "Real-Time Microscale Temperature Imaging by Stimulated Raman Scattering." J. Phys. Chem. Lett. 7083–7089 (2020)

5.1 INTRODUCTION

Temperature is a fundamental parameter in determining chemical reaction rates as dictated by the Arrhenius equation. Such dependence is also essential in biological systems. In mammals, body temperature is strictly regulated to maintain cell homeostasis through a careful balance of heat generation and heat dissipation.[1,2] Aberrant temperatures can cause cell death through apoptosis and necrosis.[3] This effect has been utilized in photothermal therapy for targeted tumor ablation and in cold therapy for fat loss.[4,5] It is essential to monitor the temperature in biological cells to understand body physiology and to develop new therapeutic approaches. While temperature can be easily measured with either a contact-type thermal couple or non-contact infrared thermography, the spatial resolution has been typically limited to tens of micrometers or worse.

To image temperature distribution at micrometer resolution for intracellular temperature measurements, a wide variety of fluorescence temperature sensors including temperature-sensitive fluorescent polymers,[6] quantum dots,[7] nanodiamonds,[8] and fluorescent proteins[9] have been developed. Fluorescent thermosensors offer sub-degree temperature sensitivity and provide the dual function of imaging and temperature sensing. To improve robustness of intracellular measurements, ratiometric imaging or fluorescence lifetime imaging is employed, which overcomes the limitations of intensity-based imaging.[6,9]

A wide range of intracellular temperature gradients has been reported with various fluorescent sensors. For example, mitochondria temperature was reported to be anywhere from 1°C to 10°C warmer than the cytoplasm.[9–11] While some of these variations may reflect biological differences, others could also be attributed to measurement bias due to environmental influences on fluorescence.[12] Recent debate on the validity of fluorescence based intracellular temperature measurements further highlight the need for rigorous validation, especially with orthogonal label-free techniques for accurate temperature measurement.[13–15]

Raman spectroscopy has shown promise for temperature measurement with prior reports estimating temperature by measuring the ratio of anti-Stokes to Stokes scattering.[16] However, its sensitivity is limited to ~10°C.[17] In a related technique, Raman spectroscopy can also monitor water temperature based on changes in hydrogen bonding. The OH stretching band of water has two inversely related temperature-dependent modes: the hydrogen-bonded (HB) and non-hydrogen-bonded (NHB) modes at 3200 and 3600 cm^{-1}, respectively. As the temperature increases, the hydrogen bonding of clustered water molecules is broken, and the number of non-hydrogen-bonded water molecules increases. Temperature is linearly correlated to the ratio of these two modes.[18] This phenomenon has been previously used to determine water temperature with precision reaching 0.1°C, which is comparable to fluorescence thermometry.[18,19] However, as Raman scattering is a weak process, this technique has been limited to point measurements in systems at steady states. It is thus not suitable for temperature imaging of dynamic biological specimens.

Here, we describe the development of a stimulated Raman scattering (SRS) based thermometry technique utilizing fast ratiometric imaging of two water Raman bands for microscale temperature mapping. SRS improves the Raman scattering efficiency by more than 6 orders of magnitude

through coherent excitation. Indeed, SRS microscopy has been widely used in favor of spontaneous Raman microscopy for cellular and tissue imaging due to its superior imaging speed.[20,21] Using our previously developed broadband fiber laser[22] and a dual-channel orthogonal modulation scheme, we perform real-time ratiometric SRS imaging of the HB and NHB modes of water and map microscale temperature distribution. We demonstrate quantification of heat generation from a laser point source in aqueous and biological samples and the capability to extract the thermal conductivities of subcellular components. This advancement paves the way for real-time label-free *in vivo* imaging of microscale intracellular thermogenesis.

5.2 RESULTS AND DISCUSSION

To image two Raman bands simultaneously for ratiometry, we use a two-channel orthogonal modulation technique that was recently developed for SRS imaging with spectral focusing (Figure

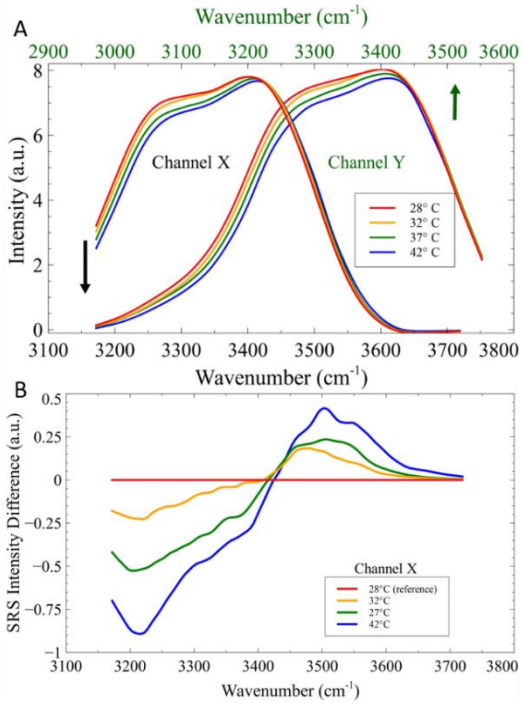

Figure 5.1 A) Simultaneous collection of 2-channel SRS spectra arising from OH stretching vibrations of liquid H2O at different temperatures. B) SRS difference spectra calculated from the spectra of channel X.

C.1).[23,24] Details of the experimental setup and detection scheme are provided in the Supplementary Information. Briefly, two orthogonally modulated Stokes pulses train are combined with the pump beam for excitation of two different Raman bands that are determined by their respective pump-Stokes time delay. The lock-in amplifier outputs in the X channel and Y channel provide two independent readings of SRS signals at these two Raman bands. The original orthogonal modulation method is highly sensitive to the optical alignment due to the requirement for precise spatial and temporal overlap of three different beams. We address this shortcoming by using two electro-optical modulators to perform orthogonal modulation, thus obviating the need for alignment of two separate Stokes beams (Figure C.1). Due to the limited bandwidth of the SRS pump and Stokes lasers (150 cm^{-1} and 60 cm^{-1}, respectively), existing SRS systems based on spectral focusing cannot reliably probe both temperature-dependent Raman bands. We use our previously developed parabolic fiber amplifier to increase spectral bandwidth of the Stokes laser to ~ 500 cm^{-1} (Figure C.2).[22] We calibrated Raman frequency using SRS imaging of urea crystals(Figure C.3). The broadband laser source allows for the simultaneous acquisition of the two temperature-dependent Raman bands.

To determine the temperature-induced spectral changes on water, SRS spectra at different temperatures were recorded by scanning the time delay between the pump and the two orthogonally modulated Stokes beams. The pump beam was tuned to 779 nm to optimize detection of the OH vibrational band with the 1050 nm Stokes beams. Figure 1A shows water SRS spectra collected from the two orthogonal SRS channels (i.e. Channel X and Channel Y from the lock-in amplifier) from 3050-3700 cm^{-1}. As shown in Figure 5.1A, the SRS intensity below the isosbestic point (~3450 cm^{-1}) decreases with a temperature rise, while the intensity above the isosbestic point slightly increases. This is due to changes in equilibrium between the HB and the NHB water

molecules. The isosbestic point is observed near 3450 cm^{-1}, comparable to previously reported values.[18,25] To show the spectral change more clearly, Raman difference spectra were calculated from Figure 5.1A by subtracting the reference spectrum at 28°C from other spectra (Figure 5.1B). It is evident that the OH stretching band of water has two modes with contrasting temperature dependencies: a negative peak at ~3220 cm^{-1} and a positive peak around 3550 cm^{-1}. Previous Raman thermometry studies monitored the ratio of 3200/3600 cm^{-1} to maximize temperature sensitivity. Our difference spectra peaks deviate slightly from previous reports. This deviation can be attributed to the limited spectral bandwidth of SRS which reshapes the NHB band towards lower wavenumbers and lower spectral resolution of our SRS microscope (~30 cm^{-1}). For our study, we focus on the ratio between the HB and isosbestic band because the isosbestic SRS band intensity near 3420 cm^{-1} is much higher than at 3550 cm^{-1}, which offers higher SNR in imaging.

To correlate temperature with SRS intensity ratio of $I_{3220cm-1}/I_{3420\ cm-1}$ (I_{ratio}), calibration experiments were performed under uniform temperature conditions using a temperature-controlled chamber. Absolute temperature of water was determined by a miniature thermistor placed inside the chamber. For each temperature, 10 SRS image pairs were acquired at 1 frame/sec. These images were averaged and the I_{ratio} image was determined by dividing the HB channel (~3220 cm^{-1}) by the isosbestic channel (~3420 cm^{-1}). We would like to note that although we use averaging to increase the sensitivity, the temperature at each pixel (4 μs pixel dwell time), contains sub-second temperature measurements. The averaging of 10 frames reduces noise and may average out temperature changes between frames due to accumulated heating. Figure 5.2 shows the relationship between temperature and I_{ratio}. As expected, I_{ratio} scales linearly with temperature. The standard deviation of the intensity ratio for each averaged I_{ratio} image is indicated as the error bar. Error estimates were performed at the center of the image as SRS intensity is highest at the center.

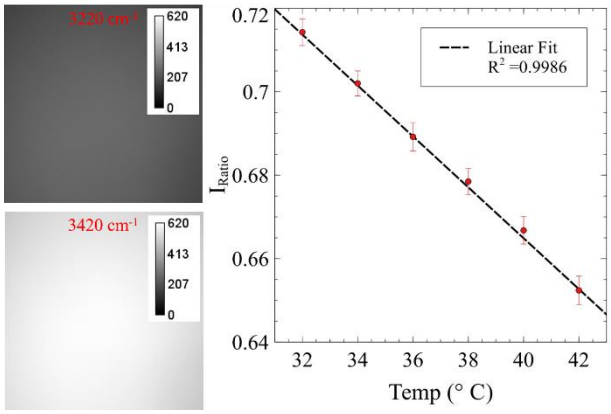

Figure 5.2 Left) SRS intensity images of the hydrogen bonded channel and isosbestic channel at 3220 and 3420 cm^{-1}, respectively. Right) Temperature calibration showing the linear relationship between temperature and SRS intensity ratio (I_{Ratio}).

This effect is caused by the chromatic aberration of the objective lens. Based on the calibration curve and measured intensity ratio error, we determine that SRS thermometry provides a temperature imaging accuracy of 0.53°C (close to the edge of the image, the error increases to 0.69°C), which is comparable to many fluorescent temperature sensors.[6,10,26–28]

Next, we apply SRS thermometry to directly quantify laser induced heating in water. Photothermally induced heating has been used increasingly as a tool for microscopic manipulation in biology, such as photothermal therapy.[29] While various studies have focused on simulating heating by absorption in the focus of an objective for the optimization of laser parameters (e.g. wavelength, irradiation intensity, penetration depth, spot size, etc),[30,31] experimental studies of microscale temperature change due to laser heating have been mostly limited to optical tweezer experiments.[32] To visualize the temperature gradient induced by a focused infrared laser beam, we coupled a continuous wave 1480 nm fiber laser diode via the side port of the inverted microscope (bypassing the galvo scan mirrors) to provide localized heating in our imaging field of view. The heating laser was focused onto the sample, producing a temperature gradient around the heating spot. The SRS image of the temperature distribution is shown in Figure 5.3A by converting I_{ratio}

into temperature using the calibration demonstrated in Figure 5.2. We observed a maximum temperature rise of ~16°C induced by 10 mW irradiation power. Time-lapse imaging shows that temperature rise happens in less than a second, below the temporal resolution of our system (Figure 5.3B). This sub-second rapid heating reaches an equilibrium of ~ 51°C at the focal point and decreases rapidly away from the focus. Figure 5.3C plots the radial temperature profile as a function of irradiation intensity. Maximal temperature increase at the laser focus depends linearly on the optical power (Figure 5.3D).

To verify these results, we used the finite element method provided within COMSOL modeling software to solve the heat transport equation with appropriate initial and boundary conditions (see Supporting Information). In contrast to previous reports where laser induced heating was modeled in a region distant from the boundaries,[33,34] the temperature gradient arising from a stationary laser spot 10 µm above the coverslip was modeled, resulting in an axially asymmetrical temperature

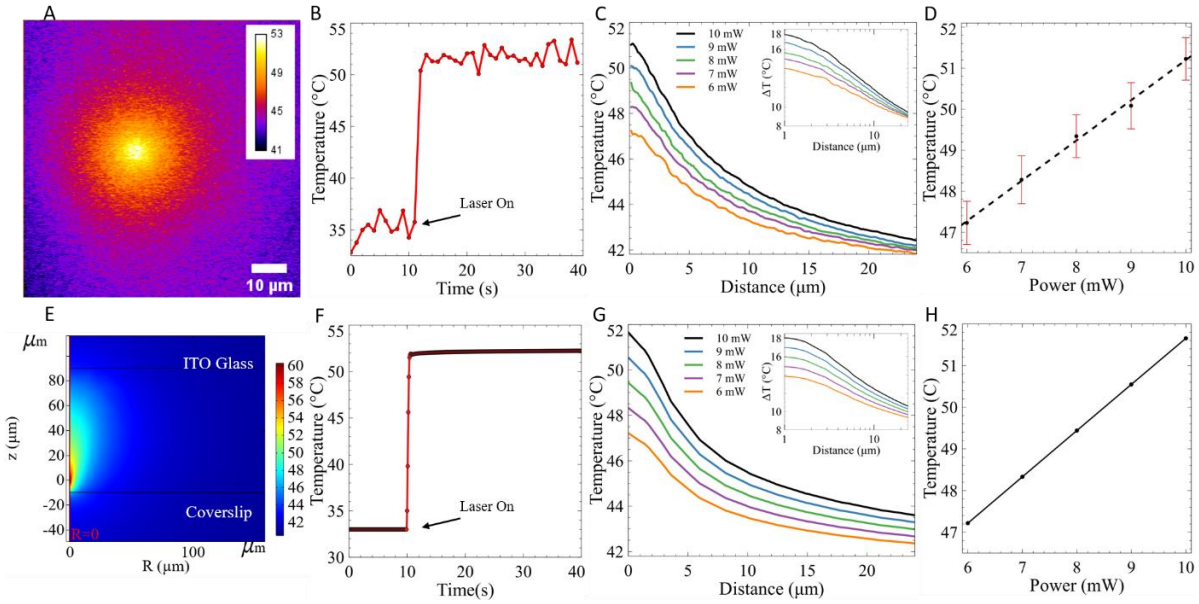

Figure 5.3 Experimental and simulated temperature distribution generated by a focused IR laser. A) Temperature mapping of laser induced heating by a 1480 nm IR laser source in water. B) Temporal profile of temperature at the center of the laser spot C) Radial profiles of temperature gradient at different IR irradiation powers (log scale plot in inset) D) Peak temperature of the localized heating source as a function of irradiation power. E) Simulation of heating source near the coverslip boundary. F-H) Simulated counterparts of B-D).

gradient arising from the coverslip boundary (Figure 5.3E). Analysis of the simulated radial thermal decay from the center of the laser spot reveals similar peak temperature profiles compared to our experimental conditions. We note that the temperature profile depends on how far the imaging plane deviates from the heating spot (Figure C.4). In our simulation (Figure 5.3G), a separation of 7 μm provides best matching of simulation to experimental results, suggesting that the axial chromatic aberration of IR heating laser and SRS lasers may give rise to lower observed temperature gradients. Other factors may also influence experimental measurements, including the size of the IR laser focus and the distance of the laser focus to the coverslip. Nevertheless, both our experiment and simulation results show that at 2-3 μm away from the heating focus, the temperature follows a logarithmic decay with the distance r away from the laser focus via the model proposed by Mao *et al.*, $\Delta T = \frac{\alpha(\lambda)*P}{2\pi k} * ln(r)$ (Figure 5.3C,G insets).[33,34] Here α is the frequency dependent absorption coefficient of water (2100 m^{-1}), P is laser power (10mW), and k is thermal conductivity of the medium. As seen in Figures 5.3B and C.2B, the slope of the model will be affected by the proximity of the heating source to the coverslip and therefore the equation needs to be modified with an additional correction factor that is a function of geometrical arrangement and laser focus property. Importantly, the agreement between simulations and experiments suggest that the heat diffusion equation holds at the micrometer scale, which is important for modeling heat diffusion inside the cell.[14]

We note that while measuring temperature increase due to an external laser source is valuable with respect to photothermal therapy, the heating due to the imaging lasers is also important to consider for many imaging applications. Indeed, photodamage in nonlinear optical microscopy is a common concern in the field due to the high optical powers often used in live cell or animal imaging.[35] Direct measurement of temperature change due to nonlinear optical microscopy is

scarce.[36,37] Using SRS thermometry, we demonstrate the ability to directly measure the temperature increase due to SRS imaging (Figure 5.3F). Specifically, the first few seconds (before the external laser is applied) see an increase of ~2°C. This temperature increase is due to the combined effect of linear absorption of the pump and Stokes beams as well as heat dissipation from the SRS process. Based on thermistor measurements, absorption of SRS excitation beams is the dominant source of heating. This temperature increase due to imaging is often insufficient to cause thermal damage but may cause physiological changes.[37,38] Therefore, SRS imaging experiments on living biological samples should limit total power to ~100 mW to avoid potential damage and incorrect interpretation of cell physiology, especially for longitudinal imaging.

Next, we measure the thermal conductivity of cellular materials using our SRS-based thermometry technique. Thermal conductivity is a key parameter in determining the temperature rise in the presence of a heat source. Within the cell, the mitochondrion is considered the "power house" and its energy production may create a heat gradient within the cell. Previous reports on the mitochondria temperature vary widely from 1°C to 10°C above the cytoplasm. However, theoretical arguments based on thermal generation and heat diffusion suggest that temperature rise of mitochondria should be a few orders of magnitude smaller.[13] One crucial element in this debate

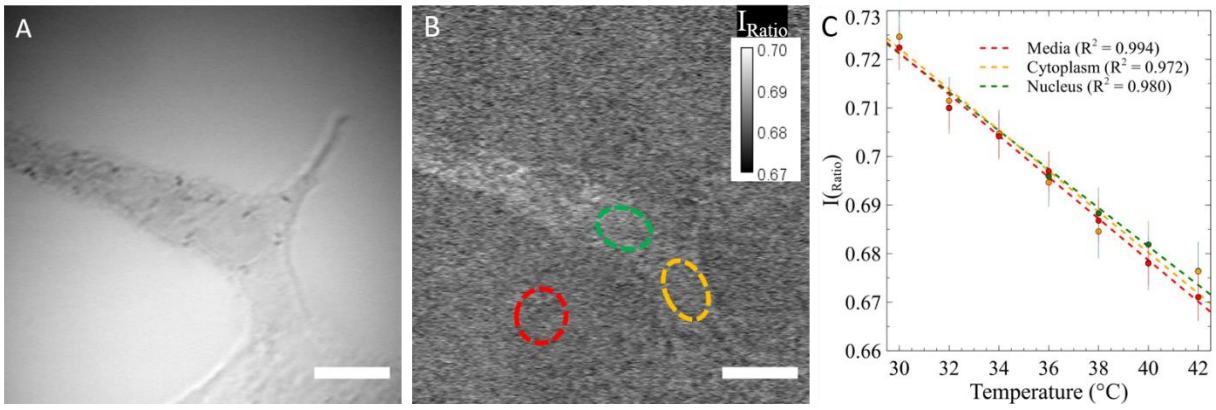

Figure 5.4 SRS Thermometry on fixed A549 cells kept at 37°C. Representative A) SRS image at 3420 cm^{-1} and B) SRS thermal map. C) Temperature calibration of intra and extracellular components. The scale bar 10 is μm.

is the thermal conductivity in the presence of a membrane. Here we use SRS thermometry to show that membrane structure does not change the thermal conductivity significantly.

We first created calibration curves by varying the extracellular temperature of fixed A549 cells using the temperature-controlled chamber and imaged with ratiometric SRS. It is important to note that cellular materials have other components (lipids, protein, and salts etc.) that may influence the water SRS spectrum (Figure C.5). Therefore, the calibration of cell temperature needs to account for these components. Figure 5.4A displays a representative SRS image at 3420 cm^{-1} of a fixed cell with its I_{ratio} image at 37°C shown in Figure 5.4B. Because there is no heat source, we assume that the temperature throughout the cell is uniform. Figure 5.4C shows the relationship between temperature and I_{ratio} for different cellular compartments at temperatures between 30-42°C. Although there are slight spectral differences between the cellular components, we observe that the calibration slope difference between intracellular and extracellular material is relatively small at <0.0017, suggesting that cellular materials and their compositional variation have little influence on the calibration curve. Due to the nonuniformity of the sample, the accuracy of temperature calibration is lower compared to bulk water. From the standard deviation of the I_{Ratio}, we estimated that accuracy to be ~ 1.2°C.

Next, we performed laser heating inside the fixed cell to extract thermal conductivity values via the amended model of Mao *et al*.[33] The temperature gradient can be estimated by $\Delta T = C\frac{\alpha(\lambda)*P}{2\pi k} * ln(r)$, where *C* is the correction factor that accounts for distance to the heat sink, aberration, and other geometric factors. For a given geometry, ΔT is inversely proportional to the thermal conductivity *k*. We can obtain a proportionality constant from the slope which will enable the extraction of k within cells based on the known value of water. By moving the sample relative to the IR laser focus, we determined the logarithmic slope of the radial temperature decay profile for

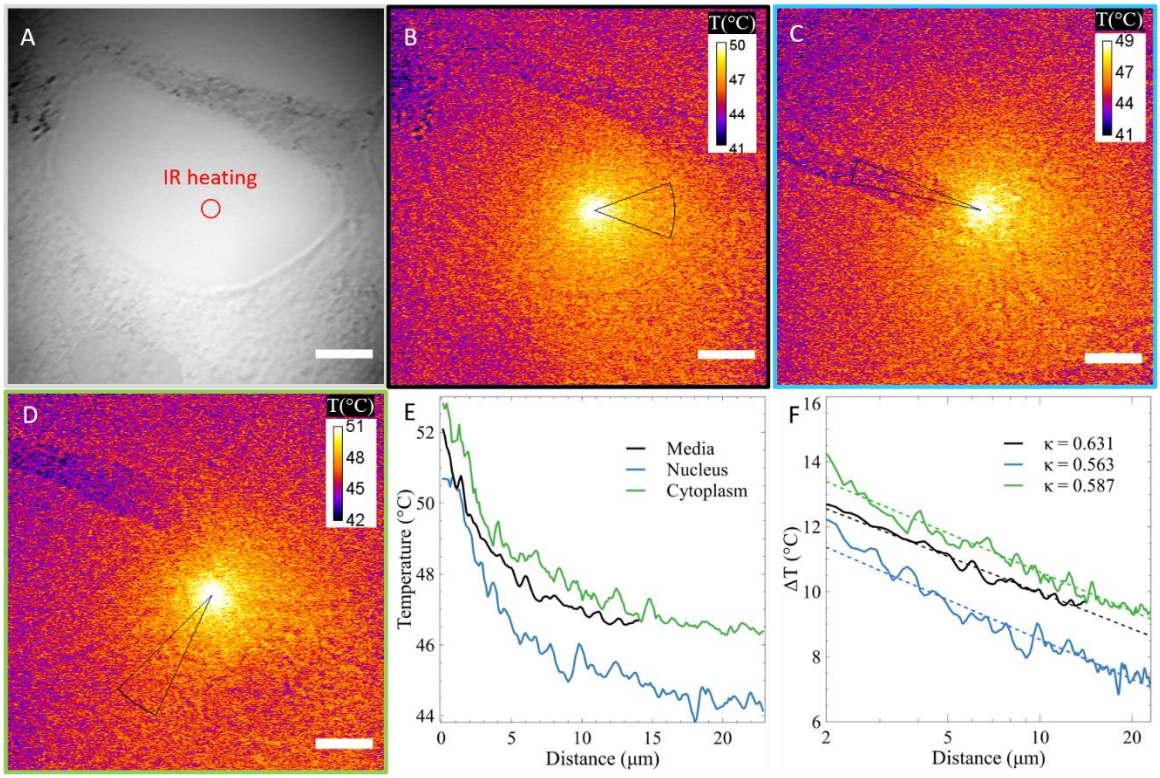

Figure 5.5 IR heating on extracellular and intracellular material of a fixed A549 cell. A) 3420 cm^{-1} Raman transition showing the heating location on the media with boxes indicating representative regions of interest. SRS temperature image (average of 10 frames) of IR heating on the B) media, C) nucleus, and D) cytoplasm with their respective ROIs for radial profiling. E) Thermal decay curves from each ROI. D) Log scale plots with slopes converted to thermal conductivities for each component. The scale bar is 10 μm.

cytoplasm, nucleus, and extracellular region. Only the range of distance r where it satisfies the logarithmic linear model and does not cross any cellular boundaries were used for fitting (cones in Fig 5.5). Using the known value of k for water (k_{water} ~ 0.631 $W \cdot m^{-1} \cdot K^{-1}$.),[39] we calculated the k values of subcellular regions and found that both the nucleus ($k_{nucleus}$ ~ 0.563 $W \cdot m^{-1} \cdot K^{-1}$) and the cytoplasm ($k_{cytoplasm}$ ~ 0.587 $W \cdot m^{-1} \cdot K^{-1}$) exhibit lower thermal conductivity than water. This agrees with previously reported values showing lower thermal conductivities for intracellular components compared to aqueous solutions.[40] However, the difference is relatively small and would not influence the temperature significantly in the presence of intracellular thermogenesis.

Lastly, we investigated intracellular thermogenesis of mitochondria using COMSOL simulation based on the thermal conductivity measured. We simulated heating distribution from a single mitochondrion within a living cell set at 37°C (Figure 5.6A). Even when assuming that the average heat generation of the cell (~100 pW/cell)[41,42] originates from a single mitochondrial (L = 500 nm), a temperature change of only $\Delta T \sim 0.0005$°C is expected. This miniscule change is far below the sensitivity limits of current thermography techniques. It also confirms previous theoretical argument by Baffou *et.al.* that intracellular temperature gradient due to mitochondria heating is orders of magnitude than 1°C.[13] When applying our ratiometric SRS imaging to live cells, we observed that unlike fixed cells, live cells exhibit higher ratio than the extracellular media (Figure

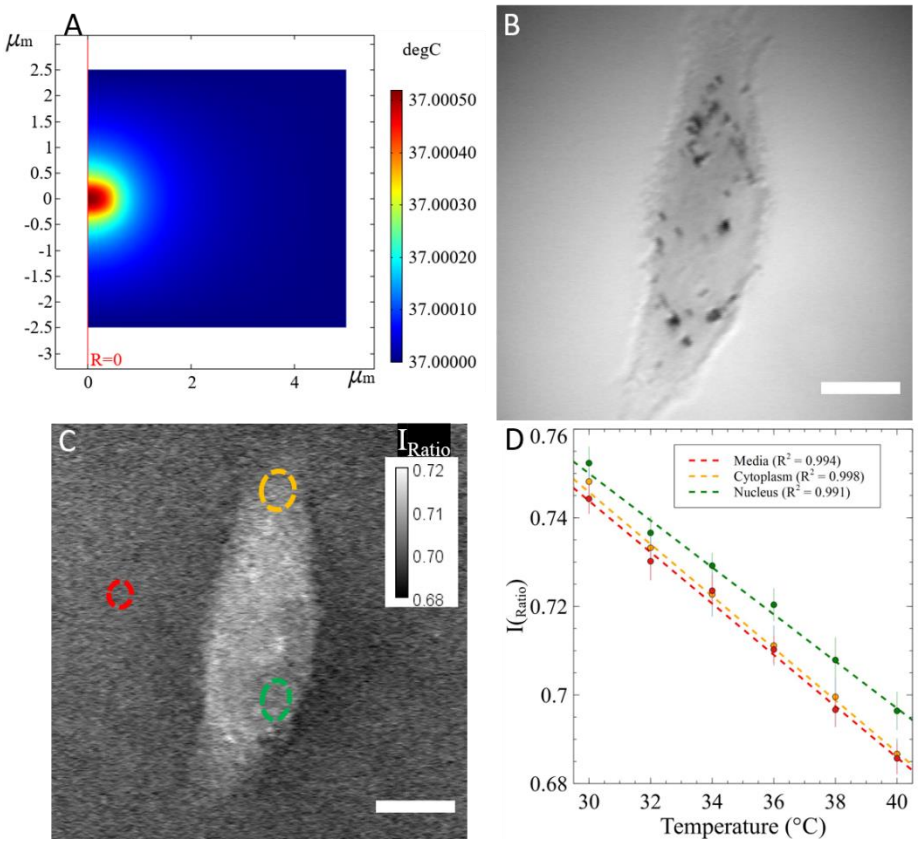

Figure 5.6 A) Simulation of a single mitochondrial heating within a cell set at 37°C. B-D) SRS Thermometry on live A549 cells kept at 37°C. Representative B) SRS image at 3420 cm^{-1} and C) SRS thermal map. D) Temperature calibration of intra and extracellular components. The scale bar is 10 μm.

5.6B-D). This does not reflect that live cells have lower temperature, but suggests that other factors in live cells contribute to the Raman ratio changes, such as the absorption of other molecules or changes in hydrogen bonding dynamics in intracellular compartments.[43,44] Nevertheless, in the temperature calibration experiment, the slopes of Raman ratio with respect to equilibrium temperature stay roughly the same for intracellular space and extracellular media. From the variation of Raman ratios within the cytoplasmic region, we argue that the temperature variation should be less than 0.79°C, which is much less than previous measurements with fluorescent sensors.

5.3 CONCLUSION

In conclusion, we describe the first example of a ratiometric SRS imaging technique for microscale, label-free temperature mapping and quantification. The measurement principle is based on the unique temperature dependence of the Raman band arising from O-H stretching vibrations of H_2O molecules. Using our recently developed broadband laser and an orthogonal modulation technique, two SRS images at 3220 cm^{-1} and 3420 cm^{-1} were simultaneously captured and the intensity ratio of these modes was calculated to determine temperature. Our calibration curve shows a reproducible linear relationship between the temperature and the intensity ratio in the range 30-42°C with a temperature resolution of 0.53°C in pure water.

We demonstrate real-time, label-free monitoring of the intracellular and extracellular-temperature changes of fixed cells under IR heating. Thermal conductivities are extracted by analyzing the thermal decay profiles of external heating on cellular components. Our measurement and simulation on live cells suggest that localized heating by mitochondria would be below 1°C, which cast doubt on the validity of previous endogenous thermogenesis studies reporting rises of a few Kelvins. Further investigation into composition-related spectral change in water-based

media will considerably increase the versatility of this technique, which could be applied in future applications such as microfluidic systems for the analysis and control of chemical reactions or biological processes. Because SRS is a three-dimensional imaging technique, it is also possible to extend this method to *in vivo* applications.

5.4 REFERENCES

1. Lowell, B. B. & Spiegelman, B. M. Towards a molecular understanding of adaptive thermogenesis. *Nature* **404**, 652–660 (2000).
2. Blaxter, K. *Energy Metabolism in Animals and Man*. (CUP Archive, 1989).
3. Monti, M., Brandt, L., Ikomi-Kumm, J. & Olsson, H. Microcalorimetric investigation of cell metabolism in tumour cells from patients with non-Hodgkin lymphoma (NHL). *Scandinavian Journal of Haematology* **36**, 353–357 (1986).
4. McCabe, K. M. & Hernandez, M. Molecular Thermometry. *Pediatric Research* **67**, 469–475 (2010).
5. Kim, M., Lee, J.-H. & Nam, J.-M. Plasmonic Photothermal Nanoparticles for Biomedical Applications. *Advanced Science* **6**, 1900471 (2019).
6. Okabe, K. *et al.* Intracellular temperature mapping with a fluorescent polymeric thermometer and fluorescence lifetime imaging microscopy. *Nature Communications* **3**, 1–9 (2012).
7. Yang, J.-M., Yang, H. & Lin, L. Quantum dot nano thermometers reveal heterogeneous local thermogenesis in living cells. *ACS Nano* **5**, 5067–5071 (2011).
8. Kucsko, G. *et al.* Nanometre-scale thermometry in a living cell. *Nature* **500**, 54–58 (2013).
9. Kiyonaka, S. *et al.* Genetically encoded fluorescent thermosensors visualize subcellular thermoregulation in living cells. *Nat. Methods* **10**, 1232–1238 (2013).
10. Homma, M., Takei, Y., Murata, A., Inoue, T. & Takeoka, S. A ratiometric fluorescent molecular probe for visualization of mitochondrial temperature in living cells. *Chem. Commun.* **51**, 6194–6197 (2015).
11. Chrétien, D. *et al.* Mitochondria are physiologically maintained at close to 50 °C. *PLOS Biology* **16**, e2003992 (2018).
12. Berezin, M. Y. & Achilefu, S. Fluorescence Lifetime Measurements and Biological Imaging. *Chem. Rev.* **110**, 2641–2684 (2010).
13. Baffou, G., Rigneault, H., Marguet, D. & Jullien, L. A critique of methods for temperature imaging in single cells. *Nature Methods* **11**, 899–901 (2014).
14. Suzuki, M., Zeeb, V., Arai, S., Oyama, K. & Ishiwata, S. The 10 5 gap issue between calculation and measurement in single-cell thermometry. *Nature Methods* **12**, 802–803 (2015).
15. Baffou, G., Rigneault, H., Marguet, D. & Jullien, L. Reply to: 'Validating subcellular thermal changes revealed by fluorescent thermosensors' and 'The 10 5 gap issue between calculation and measurement in single-cell thermometry'. *Nature Methods* **12**, 803–803 (2015).
16. Meier, B. J. K., Robert J. Determination of the Local Temperature at a Sample during Raman Experiments Using Stokes and Anti-Stokes Raman Bands - Bert J. Kip, Robert J. Meier, 1990. *Applied Spectroscopy* (2016).
17. LaPlant, F., Laurence, G. & Ben-Amotz, D. Theoretical and Experimental Uncertainty in Temperature Measurement of Materials by Raman Spectroscopy. *Appl. Spectrosc., AS* **50**, 1034–1038 (1996).
18. Kuriyama, R. & Sato, Y. Two-wavelength Raman imaging for non-intrusive monitoring of transient temperature in microfluidic devices. *Meas. Sci. Technol.* **25**, 095203 (2014).

19. Liu, K.-L. K., Davis, K. L. & Morris, M. D. Raman Spectroscopic Measurement of Spatial and Temporal Temperature Gradients in Operating Electrophoresis Capillaries. *Anal. Chem.* **66**, 3744–3750 (1994).
20. Cheng, J.-X. & Xie, X. S. Vibrational spectroscopic imaging of living systems: An emerging platform for biology and medicine. *Science* **350**, aaa8870 (2015).
21. Hill, A. H. & Fu, D. Cellular Imaging Using Stimulated Raman Scattering Microscopy. *Analytical Chemistry* (2019) doi:10.1021/acs.analchem.9b02095.
22. Figueroa, B. *et al.* Broadband hyperspectral stimulated Raman scattering microscopy with a parabolic fiber amplifier source. *Biomed. Opt. Express, BOE* **9**, 6116–6131 (2018).
23. He, R. *et al.* Dual-phase stimulated Raman scattering microscopy for real-time two-color imaging. *Optica* **4**, 44 (2017).
24. Francis, A., Berry, K., Chen, Y., Figueroa, B. & Fu, D. Label-free pathology by spectrally sliced femtosecond stimulated Raman scattering (SRS) microscopy. *PLOS ONE* **12**, e0178750 (2017).
25. Walrafen, G. E., Hokmabadi, M. S. & Yang, W. -H. Raman isosbestic points from liquid water. *J. Chem. Phys.* **85**, 6964–6969 (1986).
26. Gota, C., Okabe, K., Funatsu, T., Harada, Y. & Uchiyama, S. Hydrophilic Fluorescent Nanogel Thermometer for Intracellular Thermometry. *J. Am. Chem. Soc.* **131**, 2766–2767 (2009).
27. Donner, J. S., Thompson, S. A., Kreuzer, M. P., Baffou, G. & Quidant, R. Mapping intracellular temperature using green fluorescent protein. *Nano Lett.* **12**, 2107–2111 (2012).
28. Takei, Y. *et al.* A Nanoparticle-Based Ratiometric and Self-Calibrated Fluorescent Thermometer for Single Living Cells. *ACS Nano* **8**, 198–206 (2014).
29. Hu, J.-J., Cheng, Y.-J. & Zhang, X.-Z. Recent advances in nanomaterials for enhanced photothermal therapy of tumors. *Nanoscale* **10**, 22657–22672 (2018).
30. Peterman, E. J. G., Gittes, F. & Schmidt, C. F. Laser-Induced Heating in Optical Traps. *Biophysical Journal* **84**, 1308–1316 (2003).
31. Schönle, A. & Hell, S. W. Heating by absorption in the focus of an objective lens. *Opt. Lett., OL* **23**, 325–327 (1998).
32. Català, F., Marsà, F., Montes-Usategui, M., Farré, A. & Martín-Badosa, E. Influence of experimental parameters on the laser heating of an optical trap. *Scientific Reports* **7**, 1–9 (2017).
33. Mao, H., Ricardo Arias-Gonzalez, J., Smith, S. B., Tinoco, I. & Bustamante, C. Temperature Control Methods in a Laser Tweezers System. *Biophysical Journal* **89**, 1308–1316 (2005).
34. Haro-González, P. *et al.* Quantum Dot-Based Thermal Spectroscopy and Imaging of Optically Trapped Microspheres and Single Cells. *Small* **9**, 2162–2170 (2013).
35. Nourhashemi, M., Mahmoudzadeh, M. & Wallois, F. Thermal impact of near-infrared laser in advanced noninvasive optical brain imaging. *Neurophotonics* **3**, (2016).
36. Picot, A. *et al.* Temperature Rise under Two-Photon Optogenetic Brain Stimulation. *Cell Rep* **24**, 1243-1253.e5 (2018).
37. Podgorski, K. & Ranganathan, G. Brain heating induced by near-infrared lasers during multiphoton microscopy. *J Neurophysiol* **116**, 1012–1023 (2016).
38. Doukas, A. G. & Flotte, T. J. Physical characteristics and biological effects of laser-induced stress waves. *Ultrasound in Medicine & Biology* **22**, 151–164 (1996).

39. Appendix B Thermophysical Properties of Water. in *Drying Phenomena* 457–459 (John Wiley & Sons, Ltd, 2015). doi:10.1002/9781118534892.app2.
40. Kyoo Park, B. *et al.* Thermal conductivity of bovine serum albumin: A tool to probe denaturation of protein. *Appl. Phys. Lett.* **99**, 163702 (2011).
41. Loesberg, C., van Miltenburg, J. C. & van Wuk, R. Heat production of mammalian cells at different cell-cycle phases. *Journal of Thermal Biology* **7**, 209–213 (1982).
42. Johnson, M. D. *et al.* Universal constant for heat production in protists. *PNAS* **106**, 6696–6699 (2009).
43. Nuriya, M. *et al.* Characterization of Intra/Extracellular Water States Probed by Ultrabroadband Multiplex Coherent Anti-Stokes Raman Scattering (CARS) Spectroscopic Imaging. *J. Phys. Chem. A* **123**, 3928–3934 (2019).
44. Sugimura, T., Kajimoto, S. & Nakabayashi, T. Label-Free Imaging of Intracellular Temperature by Using the O−H Stretching Raman Band of Water. *Angewandte Chemie International Edition* **59**, 7755–7760 (2020).

Chapter 6: Conclusions and Future Directions

6.1 WHAT'S NEXT?

I began this Ph.D. journey with the hope that I could help extend our ability to view the unobservable. Among the many spectroscopic techniques, SRS is a premier tool to study the interplay between molecular identification and function in biomedical imaging; thus, the aim of most of the work in this dissertation was to improve the ability of SRS to reveal cellular machinery and enable early-cancer diagnosis. However, it would be naïve to consider that SRS has reached a level where it outperforms other biomedical microscopies. In typical SRS labs, a combination of other modalities such as fluorescence, SHG, TPA, etc., are combined with SRS to provide a more complete chemical analysis. Although these methods, provide excellent sensitivity and orthogonal information, ideally, one would like to employ one imaging technique to gather all chemical information with suitable sensitivity, speed, and spatial resolution. I briefly discuss in the next sections some of the key developments in SRS microscopy that I believe will further propel SRS to the forefront of biomedical microscopy.

The biggest challenge limiting the application of SRS in biology and medicine is its relatively low sensitivity. By increasing data acquisition times and irradiation intensities, one can get higher sensitivity, albeit at the risk of damaging the sample. Additionally, when using higher peak powers, the SRS signal is also accompanied by a parasitic background signal which stems from a combination of nonlinear transient scattering processes (cross-phase modulation, photothermal lensing, etc.). One popular way to negate background contributions in spectral focusing experiments is a technique known as frequency modulation (FM), where two SRS signals at different Raman excitation frequencies are directly subtracted in real-time to remove the parasitic background, taking advantage of the narrowband nature of SRS and broadband nature of the

parasitic background. Recently our lab improved on this technique by employing alignment-free polarization encoding via a birefringent crystal in combination with the developed broadband fiber amplifier to further suppress the parasitic background by 40%.[1] Combining this new FM technique with pre-resonance and/or rigorous electronic SRS pumping, which provides ~10^8 signal enhancement at the cost of increased parasitic contribution,[2,3] should further increase the current sensitivity of SRS.

6.2 SENSITIVE HYPERSPECTRAL SRS WITH A WAVELENGTH TUNABLE OPO

Another way to increase sensitivity is to employ shorter excitation wavelengths. It is well known that the Raman scattering cross-section is proportional to the fourth power of the excitation frequency, therefore, to increase the sensitivity of our SRS system we have recently developed a highly sensitive dual wavelength-tunable laser source. All current SRS imaging systems use near-infrared (NIR) lasers for excitation. This is because most applications are intended for biological imaging, where cell damage and tissue penetration are major concerns at shorter wavelengths. Additionally, the current choice of excitation wavelengths is severely limited by the laser sources available. The Stokes laser is typically limited to either 1064 nm or 1040 nm, with a tunable pump wavelength to match the Raman transition of interest. Thus by converting the fixed 1040 nm output to a shorter-wavelength tunable optical parametric oscillator (OPO), we are no longer constrained by NIR laser beams and can now move into the red portion of the visible spectrum to improve our sensitivity. The femtosecond OPO is based on a lithium triborate (LBO) crystal pumped by a frequency-doubled Yb fiber laser-amplifier system. In addition to larger cross-sections, the shorter wavelength of the excitation beams also brings the excitation frequencies closer to the molecular

absorption transitions of many endogenous compounds. For vibrational modes that are strongly coupled to these transitions, the corresponding SRS response is significantly enhanced.[2,4]

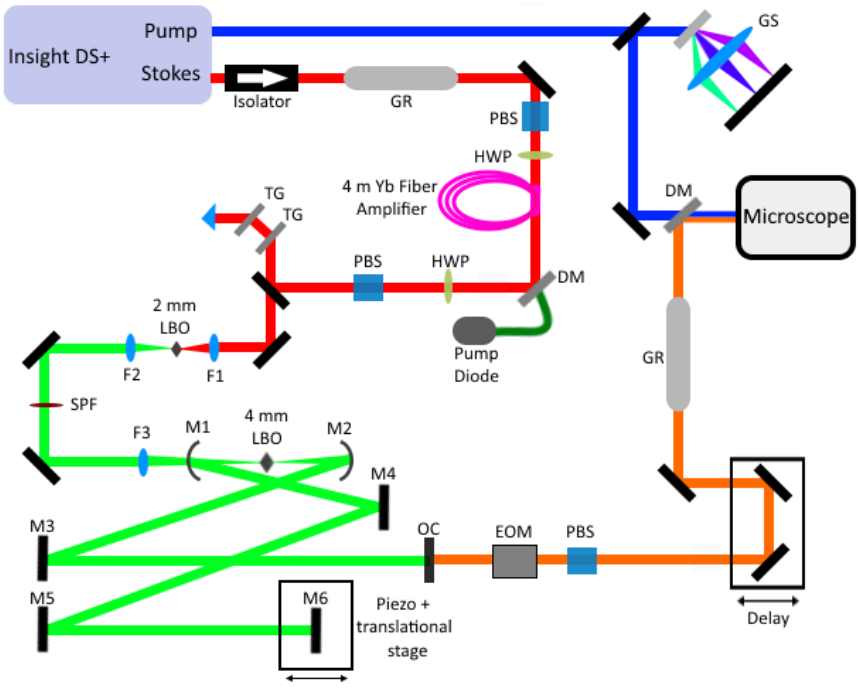

Figure 6.1 Setup of the ytterbium-fiber laser-amplifier system pumped LBO-OPO. GR, glass rod; PBS, polarizing beam splitter; HWP, half-wave plate; DM, dichroic mirror; TG, transmission grating; F1/2/3, focusing lens; SPF shortpass filter; M1/2/3/4/5/6, cavity mirrors; OC, output coupler; EOM, electro-optic modulator; GS, grating stretcher.

The experimental setup is shown in Fig. 6.1. The Insight DS+ (Spectra-Physics) outputs two beams with an 80 MHz repetition rate. The two outputs are a tunable beam ranging from 680-1300 nm (pump), and a fixed beam at 1040 nm (Stokes). To avoid nonlinear effects in the fiber amplifier, the Stokes beam is chirped by 72 cm of high dispersion H-ZF52A glass rods (GR) to undergo chirped pulse amplification in a 4-m polarization-maintaining Yb-doped fiber (PLMA-YDF-30/250-VIII Nufern). A half-wave plate was placed at the input to optimize the polarization of the seed pulse transmitting through the fiber. An average power of 80 mW at 1040 nm was amplified to 8 W pumped by 15 W from a fiber-coupled laser diode at 976 nm (BWT). The gain fiber is pumped via free space in the counter-propagation pumping scheme combined with the seed using a dichroic mirror. The double-clad fiber was coiled to a radius of 6 cm to suppress higher transverse

modes. A grating compressor consisting of transmission gratings (TG) with 1250 lines/mm (Ibsen photonic) was used to compress the pulses for efficient second harmonic generation (SHG). After compression, the pulses were frequency-doubled in a 2 mm long LBO crystal (Laserton), cut for type 1 phase-matching I the xy-plane ($e \rightarrow o + o$, $\theta = 90°$, $\varphi = 12.9°$), to provide the pump radiation for the OPO. We obtained up to 3.5 W of pulsed radiation at a center wavelength of 520 nm. After the LBO crystal, the remaining fundamental beam was filtered out by a short pass filter FESH1000 (Thorlabs). The linear OPO cavity was singly resonant for the signal wavelength and formed by two curved mirrors (M1/M2) with a radius of curvature of -150 mm (f = 80 mm) and five plane mirrors. Two of these five mirrors were the end mirrors of the linear cavity (OC/M6), and three were folding mirrors (M3/M4/M5). OC mirror acted as the output coupler for the signal radiation and its transmission (10%) over the range of 700-900 nm. All other mirrors were designed to have more than 99.9% reflectivity over a spectral range from 710-890 nm ±10 nm (Layertec). The second end mirror M6 was mounted on a mechanical translation stage with an additional piezo actuator for coarse and fine adjustment of the cavity lengths, respectively. The OPO was based on a 4 mm LBO crystal (Laserton) cut for type 1 ($e \rightarrow o + o$) noncritical phase matching in the xy-plane ($\theta = 90°$, $\varphi = 0°$).

An electro-optical modulator (EOM) in then placed in the OPO signal beam, which will be denoted as the Stokes beam, modulating at 20 MHz. A motorized delay line is inserted into the Stokes beam to scan the time delay between the pump and the Stokes. The Stokes beam was then chirped by traveling through 60 cm of high dispersion GR. Meanwhile, the pump beam was chirped by a single grating stretcher (GS) to match the chirp of the Stokes beam. Next, the two beams are spatially overlapped using a dichroic mirror (DM) before they were sent into a home-built laser scanning microscope (Nikon, Eclipse FN1) for SRS imaging. A 63× Leica water

immersion objective was used to focus the beams onto the sample with a power of ~80 mW for each beam. For signal detection, the Stokes beam was filtered out using a short-pass filter (SPF), and the pump beam was detected using a large area silicon photodiode (Hamamatsu). The SRS signal was detected with a Zurich Instruments lock-in amplifier (H2FLI).

6.2.1 Preliminary Results

We first characterized the pulse properties of the OPO. Figure 6.2A shows the wavelengths attainable by adjusting the cavity length of the end mirror M6. As expected, available outputs range from ~760 – 870 nm, which is within the range of the high reflection mirrors. Signal powers of the OPO as a function of wavelength are shown in Figure 6.2B. Excluding the upper and lower spectral limits, the OPO generated more than 400 mW of usable signal power. To obtain the available wavelengths within the range of the mirrors, we would need to simply change the angle of the 2 mm LBO crystal which would also increase the power of these wavelengths. The average output pulse duration ~350 fs, which will be chirped by high dispersion glass for hyperspectral SRS imaging.

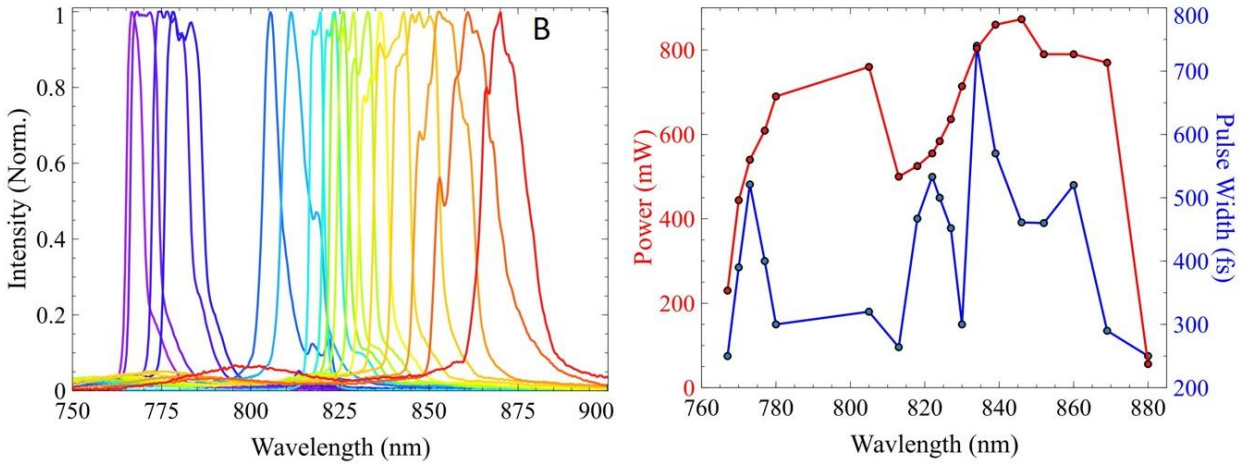

Figure 6.2 OPO output characteristics. A) Tuning of the LBO-OPO signal wavelength. B)Signal power and pulse duration of the OPO as a function of wavelength.

For proof of concept, we obtained the SRS spectrum of deuterated dimethyl sulfoxide (DMSO) with our original laser system, and with our homebuilt OPO (Figure 6.3). From this figure, it is evident that using shorter wavelengths increases our generated SRS signal by ~1.75x using the same excitation intensities for both schemes. From theory, we should expect a 2.4x increase through the relation of the cross-section to the excitation frequencies ($\sigma_{SRS} \propto \omega_p * \omega_S^3$). By proper optimization of chirp and beam alignment, the remaining enhancement can be achieved, providing an avenue for sensitive SRS microscopy.

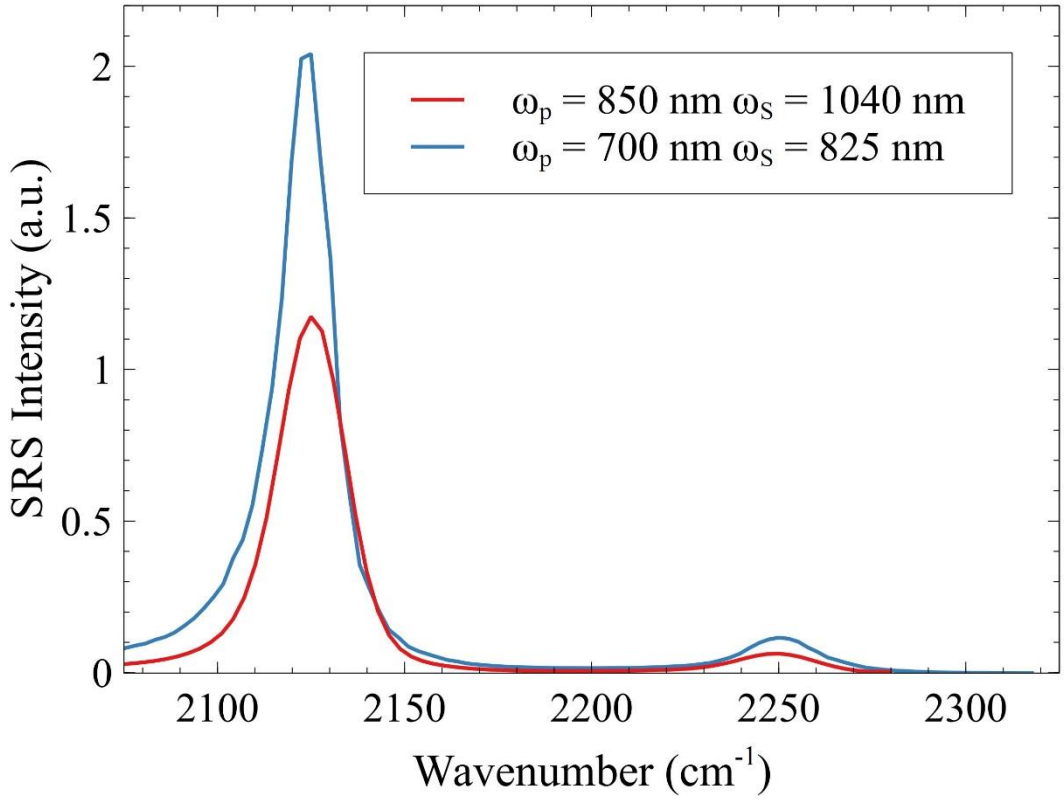

Figure 6.3. Comparison of SRS signal between shorter and longer excitation wavelengths

6.3 INCREASING SPATIAL RESOLUTION

Spatial resolution is another key parameter that can be improved in the near future. As most SRS labs employ NIR light for excitation, the typical lateral resolution of SRS microscopy is ~400 nm

and the axial resolution is 1–2 μm, which although fine for most cases, it is unfortunately too low to resolve many relevant cellular structures. Therefore, inspired by successes in fluorescence microscopy, many research teams have proposed to combine the advantages of stimulated emission depletion microscopy with SRS microscopy.[5,6] But unlike fluorescence imaging processes, the efficient population and depopulation of relevant molecular eigenstates, which is required for most super-resolution techniques, is more difficult to accomplish for SRS.

Similar to increasing sensitivity by employing shorter excitation frequencies, a far easier way to achieve higher resolution is to interrogate the sample with shorter wavelengths. By using visible pump and Stokes beams and a 1.49 NA objective lens, SRS imaging was demonstrated on single cells and tissues at an impressive resolution of 130 nm.[7] Along with the higher resolution, the shorter wavelength of the excitation beams is tuned closer to the molecular absorption transitions of many endogenous molecules while concomitantly increasing the Raman scattering efficiency leading to improved sensitivity. Although one must take into consideration increased tissue scattering and photodamage, SRS microscopy with short wavelengths allow for resolving biological structures at the 100 nm scales in fixed cells and thin tissue samples. Combining these shorter wavelengths with plasmonic nanomaterials will further boost the SRS signal which will truly allow SRS to provide high sensitivity along with an increased resolution for single-molecule detection.[8]

6.4 IMAGING DEPTH

In terms of penetration depth, SRS (along with other nonlinear optical imaging techniques) is severely limited due to the turbidity and heterogeneity of tissue. Due to light scattering, the SNR of SRS microscopy deteriorates rapidly with imaging depth and reaches an effective imaging distance of around ~100 μm. This is exacerbated for thick samples where the pump and Stokes

photons are continually scattered as they reach their focal imaging plane leading to larger out-of-focus SRS signal generation, which reduces image quality and sensitivity. Currently, there are a few methods to improve the signal size and imaging depth. The easiest method would be to employ longer excitation wavelengths to increase imaging depths due to less scattering at these wavelengths. However, this comes with a reduction in SRS signal intensity. Another method would be to correct for optical aberration by employing adaptive optics (deformable mirrors) to pre-compensate for the refractive-index inhomogeneities in biological specimens, which would require *a priori* knowledge of the tissue aberration, which could be difficult to determine.[9] Tissue clearing methods can also be used, albeit at the risk of altering tissue structure and its incompatibility with live specimens (bar skull clearing).[10] An alternative method would be to adapt the technique implemented by Jian *et al.* in using a non-collinear excitation for pump-probe microscopy.[11] This method employed using a cross-beam strategy to significantly improve the axial resolution when imaging through low NA lenses to provide an alternative way for depth-resolved, large FOV imaging. With this method, the modulated and unmodulated excitation beams in SRS would be spatially separated, decreasing out-of-focus SRS signal generation, therefore increasing imaging depth. While the lower NA (0.7) reduces resolving power, the 3 μm lateral resolution is still acceptable for many cell types (e.g. neuron, red blood cells).

6.5 CLINICAL SRS

Lastly, the end goal is not only to improve SRS microscopy for basic research but by implementing these key improvements we can cement SRS microscopy as an indispensable tool for clinical use. As discussed throughout this thesis, SRS has shown tremendous activity in cancer diagnostics, stain-free histopathology, pharmaceutical research, and other biomedically relevant fields. However, owing to its complex excitation scheme, diagnostic SRS systems are rarely found

in clinical settings. This has led to intense technical development in easing the clinical adaption of SRS, including endoscopes[12] and handheld microscopes[13]. One of the best ways to ensure a cheap, compact, and alignment-free SRS system is by employing all-fiber light sources. The most common optical fibers used are those that are doped with gain media of Yb and Er, allowing for operation near 1 and 1.5 μm, respectively. Leveraging the advantages of fiber optics, an integrated clinical system for SRS was developed to be housed in a portable cart for intraoperative optical histology by Orringer *et al*.[14] However, as the system consisted solely of Yb and Er-doped fibers, the C-H (2700-3100 cm^{-1}) region was the only region accessible due to the limited gain bandwidth of the gain media. This limited tuning range falls short of being able to pursue relevant applications such as the detection of deuterated drugs and visualization of metabolism via deuterium oxide probing around ~2200 cm^{-1} and tumor classification in the fingerprint region.[15–17] To this end, Brinkmann *et al*. recently developed a rapidly tunable (>2700 cm^{-1}) dual-output all-fiber light source for CARS imaging.[18] The wide and rapid tunability was achieved by a novel tuning concept for OPOs, based on a rapidly tunable filter and a specifically chirped fiber Bragg grating as the output coupler, both within the master laser pumping the OPO. I expect that this technique will be extended soon to SRS for clinical usage.

Overall, improvements in SRS microscopy continue and have increased dramatically in the past 10 years. Combined with advancements in machine learning,[19,20] further developments will allow even more applications and has the potential to improve human health and well-being by providing fundamental knowledge in cellular metabolism and early disease diagnosis. The novel imaging applications and improvements described in this thesis will undoubtedly contribute to this rapidly developing area of research.

6.6 REFERENCES

1. Hill, A. H., Munger, E., Francis, A. T., Manifold, B. & Fu, D. Frequency Modulation Stimulated Raman Scattering Microscopy through Polarization Encoding. *J. Phys. Chem. B* (2019) doi:10.1021/acs.jpcb.9b07075.
2. Wei, L. *et al.* Super-multiplex vibrational imaging. *Nature* **544**, 465–470 (2017).
3. Shi, L. *et al.* Electronic Resonant Stimulated Raman Scattering Micro-Spectroscopy. *J. Phys. Chem. B* **122**, 9218–9224 (2018).
4. Wei, L. & Min, W. Electronic Preresonance Stimulated Raman Scattering Microscopy. *J. Phys. Chem. Lett.* **9**, 4294–4301 (2018).
5. Gong, L. & Wang, H. Breaking the diffraction limit by saturation in stimulated-Raman-scattering microscopy: A theoretical study. *Phys. Rev. A* **90**, 013818 (2014).
6. Silva, W. R., Graefe, C. T. & Frontiera, R. R. Toward Label-Free Super-Resolution Microscopy. *ACS Photonics* **3**, 79–86 (2016).
7. Bi, Y. *et al.* Near-resonance enhanced label-free stimulated Raman scattering microscopy with spatial resolution near 130 nm. *Light: Science & Applications* **7**, 1–10 (2018).
8. Zong, C. *et al.* Plasmon-enhanced stimulated Raman scattering microscopy with single-molecule detection sensitivity. *Nature Communications* **10**, 1–11 (2019).
9. Wright, A. J. *et al.* Adaptive optics for enhanced signal in CARS microscopy. *Opt Express* **15**, 18209–18219 (2007).
10. Chen, Y. *et al.* Coherent Raman Scattering Unravelling Mechanisms Underlying Skull Optical Clearing for Through-Skull Brain Imaging. *Anal. Chem.* **91**, 9371–9375 (2019).
11. Jiang, J., Warren, W. S. & Fischer, M. C. Crossed-beam pump-probe microscopy. *Opt. Express, OE* **28**, 11259–11266 (2020).
12. Lombardini, A. *et al.* High-resolution multimodal flexible coherent Raman endoscope. *Light: Science & Applications* **7**, 10 (2018).
13. Liao, C.-S. *et al.* In Vivo and in Situ Spectroscopic Imaging by a Handheld Stimulated Raman Scattering Microscope. *ACS Photonics* **5**, 947–954 (2018).
14. Orringer, D. A. *et al.* Rapid intraoperative histology of unprocessed surgical specimens via fibre-laser-based stimulated Raman scattering microscopy. *Nat. Biomed. Eng.* **1**, 0027 (2017).
15. Wei, L., Yu, Y., Shen, Y., Wang, M. C. & Min, W. Vibrational imaging of newly synthesized proteins in live cells by stimulated Raman scattering microscopy. *PNAS* **110**, 11226–11231 (2013).
16. Shi, L. *et al.* Optical imaging of metabolic dynamics in animals. *Nat Commun* **9**, (2018).
17. Figueroa, B. *et al.* Broadband hyperspectral stimulated Raman scattering microscopy with a parabolic fiber amplifier source. *Biomed. Opt. Express, BOE* **9**, 6116–6131 (2018).
18. Brinkmann, M. *et al.* Portable all-fiber dual-output widely tunable light source for coherent Raman imaging. *Biomed. Opt. Express, BOE* **10**, 4437–4449 (2019).
19. Manifold, B., Thomas, E., Francis, A. T., Hill, A. H. & Fu, D. Denoising of stimulated Raman scattering microscopy images via deep learning. *Biomed. Opt. Express, BOE* **10**, 3860–3874 (2019).
20. Hollon, T. C. *et al.* Near real-time intraoperative brain tumor diagnosis using stimulated Raman histology and deep neural networks. *Nature Medicine* **26**, 52–58 (2020).

Appendix A.

Appendix A accompanies Chapter 2: Label-Free Chemical Imaging with Stimulated Raman Scattering Microscopy

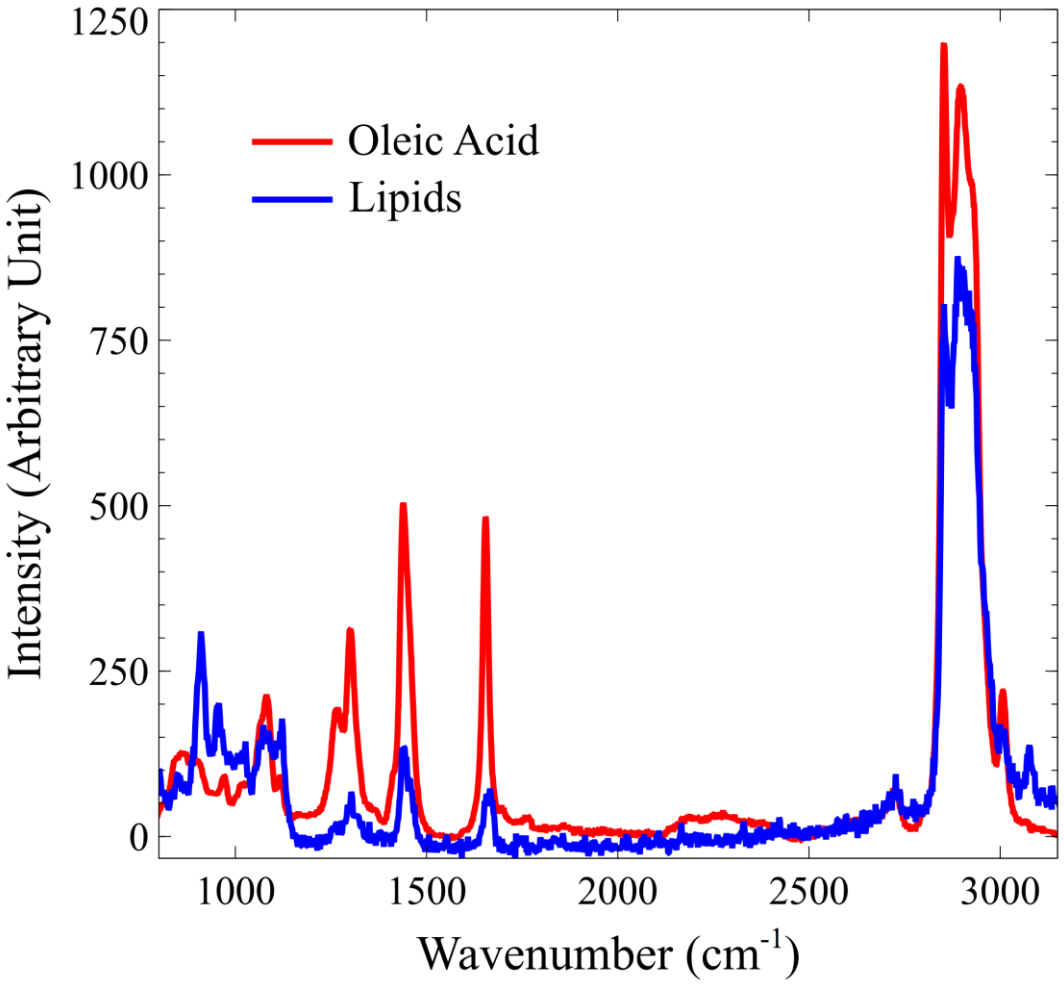

Figure A.1 Spontaneous Raman spectra of the lipid from a LFP and oleic acid

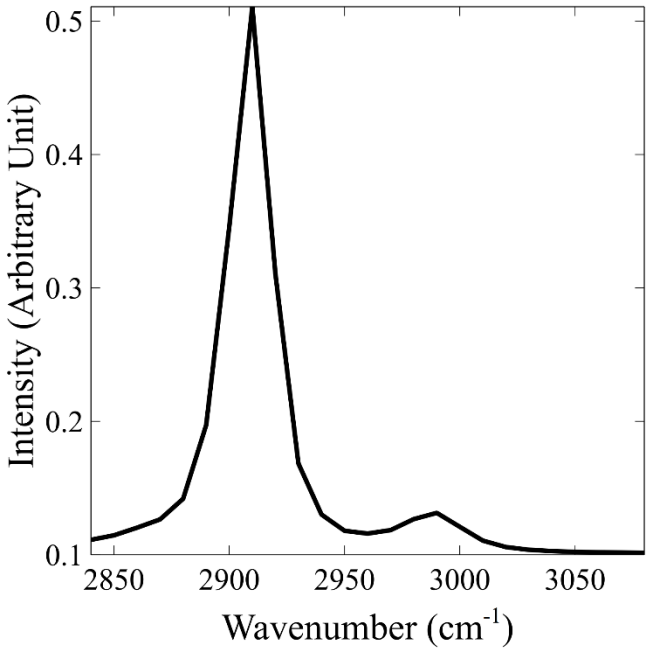

Figure A.2 SRS spectra of DMSO for the calibration of lipids

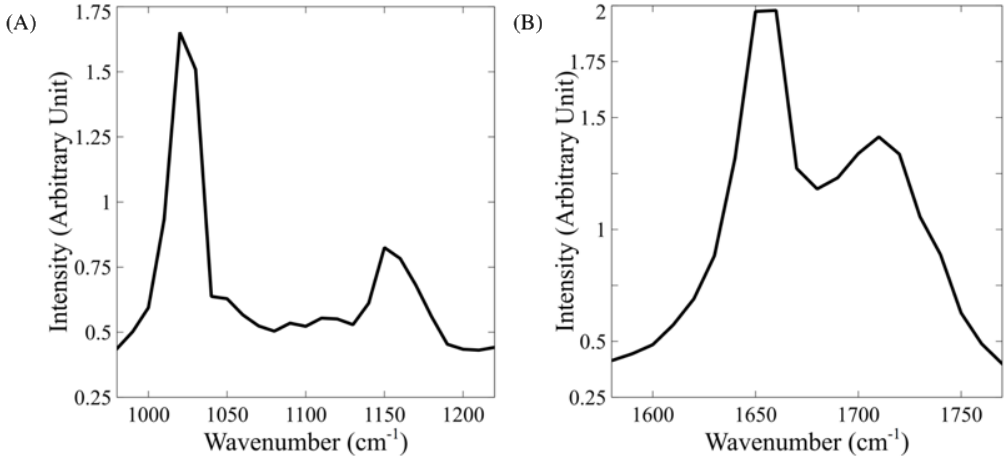

Figure A.3 SRS spectra of (A) Napthalene and (B) mixture of oleic acid and acetone, for calibration of SRS wavenumbers near 1100 cm^{-1} and 1700 cm^{-1}, respectively.

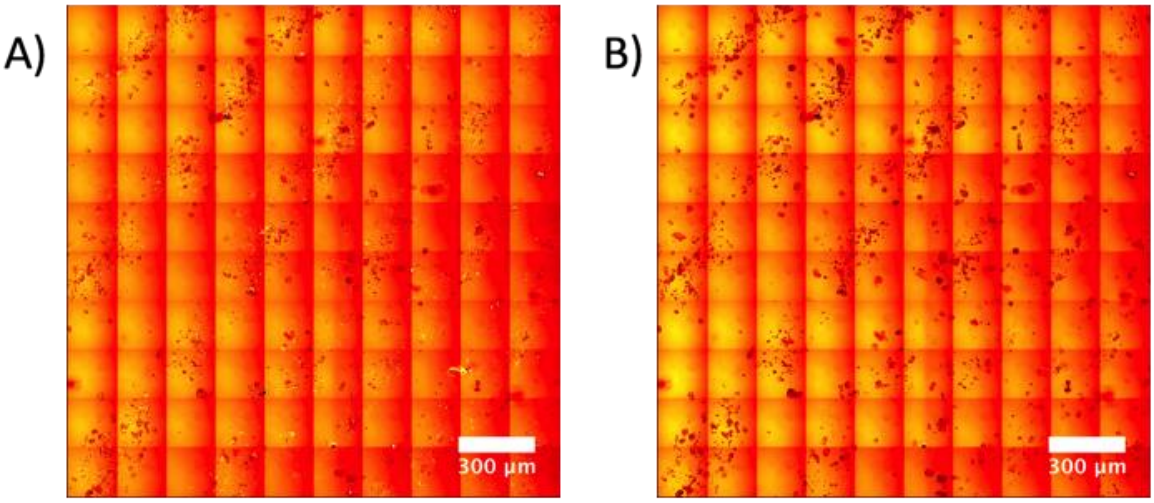

Figure A.4 SRS images of LPA on tape at (A) 2872 cm^{-1} and B) 3015 cm^{-1}

Appendix B

Appendix B accompanies Chapter 3: Detecting and Quantifying Microscale Chemical Reactions with Stimulated Raman Scattering Microscopy

Samples	Formulation composition	Stress condition
Binary formulation at 90% DL of PIO-HCl	10% d-Mgst and 90% PIO-HCl	5C, unstressed
	10% d-Mgst and 90% PIO-HCl	40C/75%RH for 9 days
	10% Mgst and 90% PIO-HCl	5C, unstressed
	10% Mgst and 90% PIO-HCl	40C/75%RH for 9 days
Binary formulation at 99% DL of PIO-HCl	1% 2H-MgST and 99% PIO-HCl	5C, unstressed
	1% 2H-MgST and 99% PIO-HCl	40C/75%RH for 9 days
	1% MgST and 99% PIO-HCl	5C, unstressed
	1% MgST and 99% PIO-HCl	40C/75%RH for 9 days
Multicomponent formulation at 1% DL of PIO-HCl	1% PIO-HCl, 1% 2H-MgSt and 98% placebo blend	5C, unstressed
	1% PIO-HCl, 1% 2H-MgSt and 98% placebo blend	40C/75%RH for 9 days
	1% PIO-HCl, 1% MgSt and 98% placebo blend	5C, unstressed
	1% PIO-HCl, 1% MgSt and 98% placebo blend	40C/75%RH for 9 days

Table B.1 Formulation composition and stress conditions

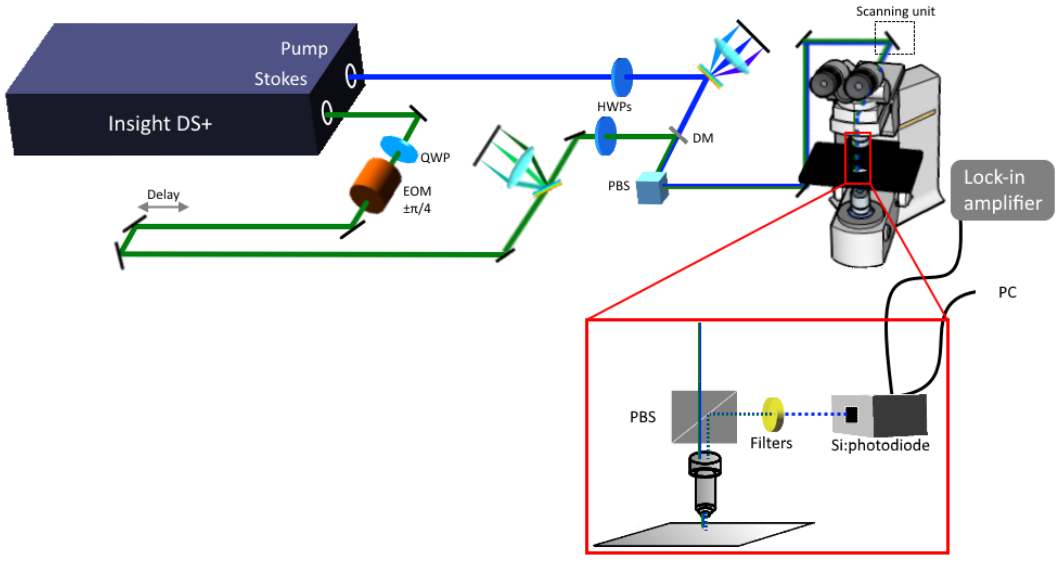

Figure B.1 Schematic diagram of the hyperspectral SRS imaging setup based on a femtosecond dual beam laser system. Abbreviations: QWP, quarter waveplate; EOM, electro-optical modulator; HWP, half waveplate; PBS, polarizing beam splitter; DM, dichroic mirror; SPF, short–pass filter; PD, photodiode.

Spectral coverage of our hyperspectral SRS microscope is limited by the spectral bandwidths of the laser source <300 cm^{-1}, therefore tuning of the pump wavelength is required to cover larger spectral information. To probe the region between 1560-1760 cm^{-1} corresponding solely to PIO-HCl and PIO-FB, the pump wavelength was tuned to 890 nm (Fig. 3.1). For the region between 1350 – 1560 cm^{-1}, corresponding to the excipient region, the pump wavelength was tuned to 905 nm.

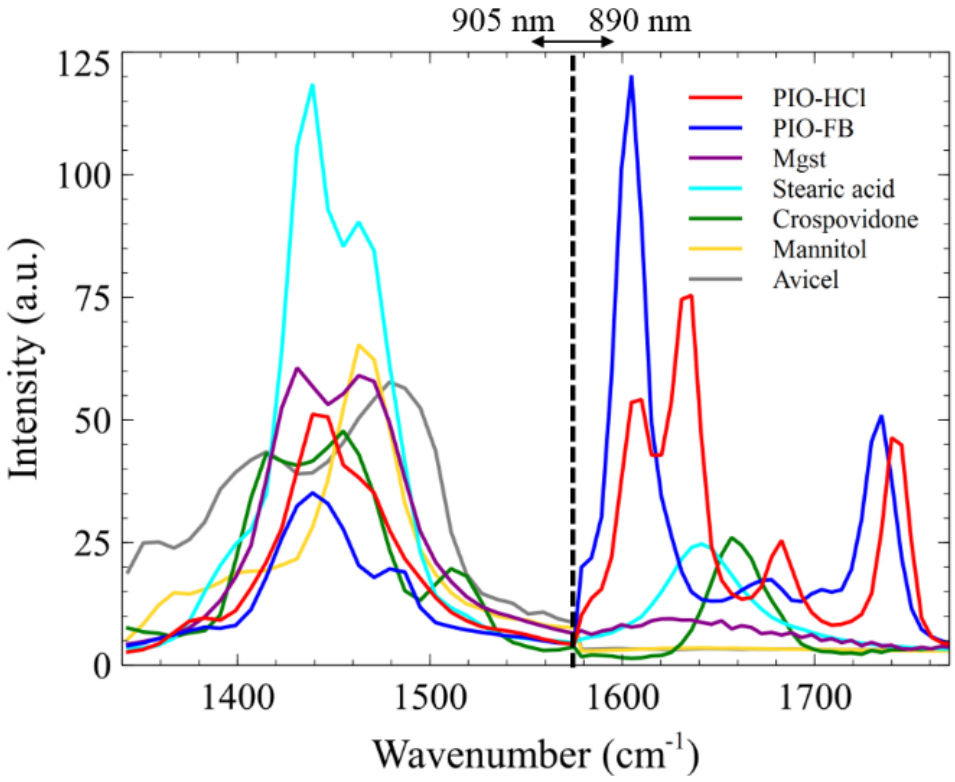

Figure B.2. SRS spectra of API and excipients found within our multicomponent tablet. 905 nm pump excitation for the region between 1340-1570 cm^{-1}. 890 nm pump excitation for the region between 1570-1770 cm^{-1}. I_P, I_S = 40 mW

We first acquired SRS spectra of individual chemical ingredients within a tablet, including Pioglitazone (HCl salt and free base), Mgst, stearic acid, Crospovidone, Mannitol, and Avicel (Fig. B.2) For comparison, the spontaneous Raman spectra of these compounds are shown in the supplementary information Figure B.3. For PLS model development, hyperspectral imaging between the spectral region of 1560-1760 cm^{-1} was investigated to mitigate the interference of the excipient components, which are largely Raman inactive.[1] Low intensity spectral peaks pertaining to stearic acid and Crospovidone (1650 and 1660 cm^{-1}, respectively) are noted within this region, however the strong spectral differences between PIO-HCl salt and PIO-FB are readily differentiated as seen in Fig. 3.1 and B.2. PIO-HCl exhibits a doublet located ~ 1610-1640 cm^{-1}, as opposed to the singlet present in the PIO-FB spectrum in the same region. This spectral difference is attributed to a change in the vibrational modes of the pyridine ring and the carbonyl

group after protonation.[2] Because stearic acid is not an initial chemical component, we hypothesize that the presence of the broad 1645 cm^{-1} peak due to the hydroxyl vibration should further confirm the disproportionation reaction due to the COO^- group of Mgst acting as a proton acceptor, forming $MgCl_2$ and stearic acid as byproducts. Thus, we chose to probe the hydroxyl group of stearic acid in our data analysis. For spectral unmixing of the API, its free base, and the excipients, a non-negative least squares spectral unmixing approach was employed for the full spectral region between 1350-1760 cm^{-1}.

For PLS model generation, it can be seen from the spectral differences between PIO-HCl and PIO-FB in Fig. B.2 and B.3 that a derivative treatment of the spectra is not needed for building chemometric models as the free base is easily discernible within the spectral region of 1560-1760 cm^{-1}. In building our PLS model, standard normal variate (SNV) and mean centering were used to pre-process the spectra of the calibration standards. SNV is often employed as a preprocessing treatment in data generated by Near Infrared and Raman spectroscopy due to its ability to eliminate the multiplicative interferences from light scattering and particle size variations for solid state samples.[3–5] Two latent variables were chosen because it minimized root mean squares error of cross-validation (RMSECV) and explains 99.49% of X variance and 99.58% variance of Y for PIO-FB.

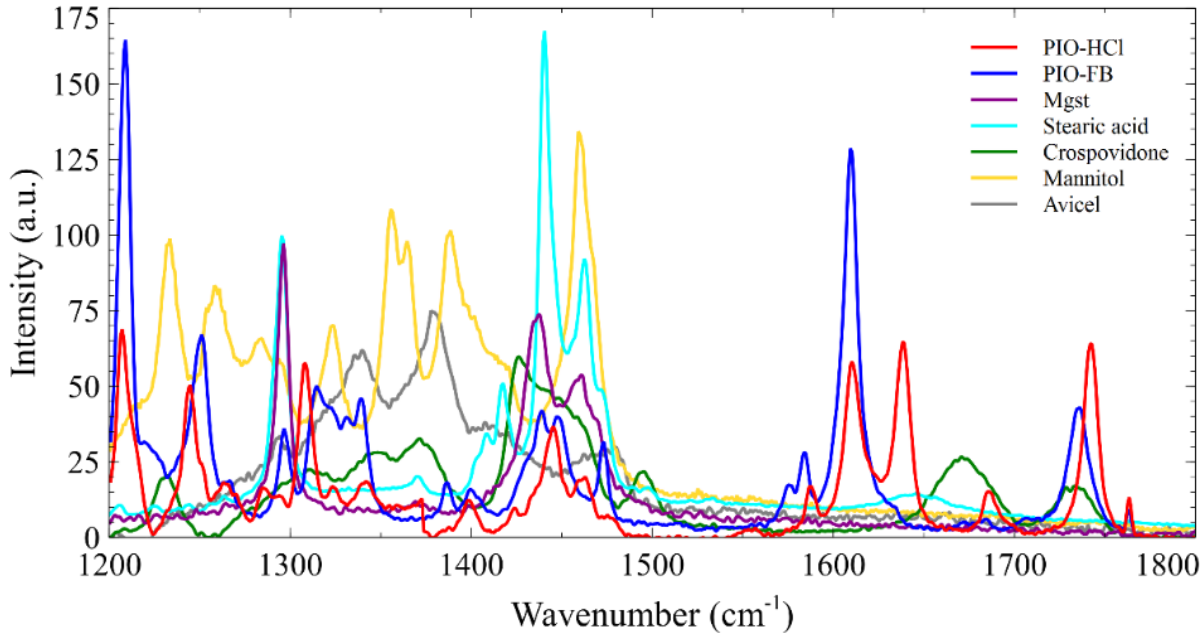

Figure B.3 Spontaneous Raman spectra of API and related excipients within the spectral region of 1200-1800 cm^{-1}.

We used a Renishaw InVia Raman microscope to collect the spectra of the molecular species. The microscope included a 785-nm excitation source. Spectra from 1200 cm^{-1} to 1800 cm^{-1} was collected at laser power of 50% and 20s acquisition time averaged 2 times.

To determine drug disproportionation in tablet formulations at low DL, we first applied single Raman-band SRS imaging to rapidly map the distribution of pioglitazone at 1% loading. Previously with Raman spectroscopy, DL at 5% w/w has been demonstrated, but further lowering the percentage of API creates a challenge due to the slow speed of spontaneous Raman measurements.[1] With SRS imaging, large area, high resolution imaging at selected Raman band can be readily achieved. We took two large-area images at 1610 cm-$^{-1}$ and 1660 cm^{-1} to locate pioglitazone and crospovidone over the entire surface of the tablet (7 x 7 mm) with 500 nm resolution. Fig. S4 shows the merged image of the two channels which is composed of stitched 35 x 35 SRS frames. Total acquisition time for each channel was ~45 minutes. It is apparent that even

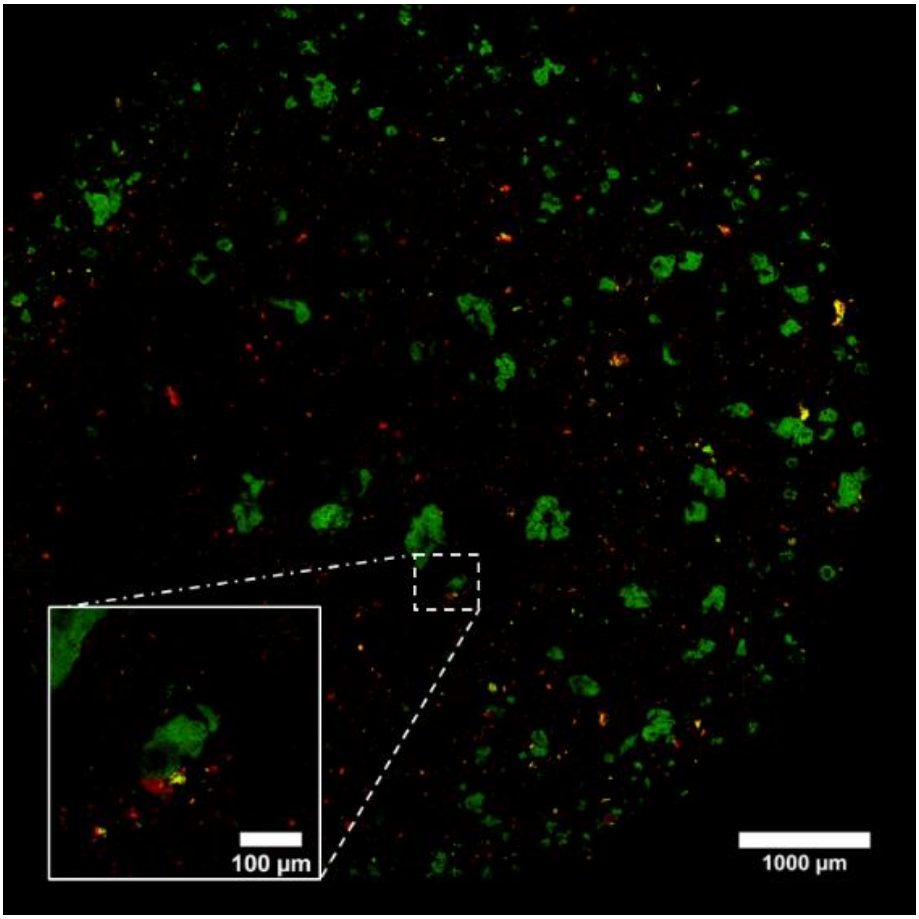

Figure B.4 Large area SRS image obtained by merging single-band SRS images at 1610 cm^{-1} and 1660 cm^{-1}. Green pixels represent crospovidone and red pixels represent Pioglitazone. Insert is an 8x magnification of the image indicated by a dashed square

at 1% DL and 5% crospovidone, both the API and the inert excipient are easily detected and distributed heterogeneously throughout the tablet.

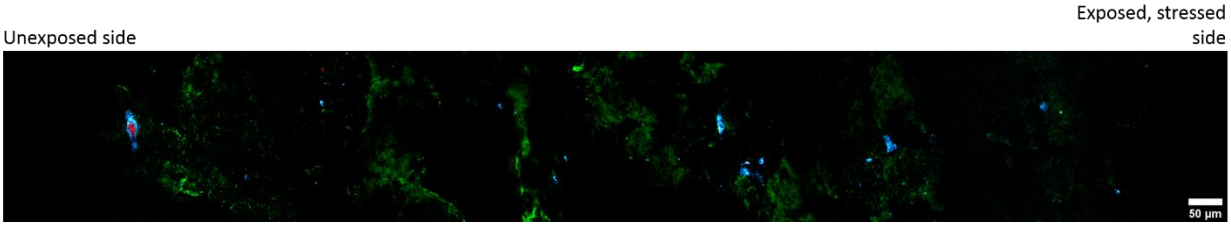

Figure B.5 Cross-sectional image of a control tablet stressed at 45 °C and 60% RH for 90 hours. Green, red, and blue pixels represent crosprovidone, PIO-HCl, and PIO-FB, respectively.

To confirm that the disproportionation reaction occurs largely at the surface, where the exposure to the stressing environment is more pronounced, we performed cross-sectional imaging of a stressed tablet using our SRS microscope. This was achieved by cutting the tablet radially by a razor blade, followed by microtome cutting to produce a smoother surface for imaging. The tablet was then flipped on its curved surface, which allowed for cross-sectional imaging (Fig. B.5). Furthermore, imaging was done right below the surface to reduce aberrations due irregular surface due to the cutting process.

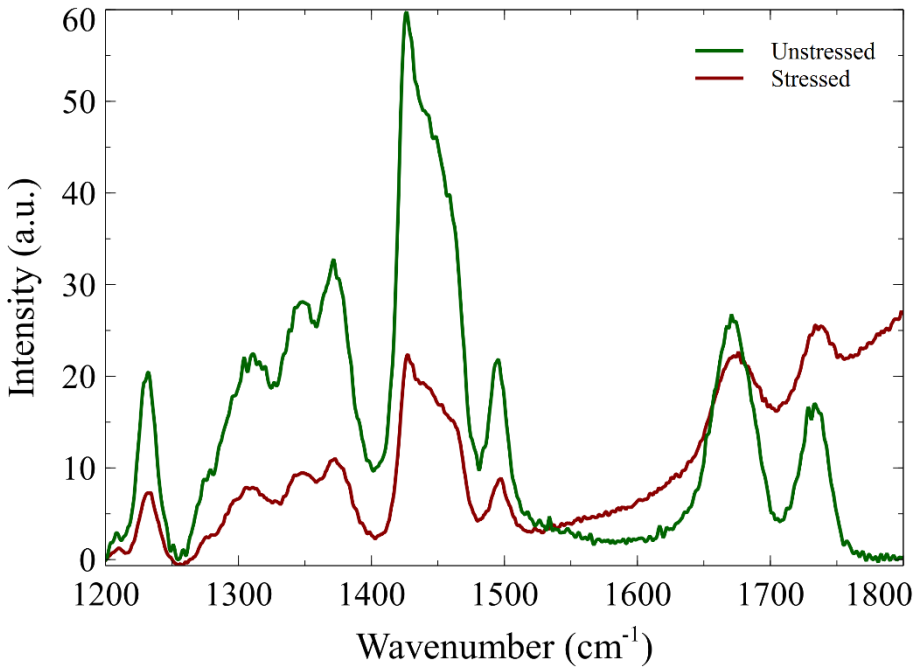

Figure B.6 Spontaneous Raman spectra of neat crospovidone between unstressed and stressed conditions for 24 hours.

To investigate the decrease in signal observed in SRS measurements during our time-lapse imaging, we verified whether this loss in signal was due to a change in molecular composition (spectral shift) or as a lower molecular density within the excitation volume induced by the stressing conditions (Fig. B.6). Therefore, we acquired the spontaneous Raman of neat crospovidone across the fingerprint region to discern if any spectral differences occurred between unstressed and stressed conditions at 45 °C and 60% R.H for 24 hours. We did not observe any spectral differences; however, we did notice a decrease in Raman signal intensity induced by the hydration of crosprovidone which decreases its effective concentration. Furthermore, because crospovidone is a hygroscopic molecule, water droplets were present on the powdered sample deposited on a silicon wafer which is spectrally evident towards the high wavenumber region of the spectrum.

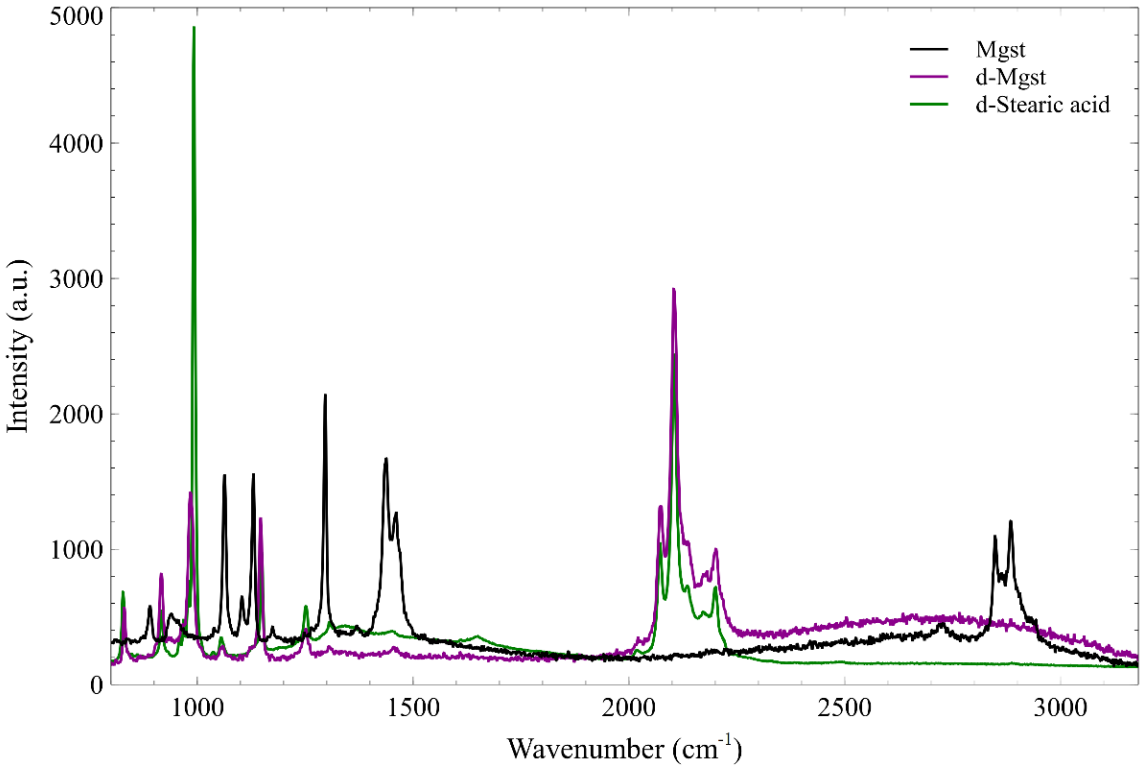

Figure B.7 Spontaneous Raman spectra of the non-deuterated Mgst, deuterated Mgst, and deuterated stearic acid.

To better visualize molecules with closely overlapped Raman signals, isotopologues (molecules that differ only in their isotopic composition), have been used to shift C-H bonds (2900-3000 cm^{-1}) into the C-D region (2000-2200 cm^{-1}) with no impact on cellular function in biomedical imaging.[6–10] Similarly, using d-Mgst instead of its counterpart shifts the vibrational peaks from the typically congested excipient region to the silent Raman region centered around 2100 cm^{-1} (Fig. B.7). We note that although both d-Mgst and d-stearic acid have similar spectra within this region, we can use the small hydroxyl peak at 1645 cm^{-1} of d-stearic acid to differentiate between these two molecular compounds. This new peak is a direct probe of the acid-base reaction converting Mgst to stearic acid.

Trying to interpret results of Fig. 3 solely on the PCC values can be misleading. While PCC provides an effective statistic for measuring overall association of two signals in an image, it does not measure the relative abundance between the two different images with respect to each other, which is at the heart of most analyses of colocalization. In addition to describing correlation with PCC, we also employed Mander's Correlation Coefficient, which further measures the fraction of one signal/image with a second signal/image.[11]. For two signals/images, denoted R and G, two different MCC values are derived, M_1, the fraction of R in compartments containing G and M_2, the fraction of G in compartments containing R. MCC values vary from 0 (non-overlapping images) to 1 (100% colocalization between both images). By providing measures of the fraction of total signal/image intensity that colocalizes with the intensity of a second signal/image, MCCs provide an intuitive and direct metric of the quantity of interest for colocalization studies. Unlike

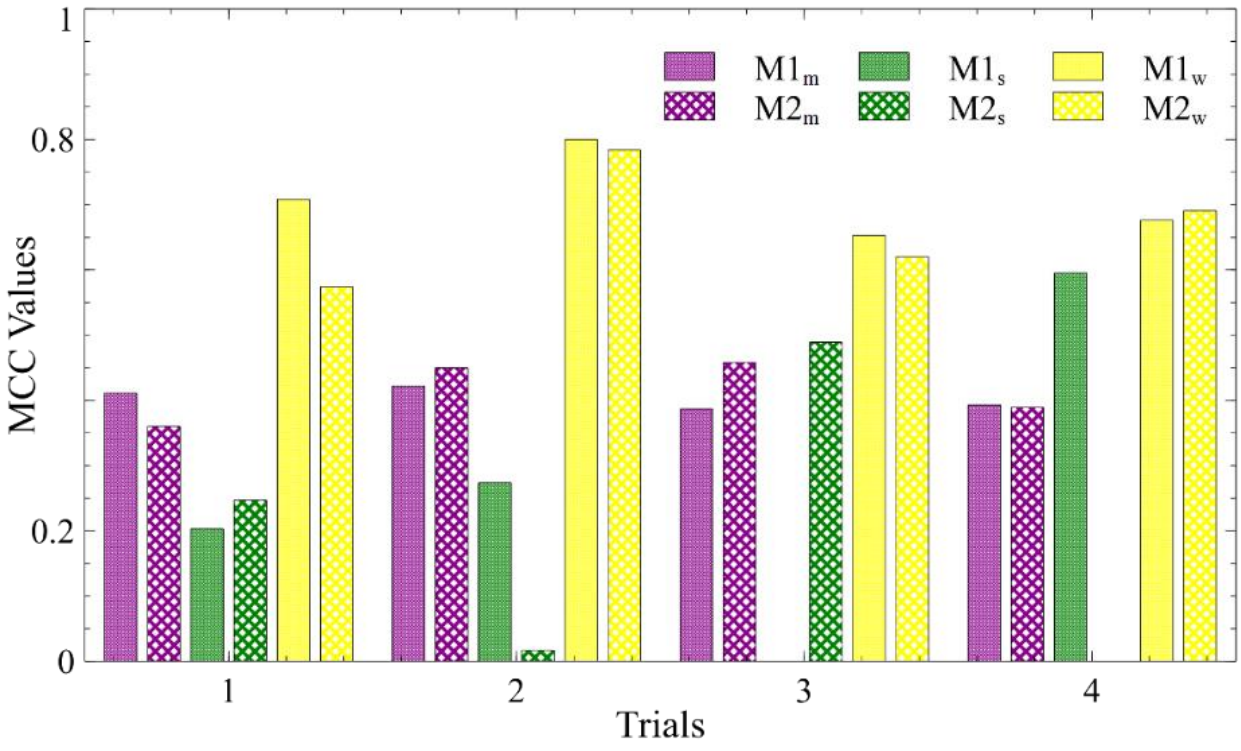

Figure B.8 Colocalization analysis of stressed 10% d-Mgst and 90% PIO-HCl tablets. The dashed and diagonal bars are the MCC values between PIO-FB and the different components.

PCC, MCC strictly measures co-occurrence independent of signal proportionality. This approach will be important in quantitatively understanding how the different components interact via the disproportionation reaction. To automatically identify the threshold value to be used to identify the background level, we used the statistical approach developed by Costes et al.[12] We then calculated fractional abundances of PIO-FB with d-Mgst, d-stearic acid, water, and vice-versa. Applying this analysis to our set of images we can quantify the amount of correlation using PCC and the co-occurrence using MCC between PIO-FB and d-Mgst and the reaction by-products such as d-stearic acid and water. $M1_x$ is the proportion of PIO-FB coincident with x species and $M2_x$ is the proportion of x species coincident with PIO-FB. In combination with the visual analysis of d-stearic in Fig 4E-H, the MCCs now allow us to quantitatively see the reason for the negative PCC value of -0.12: the fraction of PIO-FB coincidental on d-stearic acid (M1 ~0.5) is larger than the fraction of d-stearic acid on PIO-FB (0.01). Intuitively this make sense, since water is highly mobile and can be found to be colocalized with PIO-FB irrespective of the spatial profile of the d-stearic acid molecules.

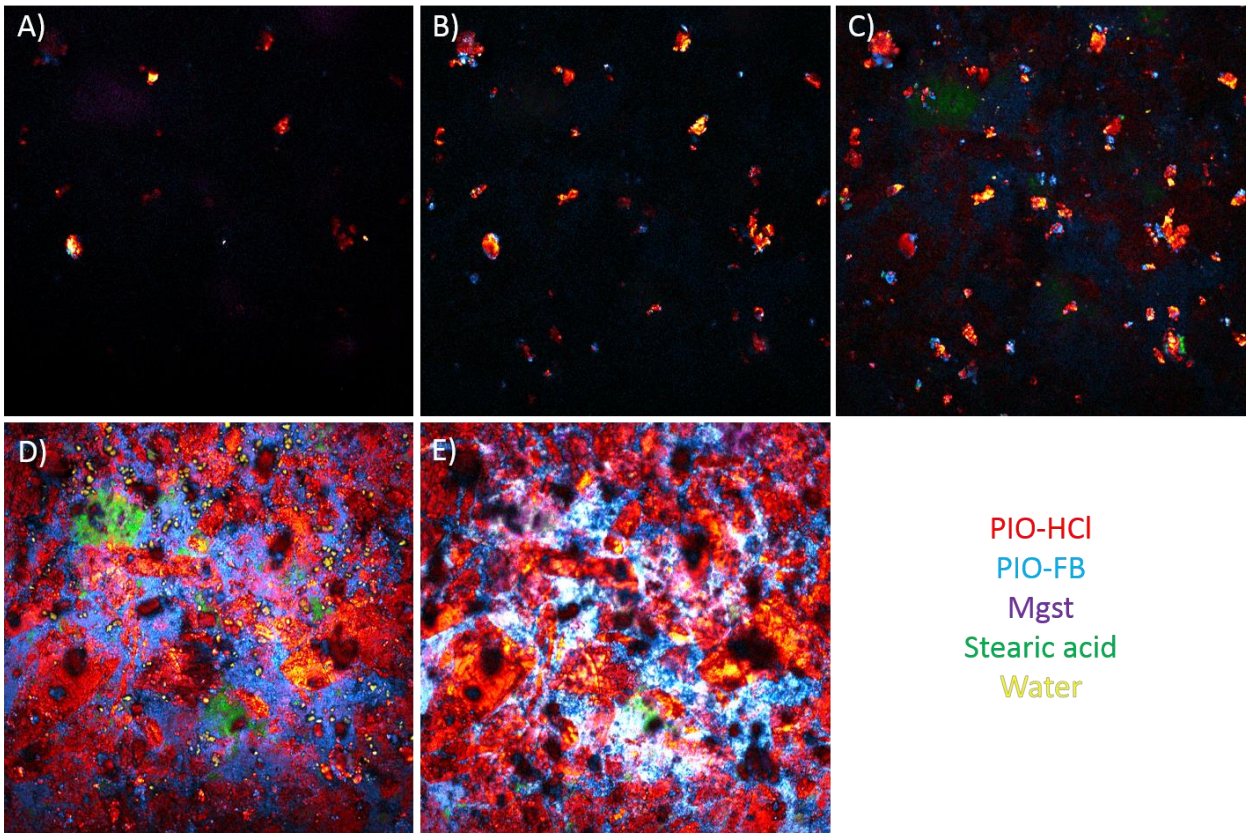

Figure B.9 Visualization of disproportionation from the surface of the tablet to a 20 μm depth below the surface. 0, 5, 10, 15, and 20 μm in A, B, C, and D, respectively.

References

1. Nie, H. *et al.* Analytical approaches to investigate salt disproportionation in tablet matrices by Raman spectroscopy and Raman mapping. *J. Pharm. Biomed. Anal.* **118**, 328–337 (2016).
2. Yathirajan, H. S., Nagaraj, B., Nagaraja, P. & Bolte, M. Pioglitazone hydro-chloride. *Acta Crystallogr. Sect. E Struct. Rep. Online* **61**, o154–o155 (2005).
3. Candolfi, A., De Maesschalck, R., Massart, D. L., Hailey, P. A. & Harrington, A. C. E. Identification of pharmaceutical excipients using NIR spectroscopy and SIMCA. *J. Pharm. Biomed. Anal.* **19**, 923–935 (1999).
4. Barnes, R. J., Dhanoa, M. S. & Lister, S. J. Standard Normal Variate Transformation and De-trending of Near-Infrared Diffuse Reflectance Spectra. *Appl. Spectrosc.* **43**, 772–777 (1989).
5. Afseth, N. K., Segtnan, V. H. & Wold, J. P. Raman Spectra of Biological Samples: A Study of Preprocessing Methods. *Appl. Spectrosc.* **60**, 1358–1367 (2006).
6. Yamakoshi, H. *et al.* Alkyne-Tag Raman Imaging for Visualization of Mobile Small Molecules in Live Cells. *J. Am. Chem. Soc.* **134**, 20681–20689 (2012).
7. Hu, F., Wei, L., Zheng, C., Shen, Y. & Min, W. Live-cell vibrational imaging of choline metabolites by stimulated Raman scattering coupled with isotope-based metabolic labeling. *Analyst* **139**, 2312–2317 (2014).
8. Hong, S. *et al.* Live-Cell Stimulated Raman Scattering Imaging of Alkyne-Tagged Biomolecules. *Angew. Chem. Int. Ed.* **53**, 5827–5831 (2014).
9. Crawford, J. M., Portmann, C., Zhang, X., Roeffaers, M. B. J. & Clardy, J. Small molecule perimeter defense in entomopathogenic bacteria. *Proc. Natl. Acad. Sci.* **109**, 10821–10826 (2012).
10. Littlejohn, G. R. *et al.* An update: improvements in imaging perfluorocarbon-mounted plant leaves with implications for studies of plant pathology, physiology, development and cell biology. *Front. Plant Sci.* **5**, (2014).
11. Manders, E. M. M., Verbeek, F. J. & Aten, J. A. Measurement of co-localization of objects in dual-colour confocal images. *J. Microsc.* **169**, 375–382 (1993).
12. Costes, S. V. *et al.* Automatic and quantitative measurement of protein-protein colocalization in live cells. *Biophys. J.* **86**, 3993–4003 (2004).

Appendix C

Appendix C accompanies Chapter 5: Real-Time Microscale Temperature Imaging by Stimulated Raman Scattering

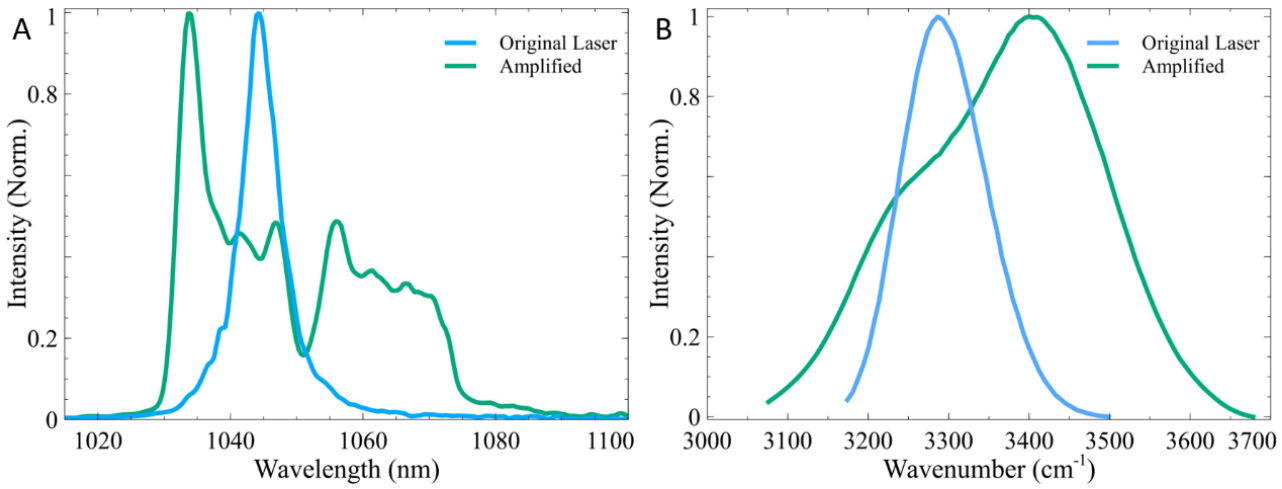

Figure C.1 Comparison of A) laser output spectrum and B) SRS spectra of water between original Insight DS+ laser and the amplified system.

Cell culture: A549 cells (ATCC) were maintained at 37°C in an atmosphere of 5% (vol/vol) CO_2. And cultured in DMEM/F-12 phenol red free medium (ThermoFisher) supplemented with 10% (vol/vol) FBS and 1% (vol/vol) penicillin/streptomycin. Cells were fixed with 4% paraformaldehyde (PFA for 30 minutes).

Broadband dual-channel SRS imaging: A femtosecond dual beam laser system (Insight DS + from Spectra-Physics) was used for hyperspectral SRS imaging based on spectral focusing as described in our earlier publications.[1,2] Figure C.2 shows our experimental setup. There are two critical improvements that are needed for water temperature imaging. Firstly, we used a parabolic fiber amplifier to increase the Stokes laser bandwidth from 6 nm to ~40 nm (Figure C.1). This is important because the original laser system only provides ~200 cm^{-1} bandwidth, which severely decreases signal level when the two bands near the edge of the bandwidth are used for imaging. The parabolic amplifier increases the bandwidth to ~500 cm^{-1}, which allows full coverage of the water Raman band and improved sensitivity. Secondly, we employed an orthogonal modulation technique for simultaneous dual-band imaging. Simultaneous imaging is important to mitigate

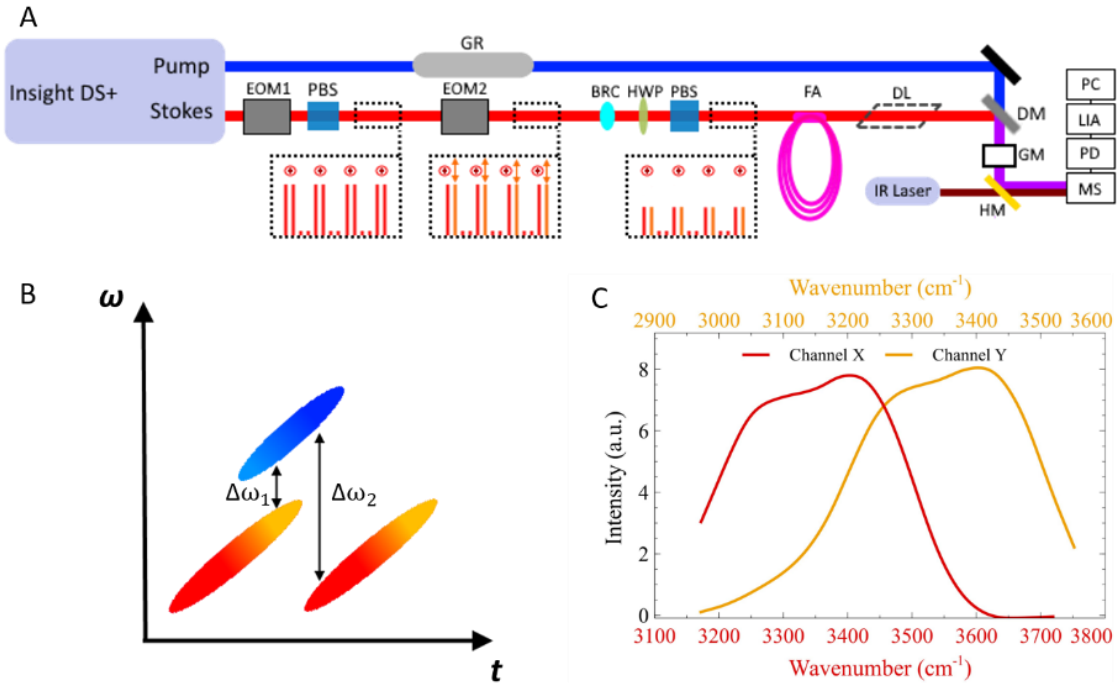

Figure C.2 Schematic diagram and principle. A) Diagram of the broadband SRS image setup. Abbreviations: GR, glass rods; EOM, electro-optical modulator; PBS, polarizing beam-splitter, BRC, birefringent crystals; HWP, half waveplate; FA, fiber amplifier; DL, delay line, DM; dichroic mirror; GM, galvo mirror; HM, IR hot mirror; MS, microscope; PD, photodiode; LIA, lock-in amplifier. B) Chirped SRS excitation scheme showing two orthogonal phase Stokes pulses and the pump pulse. C) SRS spectra of water showing Raman spectra from the two orthogonal output of lock-in amplifier.

measurement errors from laser intensity fluctuation, motion artifact, and fast temperature change. Previously we have used orthogonal modulation for quantitative transient absorption microscopy of hemoglobin. Briefly, the Stokes beam was intensity modulated at 20 MHz by an electro-optical modulator (EOM 1) and a polarizing beam splitter (PBS). This amplitude modulated pulse train was followed by another polarization modulation at 20 MHz with a second EOM (EOM2) operated at a 90° phase shift from the first EOM. The two orthogonal polarization pulse trains were then passed through a birefringent crystal to provide the temporal delay needed to probe two desired SRS transitions for temperature imaging. The pump beam was chirped by 30 cm of high dispersion H-ZF52A glass rods to match the chirp of the Stokes beam. The combined beams were directed into a home-built inverted laser scanning microscope (Olympus IX73) by a NIR hot mirror FM01R (Thorlabs). A 63x magnification Leica microscope objective was used for imaging. Two SRS images were acquired simultaneously from the lock-in X and Y output at a frame (512 x 512 pixels) rate of 1 frame/sec. Power of pump and Stokes were set at 30 and 80 mW, respectively.

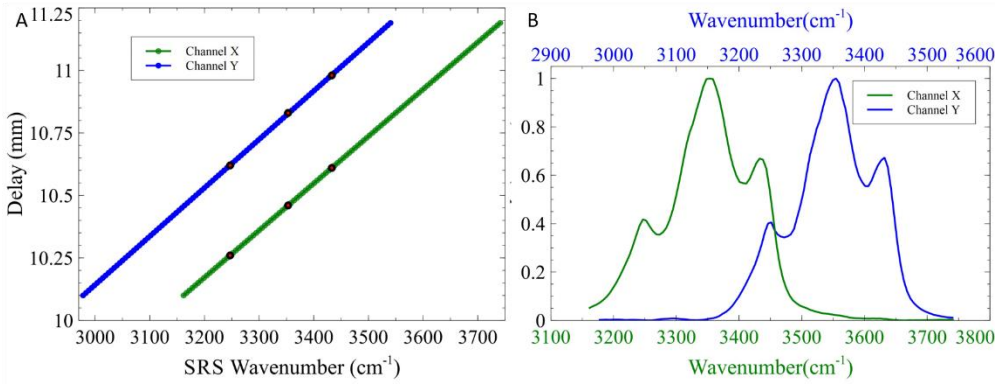

Figure C.3 Calibration of SRS imaging setup based on a parabolically amplified femtosecond dual beam laser system. A) Calibration of SRS wavenumber with respect to pump-Stokes pulse delay using Raman spectra of Urea. Markers indicate 3247, 3353, and 3433 cm^{-1} Raman transitions used to calibrate spectra. B) Simultaneous collection of 2-channel SRS spectra arising from OH stretching vibrations of solid urea crystals.

Temperature calibration and imaging: Calibration of SRS microscope for OH imaging was done by imaging the Raman peak of urea crystals (Figure C.3). To measure temperature, we simultaneously image the HB vibration (~3220 cm^{-1}) and the NHB vibration (~3420 cm^{-1}) of water. We chose the isosbestic of the non-hydrogen-bonded Raman band for ratiometric analysis because it is independent of temperature and has high signal intensity. SRS images of the HB and isosbestic modes are simultaneously acquired using the dual-band SRS imaging system. Temperature distribution of the imaging plane is calculated from the intensity ratio of the two SRS images. For temperature calibration and imaging, a temperature-controlled micro-observation chamber was added to our microscope (FCS2, Bioptechs). The FCS2 use an electrically conductive transparent thin film of Indium-Tin Oxide to provide uniform heating. In addition, we used a Bioptechs Objective Heater System to eliminate the thermal heatsink from the objective that would otherwise be detrimental to maintain the temperature of the chamber. Absolute temperature in the sample is acquired through a miniature thermocouple (223Fμ3122-07U015, Mouser) for calibration.

COMSOL Simulations: Numerical simulations of thermal images were performed with COMSOL Multiphysics software v 5.5[3] which solves Fourier's heat equation, $\rho c_p \partial_t T = \kappa \nabla^2 T + q(\boldsymbol{r}, T)$, where ρ is density, c_p is constant-pressure heat capacity, κ thermal conductivity, and $q(\boldsymbol{r}, T)$ describing the time-dependent heating laser source. The optical heat source was modeled with a Gaussian distribution with FWHM of 1 μm. The absorption coefficient of water at 1480 nm was ~21 cm^{-1}.[4] The rotational symmetry of the spot makes the temperature field axisymmetric and the problem reduces to a 2D problem in the radial coordinate r and the vertical coordinate z. The thicknesses of the water domain, coverslip, and glass slide were 100, 130, and 1000 μm, respectively. Under the coverslip was a layer of objective water with a thickness of 100 μm, followed by a 1 cm x 10 cm objective domain kept at constant temperature set 33°C. We simulated heat diffusion in water with initial temperature and boundary conditions set 33°C. The focused spot was modeled with an ultra-fine mesh element size, with domains further away comprising of "finer" meshing element sizes.

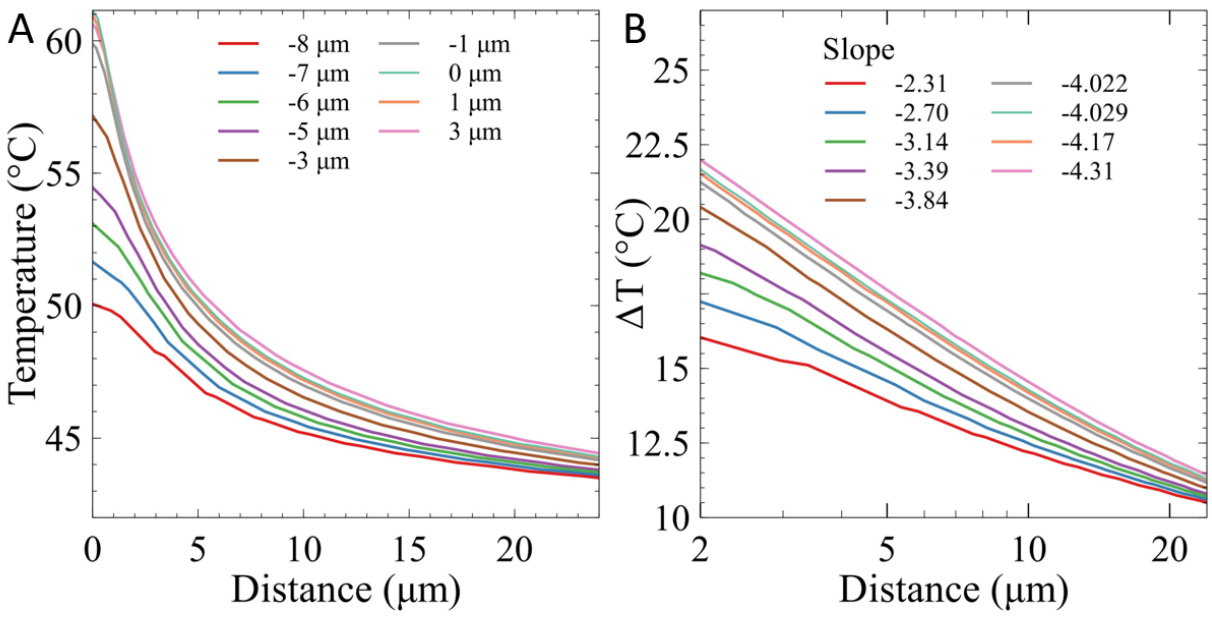

Figure C.4 Thermal profiles as a function of axial location of heating source and imaging planes. A) Thermal profile of heating source at different imaging planes. B) Slopes of A.

As seen in Figure C.4, the introduction of a proportionality constant is necessitated by the fact that the slope of the thermal profile will be influenced by proximity of any heat sinks near the point heat source. Closer to the coverslip (z = -10 um), the thermal profile sees a reduced slope. To obtain the proportionality constant at any imaging plane, the ratio between the effective k which is extracted from the slope of the equation $\Delta T = \frac{\alpha(\lambda)*P}{2\pi k_{eff}} * ln(r)$ and the literature value of k is calculated and is subsequently used to extract the k of different ROI within the same imaging plane.

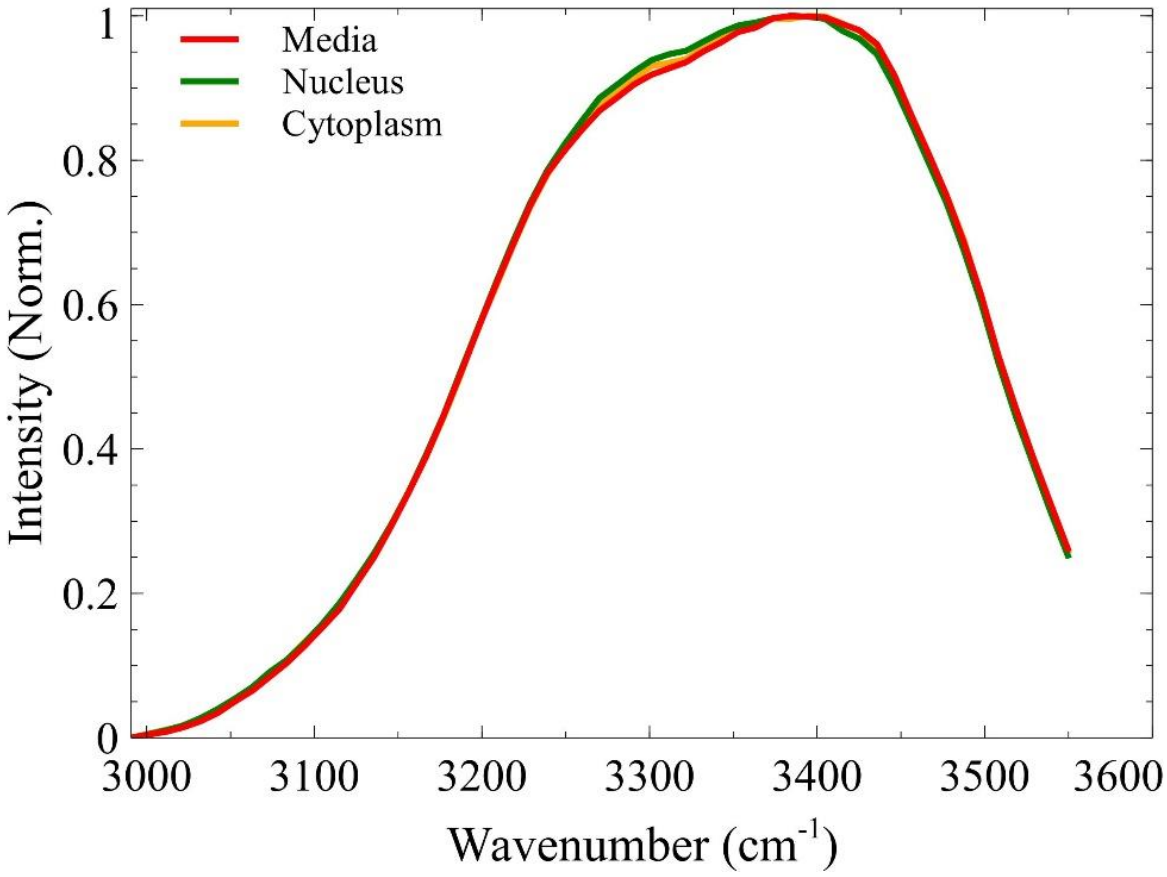

Figure C.5 SRS spectra of regions of interest in a fixed cell.

References

(1) Figueroa, B.; Nguyen, T.; Sotthivirat, S.; Xu, W.; Rhodes, T.; Lamm, M. S.; Smith, R. L.; John, C. T.; Su, Y.; Fu, D. Detecting and Quantifying Microscale Chemical Reactions in Pharmaceutical Tablets by Stimulated Raman Scattering Microscopy. *Anal. Chem.* **2019**. https://doi.org/10.1021/acs.analchem.9b01269.

(2) Fu, D.; Holtom, G.; Freudiger, C.; Zhang, X.; Xie, X. S. Hyperspectral Imaging with Stimulated Raman Scattering by Chirped Femtosecond Lasers. *J. Phys. Chem. B* **2013**, *117* (16), 4634–4640. https://doi.org/10.1021/jp308938t.

(3) COMSOL: Multiphysics Software for Optimizing Designs https://www.comsol.com/ (accessed Apr 16, 2020).

(4) Curcio, J. A.; Petty, C. C. The Near Infrared Absorption Spectrum of Liquid Water. *JOSA* **1951**, *41* (5), 302–304. https://doi.org/10.1364/JOSA.41.000302.

VITA

Benjamin Figueroa, Jr was born in Tucson, AZ. in 1992 where he spent most of his childhood. After spending a year in Argentina with his family, he moved to Auburn, WA. in 2007. Here is where he first enjoyed being called a scientist by his highschool physics teacher and began thinking like a scientist. A soccer aficionado, he has always enjoyed taking a break from studying to play soccer with friends and family. Ben attended La Sierra University (Riverside, CA) from 2010-2015, earning a Bachelor of Science degree in both Biophysics and Biochemistry (minor in Math). In Fall 2015, Ben entered the Ph.D. program in Chemistry at the University of Washington and joined the research group of Professor Dan Fu. In addition to learning nonlinear microscopy, he also learned how to dance salsa and bachata and eventually instruct at the UW Salsa club in his 5th year. In graduate school, Ben was very active in outreach as he would visit local Seattle schools with a group of fellow graduate students and then later became a Science Communication Fellow through Seattle's Pacific Science Center.

Selected Honors and Awards

2019 IDEA scholarship, Pacific Science Center
2019 NSF-AGEP Research Exchange Retreat Funding
2019 NSF-AGEP Research Exchange Fellowship
2018 Lloyd E. Florence M. West Fellowship in Chemistry
2017 National Science Foundation Graduate Research Fellowship
2015 Outstanding Senior Award for Biochemistry
2015 Outstanding Senior Award for Physics
2010-2015 Who's Who award nominee
2010-2015 Dean's List
2014 Lester H. Cushman Endowed Scholarship from La Sierra University